An Edgy Journey with Transition Metal Dichalcogenides
From Flakes to Nanopillars

Maduro, L.A.

DOI
Publication date
2021
Document Version
Final published version
Citation (APA)

Important note
To cite this publication, please use the final published version (if applicable).
Please check the document version above.

AN EDGY JOURNEY WITH TRANSITION METAL DICHALCOGENIDES

FROM FLAKES TO NANOPILLARS

AN EDGY JOURNEY WITH TRANSITION METAL DICHALCOGENIDES

FROM FLAKES TO NANOPILLARS

Proefschrift

ter verkrijging van de graad van doctor

aan de Technische Universiteit Delft,

op gezag van de Rector Magnificus Prof.dr.ir T. H. J. J. van der Hagen,

voorzitter van het College voor Promoties,

in het openbaar te verdedigen op donderdag 30 september 2021 om 15:00 uur

door

Louis Arcolino MADURO

Master of Science in Physics,
Universiteit Leiden, Nederland

geboren te Aruba.

To my parents

The universe is full of magical things,
patiently waiting for our wits to grow sharper

- Author Disputed

CONTENTS

SUMMARY

The family of transition metal dichalcogenides offer a unique platform for electronic and optical tunability due to the sensitivity to their dimensional configuration, edge terminations, and varying crystal phases. In this thesis we focus on structures based on the transition metal dichalcogenides MoS_2 and WS_2. We study how different crystal phases and edge structures of these two transition metal dichalcogenides affect their optical, electronic, and structural behaviour with the use of electron energy loss spectroscopy, energy-dispersive X-ray spectroscopy, and high resolution spatial imaging in the transmission electron microscopy in order to carry out our studies. When possible, we complement our experimental studies with ab initio calculations.

In chapter 3 we use monochromated electron energy-loss spectroscopy together with high resolution imaging in the transmission electron microscope and demonstrate the presence of strain-dependent edge structures in flakes of MoS_2 monolayers. The strain at the edges of the MoS_2 layers depends on the presence of zig-zag or armchair edges. Tensile strain is observed for both types of edge configurations, with the zig-zag edges exhibiting larger strain than the armchair edges. We observe a broadening of the exciton peaks in the transition region when going from three to two monolayers of MoS_2.

In chapter 4 we controllably fabricate MoS_2 nanowalls with specific atomic edge terminations. The MoS_2 layers are exfoliated from a bulk crystal and deposited onto a Si substrate. By exploiting the crystal symmetries of MoS_2 we chose specific edge structures corresponding to zig-zag and armchair edge terminations in a thick MoS_2 flake. High-resolution transmission electron microscopy is used to identify the edge structures. With electron energy loss spectroscopy we observe edge-dependent electronic behaviour. An indication of metallic edge behaviour corresponding to the zig-zag edge termination is observed, which is in agreement with metallic behaviour of a simple model of a zig-zag terminated MoS_2 nanowall which is found by density functional theory calculations.

In chapter 3 and chapter 4 we studied MoS_2 structures fabricated based on exfoliation techniques. While exfoliation techniques can be used to study fundamental questions concerning transition metal dichalcogenides, it is not a scalable technique for industrial scale applications. In this respect, we develop a scalable two-step procedure based on nanofabrication techniques(chapter 5) combined with chemical vapour deposition (chapter 6). In chapter 5 we describe a fabrication process for Mo nanopillars producing nanopillar structures with controllable shapes, sizes, and densities. We start with depositing a layer of Si_3N_4 via low-pressure chemical vapour deposition on top of a Si substrate, which is used as a protective layer for the Si. Afterwards, sputter-deposition of Mo films on top of Si substrates is carried out. The controllable Mo nanopillar fabrication is achieved by first defining nanostructures with electron beam lithography using hydrogen silsesquioxane negative tone resist as a mask. We subsequently etch the unprotected Mo film at cryogenic temperatures using inductively coupled plasma reactive

ion etching in a SF_6/O_2 gas mixture. The utility of the Si_3N_4 layer becomes apparent in the etching step. With the used etch parameters Si etches at a much higher rate than Mo; The Si is rapidly etched away leading to the Mo nanostructures collapsing onto the Si surface in the case without a Si_3N_4 protective layer. With this procedure we fabricate Mo nanopillars with smooth sidewalls and high aspect ratios where the sizes, shapes, and densities are controlled with precision. The remaining resist is removed by using a diluted hydrofluoric acid solution.

In chapter 6 we use the fabricated Mo nanopillars as a template for the synthesis of core-shell Mo-MoS_2 nanopillars using chemical vapour deposition. We find that a reaction temperature of 650°C produces controllable MoS_2 shells for the fabricated nanopillars. By varying the reaction time we can control the size and morphology of the MoS_2 shell. The core-shell configuration of the Mo-MoS_2 nanopillars is confirmed using high-resolution transmission electron microscopy and energy-dispersive X-ray spectroscopy. We observe that the MoS_2 shell consists of MoS_2 layers which grow perpendicular to the Mo core, resulting in a mixture of horizontally and vertically oriented MoS_2 layers with respect to the substrate surface. The orientation of the MoS_2 shells indicate that the boundaries of the core-shell Mo-MoS_2 nanopillars consists of edge structures of MoS_2 layers. The plasmonic behaviour of the Mo core and MoS_2 shell is studied with the use of electron energy-loss spectroscopy. A bulk plasmon peak, along with π-plasmon peaks for the MoS_2 shell is found which is in agreement with literature values for MoS_2. We demonstrate that the metallic behaviour of the Mo core is retained by observations of the bulk plasmonic peaks found in bulk Mo. Finally, the nonlinear optical response of the core-shell Mo-MoS_2 nanopillars is studied and compared to the nonlinear optical response of MoS_2 flakes grown on the same substrate. For the core-shell Mo-MoS_2 nanopillars an enhanced nonlinear signal of the second harmonic generation signal of the 775 nm laser excitation and sum-frequency mixing signal is observed compared to the MoS_2 flakes.

In chapter 7 we use ab initio methods based on density functional theory and many-body perturbation theory to study the electronic and optical behaviour of different crystal phases of bulk WS_2. The crystal phases studied are the 2H, 3R, and mixed 2H-3R polytypes of WS_2. From the density of states we see for all the crystal structures that the tungsten d orbitals and sulfur p orbitals are the main contributors for states near the Fermi energy. All three crystal phases exhibit an indirect band gap. The 2H phase has a band gap value of 1.39 eV, in agreement with literature values. The 3R phase has a band gap value of 1.62 eV, which is the first such calculation of the band gap of the 3R WS_2 polytype to our knowledge. The mixed 2H-3R phase has a band gap value lying in between the 2H and 3R crystal phases at 1.48 eV, in agreement with the measured value found for such a crystal. The positions of the bulk plasmon peaks do not vary much for the different crystal phases, lying in a range of 20.69 eV and 22.03 eV. We further identify the valence and conduction bands contributions to the joint density of states, which can be directly related to the energy loss function within dielectric theory framework used in this work. The band structure character can be further used to identify the orbital nature in the joint density of states, which can then be related to the features in the energy-loss function.

SAMENVATTING

De familie van transitiemetaal dichalcogeniden vormt een unieke platform voor het gecontroleerd afstemmen van elektronische en optische eigenschappen door hun gevoeligheid voor de specifieke dimensionale configuratie, atomaire randstructuren, en kristalstructuren. In deze scriptie concentreren wij ons op de transitiemetaal dichalcogeniden MoS_2 en WS_2. Wij bestuderen de optische, elektronische, en structurele eigenschappen als functie van verschillende kristalstructuren en configuraties van de atomaire randen van deze transitiemetaal dichalcogeniden. We voeren ons onderzoek uit met behulp van elektronen-energieverlies-spectroscopie, energie-dispersieve Röntgenspectroscopie, en door hoge resolutie afbeeldingen te maken met behulp van transmissie-elektronenmicroscopie. Wij gebruiken ab initio methoden om de eigenschappen van de bestudeerde transitiemetaal dichalcogeniden verder te begrijpen. In hoofdstuk 3 gebruiken we monochrome

elektronen-energieverlies-spectroscopie samen met hoge resolutie afbeeldingen van een transmissie-elektronenmicroscoop om de aanwezigheid van spanning af-hankelijke randstructuren aan te tonen. De structurele spanning bij de randen van de MoS_2 lagen wordt bepaald door de aanwezigheid van zigzagvormige of armstoelvormige atomaire configuraties. Trekspanning is waargenomen voor beide type randstructuren, waar de zigzagvormige randen onder een hogere spanning staan dan de armstoelvormige randen. Wij nemen een verbreding waar van de exciton pieken in het gebied rond de overgang van twee tot drie monolagen van MoS_2.

In hoofdstuk 4 fabriceren wij op een controleerbare wijze MoS_2 nanomuren met specifieke atomaire randstructuren. Dikke lagen van MoS_2 zijn geëxfolieerd van een bulk kristal en vervolgens gelegd op een Si substraat. Door gebruik te maken van de kristal symmetrieën van MoS_2 is het mogelijk om zigzagvormige en armstoelvormige randstructuren te isoleren uit de gebruikte dikke vlok van MoS_2. De zigzagvormige en armstoelvormige atomaire randstructuren van de MoS_2 nanomuren worden aangetoond door hoge resolutie afbeeldingen te maken in een transmissie-elektronenmicroscoop. Wij zien rand-afhankelijke elektronische eigenschappen met behulp van elektronen-energieverlies-spectroscopie. Wij observeren me-taalachtig gedrag bij de zigzagvormige randstructuren, dat in overeenkomst is met me-taalachtig gedrag in een simpel model van een MoS_2 nanomuur met zigzagvormige randstructuren, berekend met behulp van dichtheidsfunctionaaltheorie.

In hoofdstuk 3 en hoofdstuk 4 hebben wij MoS_2 structuren bestudeerd die gemaakt zijn met behulp van exfoliëren. Door dit exfoliëren is het mogelijk geweest om fundamentele vragen over transitiemetaal dichalcogeniden te beantwoorden. Deze specifieke manier-en om te exfoliëren zijn echter niet geschikt om op te schalen voor industriële applicaties. Daarom hebben wij een opschaalbare twee-staps methode ontwikkeld, gebaseerd op nanofabricage methoden (hoofdstuk 5) gecombineerd met chemische dampdeposi-

tie (hoofdstuk 6), voor het maken van nanostructuren gemaakt van transitiemetaal di-chalcogeniden. Wij beginnen in hoofdstuk 5 met de beschrijving van een controleer-bare fabricage methode om Mo nanopilaren te produceren met verschillende vormen, dimensies, en dichtheden. Wij beginnen het process door eerst een beschermende laag van Si_3N_4 aan te brengen op een Si substraat met behulp van lage-druk chemische damp-depositie. Vervolgens gebruiken we sputter-depositie om een laag Mo te deponeren op het substraat. De gecontroleerde Mo nanopilaar fabricage wordt allereerst mogelijk gemaakt door de nanostructuren te definiëren met elektronenbundel lithografie in com-binatie met een waterstof silsesquioxane negatief resist als een masker. Vervolgens etsen we de onbeschermde laag Mo op cryogene temperaturen door gebruik te maken van in-ductief gekoppeld plasma-etsen in een SF_6/O_2 gas mengsel. In de stap met het plasma-etsen kunnen we duidelijk het effect van de Si_3N_4 laag zien. De gebruikte etsparameters leiden tot een veel hogere etssnelheid voor het onderliggende Si substraat vergeleken met de laag Mo; in het geval zonder de Si_3N_4 laag wordt de onderliggende Si snel weggeëtst, met als gevolg dat de Mo nanostructuren op het geëtste Si oppervlak instorten. Met dit process is het mogelijk om op een controleerbare wijze Mo nanopilaren te maken met scherpe zijwanden, hoge aspectverhouding, waarbij nanopilaren met verschillende groottes, vormen, en dichtheden worden geproduceerd. Het resterende resist wordt weggehaald in een verdunde oplossing van waterstoffluoride zuur. In hoofdstuk 6 wor-den de gefabriceerde Mo nanopilaren gebruikt als steiger voor kern-schil Mo-MoS_2 nano-pilaren die worden gemaakt met behulp van chemische dampdepositie. De groei van de MoS_2 schil is goed te controleren bij een reactietemperatuur van 650°C. De grootte en vorm van de MoS_2 schil kan worden gecontroleerd door de reactietijd te variëren. De kern-schil structuur wordt in beeld gebracht met behulp van hoge resolutie transmissie-elektronenmicroscopie en energie-dispersieve Röntgenspectroscopie. De schil van MoS_2 bestaat uit lagen van MoS_2 die loodrecht groeien ten opzichte van de Mo kern, met als gevolg dat er horizontale en verticale MoS_2 lagen groeien ten opzichte van het substraat oppervlak. De oriëntatie van de MoS_2 schil is een indicatie dat de grenzen van de kern-schil Mo-MoS_2 nanopilaren bestaan uit MoS_2 randstructuren. Wij gebruiken elektron energieverlies spectroscopie om het plasmonische gedrag van de Mo kern en MoS_2 schil te bestuderen. De bulk plasmon piek, samen met de π-plasmon piek, is waargenomen voor de MoS_2 schil en die zijn in goede overeenkomst met de literatuur waarden. Het metallische gedrag van de Mo kern is aan te tonen door de waarneming van de bulk plas-mon pieken karakteristiek voor puur Mo. Tenslotte, bestuderen wij de niet-lineaire op-tische respons van de kern-schil Mo-MoS_2 nanopilaren en vergelijken we de respons met de respons van MoS_2 vlokken die op hetzelfde substraat zijn gegroeid. Vergeleken met de MoS_2 vlokken tonen de kern-schil Mo-MoS_2 nanopilaren een versterkt niet-lineaire signaal van de tweede harmonische generatie van 775 nm laser licht en van het som-frequentie signaal.

In hoofdstuk 7 gebruiken wij ab initio methoden gebaseerd op dichtheidsfunctionaaltheo-rie en veel-deeltjes storingsrekening om het elektronische en optische gedrag van ver-schillende kristalstructuren van WS_2 te bestuderen. Wij bestuderen de zogenaamde 2H, 3R, en gemengde 2H-3R polytypen van WS_2. Uit de toestandsdichtheid zien wij dat de wolfraam d-orbitalen en zwavel p-orbitalen de grootste bijdragen leveren aan de elek-tronische toestanden van 2H-3R WS_2 dichtbij de Fermi energie. Alle drie de kristalstruc-

turen hebben een indirecte band gap. De 2H kristalfase heeft een band gap waarde van 1.39 eV, in overeenkomst met literatuur waarden. De 3R kristalfase heeft een band gap waarde van 1.62 eV. Dit is voor zover wij weten de eerste berekening van de band gap van de 3R kristalfase. De gemengde 2H-3R kristalfase heeft een band gap waarde die ligt tussen de waardes van de 2H en 3R fase, en is 1.48 eV, in overeenkomst met de eerste gemeten waarde van deze kristalfase. De bulk plasmon pieken van de verschillende kristalstructuren liggen dichtbij elkaar, tussen de 20.69 eV en 22.03 eV. Verder lichten we de bijdrage van de valentiebanden en de geleidingsbanden aan de gezamenlijk toestandsdichtheid toe, die direct kan worden gerelateerd aan de energieverlies functie in de context van dielektrische theorie. De bandstructuur kan verder worden gebruikt om het orbitale karakter van de gezamenlijk toestandsdichtheid te bestuderen om vervolgens het gedrag van de energieverlies functie te begrijpen.

Summario

E famia di dicalcogenido di metal di transicion ta ofrece un plataforma unico pa sintonisacion electronico y optico debi na nan sensibilidad pa mustra nan configuracion dimensional, terminacion di e randnan atomico presente y variacion di e fasenan di cristal. Den e tesis aki nos ta enfoca riba e structuranan basa riba e dicalcogenidonan di metal di transicion MoS_2 y WS_2. Nos ta investiga con diferente fase di cristal y structura di rand atomico di e dos dicalcogenidonan di metal di transicion aki ta afecta nan comportacion optico, electronico y structural, uzando spectroscopia di perdemento di energia di e electronnan, spectroscopia di X-ray di dispersion di energia y imagen espacial di resolucion halto den microscopia di transmision di electron pa haci e investigacion. Unda ta posibel, nos ta complementa nos investigacionnan experimental cu calculacionnan for di cuminsamento.

Den capitulo 3 nos ta uza spectroscopia monocromatico di perdemento di energia di e electronnan hunto cu imagen di resolucion halto den microscop di transmision di electron y nos ta demostra presencia di structura di rand dependiente di stress den scama di monocapa di MoS_2. E stress na e randnan di e capanan di MoS_2 ta depende di e presencia di rand cu forma zig-zag of cu forma di stoel di man. Ta observa stress door di rekmento na ambos tipo di configuracion di rand, cu e randnan cu forma zig-zag presentando mas stress cu e randnan cu forma di stoel di man. Nos ta observa un hanchamento di e topnan di exciton den e region di transicion bayendo di tres pa dos monocapa di MoS_2.

Den capitulo 4 na un forma controlabel nos a traha nanomuraya di MoS_2 cu terminacion di rand atomico specifico. E capanan di MoS_2 ta forma door di exfoliacion for di un cristal na bulto y ta pone nan riba un substrato di Si. Probechando e simetrianan di e cristal di MoS_2 nos ta scoge structura di rand specifico cu ta coresponde cu terminacion di rand cu forma zig-zag y cu forma di stoel di man den un scama diki di MoS_2. Ta uza microscopia di transmision di electron di resolucion halto pa identifica e structuranan di rand atomico. Cu spectroscopia di perdemento di energia di e electronnan nos ta observa comportacion electronico dependiente di e randnan. Ta observa un indicacion di comportacion di rand metalico cu ta coresponde cu e terminacion di rand cu forma zigzag, cual ta concorda cu comportacion metalico di un modelo simpel di un nanomuraya di MoS_2 cu terminacion cu forma zig-zag haya pa medio di calculacion cu teoria funcional di densidad.

Den capitulo 3 y 4 nos a investiga e structuranan di MoS_2 fabrica, basa riba e tecnicanan di exfoliacion. Aunke por uza e tecnicanan di exfoliacion pa investiga cuestionnan fundamental relaciona cu e dicalcogenidonan di metal di transicion, e no ta un tecnica escalabel pa aplicacion na escala industrial. Pa tal motibo, nos a desaroya un procedura escalabel di dos paso basa riba tecnica di nanofabricacion (capitulo 5) combina cu deposicion kimico di vapor (capitulo 6). Den capitulo 5 nos ta describi un proceso di fabri-

cacion di nanopilar di Mo cu ta produci structura nanopilar cu forma, grandura y densidad controlabel. Nos ta cuminsa depositando un capa di Si_3N_4 pa medio di deposicion kimico di vapor na presion abou, cu ta uza como capa protector pa Si. Despues nos ta efectua deposicion di capa di Mo riba e substratonan di Si pa medio di pulverisacion catodico. Ta logra fabricacion di nanopilar di Mo controlabel door di defini primeramente e nanostructuranan cu litografia di rayo di electron, uzando como masker e resistencia di tono negativo di hidrogeno silseskioxano. Posteriormente nos ta kita e capa di Mo cu no ta protegi uzando kitamento di ion reactivo pa medio di plasma acopla inductivamente den un mescla di gas SF_6/O_2 na temperatura criogenico. E uzo di e capa di Si_3N_4 ta bira evidente durante e stap di kitamento di e Mo. Cu e parameternan di kitamento uza nos ta observa cu Si ta bira kita na un velocidad mucho mas halto cu Mo; Si ta kita perde rapidamente cu e resultado cu e nanostructuranan di Mo ta colapsa cay riba e superficie di Si den e caso cu no tin un capa protector di Si_3N_4 riba Si. Cu e procedura aki nos por produci nanopilar di Mo cu muraya lateral liso y proporcion di aspecto halto na unda ta controla grandura, forma y densidad di e structuranan cu precision. Ta elimina e resto di e capa di proteccion uzando un solucion dilui di acido hidrofluorico.

Den capitulo 6 nos ta uza e nanopilarnan di Mo fabrica como skelet pa e sintesis di nanopilar, unda tin un centro di Mo rondona pa MoS_2, cu nos ta yama nanopilar di Mo-MoS_2 cu casca nucleo, uzando deposicion kimico di vapor. Nos a descubri cu un temperatura di reaccion di 650°C pa e sintesis ta produci casca di MoS_2 controlabel pa e nanopilarnan fabrica. Variando e tempo di reaccion nos por controla e grandura y e morfologia di e casca di MoS_2. E configuracion di e casca nucleo di e nanopilarnan di Mo-MoS_2 ta keda confirma pa medio di microscopia di transmision di electron na unda nos a traha imagen di resolucion halto hunto cu spectroscopia di X-ray di dispersion di energia. Nos a observa cu e casca di MoS_2 ta consisti di capa di MoS_2 cu ta crece perpendicularmente for di e nucleo di Mo, resultando den un mescla di capa di MoS_2 orienta horizontalmente y verticalmente respecto di e superficie di e substrato di Si. E orientacion di e cascanan di MoS_2 ta indica cu e limitenan di e nanopilarnan di Mo-MoS_2 cu casca nucleo ta consisti di structura di rand di e capanan di MoS_2. Uzando spectroscopia di perdemento di energia di e electronnan nos a investiga e comportacion plasmonico di e nucleo di Mo y di e casca di MoS_2. Nos a haya un top di plasmon na bulto, hunto cu top di -plasmon di e casca di MoS_2, cu ta di acuerdo cu e balornan haya den literatura cientifico pa MoS_2. Nos ta demostra cu e comportacion metalico di e nucleo di Mo ta keda presente door di observacion di e topnan di plasmon na bulto haya den Mo na bulto. Finalmente, nos a investiga e reaccion optico no lineal di e nanopilarnan di Mo-MoS_2 cu casca nucleo y a compara e señal cu e reaccion optico no lineal di e scamanan di MoS_2 cu a crece riba e mesun substrato di Si. Pa e nanopilarnan di Mo-MoS_2 cu casca nucleo nos ta observa un señal no lineal amplia di e señal di e di dos generacion harmonico di e excitacion cu laser di 775 nm y di e señal di mescla di e suma di frecuencia compara cu e scamanan di MoS_2.

Den capitulo 7 nos ta haci calculacion for di cuminsamento basa riba teoria funcional di densidad y riba teoria di perturbacion di hopi curpa pa investiga e comportacion electronico y optico di diferente fase di cristal di WS_2 na bulto. E fasenan di cristal investiga ta e politiponan di WS_2: 2H, 3R y 2H-3R mescla. E densidad di e estadonan ta demostra pa tur e structuranan di cristal cu e contribucionnan mas grandi pa e estadonan cerca

di e energia di Fermi ta e orbitalnan d di tungsteno y e orbitalnan p di azufro. Tur tres fase di cristal tin un habri di banda indirecto. E habri di banda di fase 2H tin un balor di 1.39 eV, di acuerdo cu e balornan den literatura cientifico. E habri di banda di fase 3R tin un balor di 1.62 eV. Cu nos sa, esaki ta e prome biaha cu a haci e tipo di calculacion aki pa determina e balor di e habri di banda di e politipo 3R di WS$_2$. E fase mixto 2H-3R tin un balor di habri di banda cu ta keda entre e fasenan di cristal 2H y 3R, cu ta 1,48 eV, di acuerdo cu e balor haya for di experimento haci cu cristal di fase 2H-3R. E posicionnan di e topnan di plasmon na bulto no ta varia mucho hopi entre e tres fasenan di cristal, unda e balornan ta entre 20.69 eV y 22.03 eV. Ademas, nos a identifica e contribucion di e bandanan di valencia y di conduccion na e densidad di e estadonan conhunto, cu por relaciona directamente cu e funcion di perdemento di energia den cuadro di e teoria di-electrico uza den e estudio aki. Por sigui uza e caracter di structura di banda pa identifica e caracter orbital den e densidad di e estadonan conhunto, cu na su turno por relaciona cu e caracteristicanan pa studia structura di e funcion di perdemento di energia.

1

INTRODUCTION

A MATTER OF (QUANTUM) MATTER

For the majority of human history, we have created tools without the need of a fundamental understanding of the underlying materials[1]. However, this lack of knowledge has been the one source of inspiration for thousands of scientists to pursue a path in unravelling the mysteries of nature. With this motivation, theories to understand the laws of nature have undergone multiple paradigm shifts throughout our history, with the most recent occurring in the beginning of the twentieth century with the advent of quantum mechanics.

Quantum theory, and its relativistic counterpart Quantum Field Theory, is undoubtedly the most successful description of nature we have ever developed. Our fundamental understanding of materials, as well as our ability to craft new materials, has greatly increased due to the development of quantum theory, increasingly powerful computers, and reliable and accurate techniques and instrumentation. Thanks to our ever-improving understanding, we are in a unique position to tackle pressing technological challenges facing our contemporary world such as energy storage and generation, efficient and secure communication, and sensitive medical techniques, to name a few examples.

With this state of affairs, a massive research effort is taking place in material science to best understand and craft new technologies suited for these challenges. One particularly promising group of materials in this context is the family of *transition metal dichalcogenides* (TMDs). Materials of the family of TMDs exhibit remarkable physical and chemical functionalities, which in turns makes a wide range of applications possible. This thesis is a study of the physical properties of different nanoscale structures composed of TMD materials. In the following sections, we will develop some acquaintance of the properties of TMDs that make them so promising both in terms of fundamental science and of practical applications.

TWO-DIMENSIONAL PLAYGROUNDS

The family of layered, or van der Waals (vdW), materials is characterized by the layered organization of their constituent atoms; the atoms inside a layer are tightly bound by valence bonds, while the layers are weakly bound by the van der Waals interaction. The unique interplay of weak vdW bonding *between* layers, and strong covalent bonding of atoms *inside* a layer, makes it possible to isolate single layers of vdW materials. One useful analogy is comparing the mechanical stability of layered materials with a stack of plywood; it is quite easy to move around sheets of plywood with respect to each other, however a bit more directed effort is needed to tear apart one of these sheets. The first isolation and study of graphene demonstrated the potential applications of vdW materials; graphene, a single layer of carbon atoms, exhibited remarkable properties quite different from its bulk counterpart, graphite [1].

The remarkable properties of graphene led to an explosion of interest in other vdW materials, one such group of vdW materials is the aforementioned family of TMDs. In the

---

[1]It would be quite cumbersome to have to know the laws of quantum mechanics before one is allowed to use a hammer.

case of TMDs, transition metal atoms *M* are sandwiched between chalcogen atoms *C*, forming a *C-M-C* atomic layer. The presence of different atoms inside the layers of TMDs makes it possible to further build different crystals due to, on the one hand, the different arrangement of atoms inside the layers and, on the other hand, the different stacking sequences of the layers as well as the relative orientation between adjacent layers.

TMD materials exhibit a wide range of tunability as a consequence of these *polytypes* [2–4]. In a very simplistic picture, the polytypes of the TMDs of interest in this thesis can be split into two groups that depend on the atomic coordination inside a layer, namely TMDs with *octahedral* and *trigonal prismatic* atomic coordination. The octahedral phase is more commonly known as the 1T (Tetragonal) phase (a distorted octahedral phase 1T' is also possible). The trigonal prismatic phase consists of two polytypes, the 2H (Hexagonal) and 3R (Rhombohedral) polytype; for all polytype phases, the digit indicates the amount of layers in the unit cell, and the letter indicates the type of symmetry exhibited. In this work we will mainly focus on two TMDs with trigonal prismatic atomic coordination: MoS_2 and WS_2. Other TMDs with similar properties as MoS_2 and WS_2 can be found by replacing the S atoms with Se or Te atoms. Interestingly, the coexistence of the 2H and 3R phases in a single crystal, termed *polytypism*, has also been observed for TMDs, resulting in another degree of tunability [5–9].

The remarkable sensitivity of the physical properties of TMDs with respect to their dimensionality (from bulk to two-dimensional (2D) and one-dimensional (1D) configurations) is one of the main driving forces motivating their detailed investigation [10, 11]. As a representative example, MoS_2 undergoes an indirect-to-direct bandgap transition when going from the bulk to monolayer form, as well as a change in band gap value [12]. In this respect, a field effect transistor has already been demonstrated with monolayer MoS_2 [13], showcasing the functionalities of TMDs in the monolayer limit. Monolayers of TMDs also provide a playground for nonlinear optics applications [14]. Furthermore, the application of strain to monolayers of TMDs can be used to further modulate their electronic and optical properties [15, 16].

Another interesting phenomenon present in these materials occurs when twisting layers of vdW materials with respect to each other, forming what are called Moiré superlattices. At certain rotation angles of the layers, the total structure has an ordered but non-periodic geometry, even though the atoms *inside* a layer follow a periodic structure. Twisted vdW layers offers another area of research where the electronic and optical properties of vdW materials can be tuned and explored by changing the rotation angle. The field of twisted vdW materials got its spark by the discovery of unconventional superconductivity in bilayers of graphene [17, 18], with now a burgeoning field consisting of other vdW materials including TMDs [19–21].

Low-Dimensional Edge-Filled Opportunities

In recent years one-dimensional structures, such as nanowires, have garnered ample interest due to their applicability as biological sensors, catalysts, and conductors [22–27]. In this regard, one-dimensional TMD-based nanostructures are promising candidates due to their intrinsic dimensional sensitivity. In particular, TMD layers exhibit a variety

1

of edge terminations as a consequence of a lack of inversion symmetry. The most common of these edge terminations, consisting of dangling bonds, are the armchair (AC) and the zigzag (ZZ) edge structures. Crucially, the appearance of these edge structures have a dramatic effect on the resulting electronic and magnetic properties of low-dimensional TMD structures [19, 28–31]; in the trigonal phase, nanoribbons with ZZ edge structures are predicted to be metallic and ferromagnetic, while AC terminated nanoribbons are predicted to be direct bandgap semiconductors.

The catalytic properties of TMD materials have also been demonstrated to be quite sensitivity to specific edge terminations. Indeed, combining a large amount of exposed edges with a low-dimensional nanostructure can be used to enhance the catalytic activity compared to a two-dimensional sheet. One-dimensional structures, such as core-shell nanowires based on TMDs, have displayed promise in the hydrogen evolution reaction (HER) and energy storage [32–36]. The core-shell geometry also highlights one of the possibilities of TMD-based heterostructures; the TMD shell can be used as a protective layer in acidic solutions, such is often the case in catalytic reactions. Finally, we note that optical properties such as nonlinear optical effects, single photon emission, and photovoltaic response all can be tuned by engineering specific edge structures and low-dimensional configurations of TMDs [37–41].

With these motivations, it is clear that the design and fabrication of TMDs nanostructures with novel morphologies that maximize the number of exposed active edge sites is a key aspect for further improvements in terms of applications. Realizing this goal requires correlating specific structural properties with their electronic and optical properties with the highest possible precision. It is with these considerations in mind that we continue with the specific aims of this work.

SCOPE, GOALS, AND JOURNEY

This thesis aims to combine materials science engineering, fabrication of structures at the nanoscale, state-of-the-art characterization, and *ab initio* calculations, focusing on the study of the morphological, electronic and optical properties of low-dimensional transition metal dichalcogenides (TMDs) nanostructures from both an experimental and theoretical point of view.

The experimental perspective consists on adapting well-established top-down approaches to fabricate novel types of low-dimensional TMD nanostructures with morphologies that cannot be obtained from traditional bottom-up methods. To create these TMD nanostructures, we employ several techniques such as exfoliation, focused ion beam milling (FIB), electron beam lithography (EBL), cryogenic deep reactive ion etching, and chemical vapor deposition (CVD).

The subsequent structural and optoelectronic characterization of these TMD nanostructures is then carried out by means of Transmission Electron Microscopy (TEM). In the TEM, structural characterization is determined by employing aberration corrected TEM along with energy-dispersive X-ray spectroscopy (EDX). The local electronic properties are examined by means of electron energy loss spectroscopy (EELS) in the TEM to map their electronic and optical behaviour with the associated structural properties.

Understanding the experimental results obtained for the novel TMD nanostructures fabricated in the course of this thesis strongly benefits from a complementary theoretical perspective based on first-principles calculation. In this thesis, we deploy a combination of density functional theory (DFT), many body perturbation theory, and dielectric response theory to illucidate many of the relevant physical properties of these novel low-dimensional TMD nanostructures, such as their band structure and their electron energy-loss distribution. In the following, we provide a brief outline summarising the main content of each of the chapters that compose this thesis.

CHAPTER 2
We start by presenting an overview of dielectric response theory and related theoretical methods, relevant for the interpretation of the electron energy-loss spectroscopy measurements. This chapter thus provides us with the theoretical foundations that will make possible a deeper understanding of the physical properties of the TMD nanostructures fabricated and studied in this thesis.

CHAPTER 3
In this chapter we characterize edge structures in thin layers of exfoliated MoS_2 flakes. We combine scanning TEM with the Geometrical Phase Analysis method to map the strain along the edges of the MoS_2 flakes. The analysis of high-resolution EEL spectra reveals strain present along the edge structures together with a broadening of exciton peaks near these edge structures.

CHAPTER 4
In this chapter we adapt a well-established top-down fabrication technique, FIB, in order to selectively pattern the two types of edges, armchair (AC) and zigzag (ZZ), within out-of-plane exfoliated MoS_2 flakes. The resulting nanostructures are denoted as "nanowalls". Precise control on the specific type of resulting edge structure, ZZ and AC, is achieved as confirmed by means of high-resolution TEM measurements, while EELS analyses demonstrate an edge-dependent response of these MoS_2 nanowalls. Additionally, DFT calculations confirms the metallic behaviour of a simple ZZ MoS_2 nanowall model.

CHAPTER 5
In Chapter 3 and Chapter 4 we used exfoliated MoS_2 to study edge-related properties in TMD nanostructures. Unfortunately, a fabrication strategy involving exfoliation and FIB does not readily scale up as required for industrial practical applications. In this chapter, we develop a novel strategy to fabricate Mo nanopillars, which achieves precise control of the aspect-ratio, morphology, and density of the fabricated nanostructures. The fabricated Mo nanopillars are then used as a template for the synthesis of core-shell Mo-MoS_2 nanopillars in Chapter 6.

CHAPTER 6
In this chapter we build upon the work of Chapter 5 and describe the synthesis of core-shell Mo-MoS_2 nanopillars using the fabricated Mo nanopillars as a template. The growth

1

of MoS_2 is verified by means of Raman spectroscopy, while the core-shell configuration is confirmed using high resolution TEM and EDX. The MoS_2 growth is further studied using FIB cross-section and SEM imaging. We further study the local electronic properties of the core-shell nanopillars with high-resolution EELS. In addition, the nonlinear response of the core-shell nanopillars is studied and an enhanced response as compared to reference MoS_2 is reported.

CHAPTER 7
In this chapter we deploy Density Functional Theory and perturbation theory in the GW approximation formalism to understand from the theoretical point of view the band structure and dielectric response of various polytypes of WS_2 in the trigonal phase and compare with experimental measurements. We find a clear difference in the band structure of the different polytypes, while the dielectric response shows very similar behaviour for the different polytypes.

CONCLUSION
We finish this thesis with an outlook on possible interesting routes for further study of nanostructured TMD materials realised in this work.

REFERENCES

[1] K. S. Novoselov, D. Jiang, F. Schedin, T. J. Booth, V. V. Khotkevich, S. V. Morozov, and A. K. Geim, *Two-dimensional atomic crystals,* Proceedings of the National Academy of Sciences **102**, 10451 (2005), https://www.pnas.org/content/102/30/10451.full.pdf .

[2] Y. Yu, G.-H. Nam, Q. He, X.-J. Wu, K. Zhang, Z. Yang, J. Chen, Q. Ma, M. Zhao, Z. Liu, F.-R. Ran, X. Wang, H. Li, X. Huang, B. Li, Q. Xiong, Q. Zhang, Z. Liu, L. Gu, Y. Du, W. Huang, and H. Zhang, *High phase-purity 1T-MoS_2- and 1T-$MoSe_2$-layered crystals,* Nature Chemistry **10**, 638 (2018).

[3] D. Voiry, A. Mohite, and M. Chhowalla, *Phase engineering of transition metal dichalcogenides,* Chem. Soc. Rev. **44**, 2702 (2015).

[4] R. Suzuki, M. Sakano, Y. J. Zhang, R. Akashi, D. Morikawa, A. Harasawa, K. Yaji, K. Kuroda, K. Miyamoto, T. Okuda, K. Ishizaka, R. Arita, and Y. Iwasa, *Valley-dependent spin polarization in bulk MoS_2 with broken inversion symmetry,* Nature Nanotechnology **9**, 611 (2014).

[5] L. Chen, H. Feng, R. Zhang, S. Wang, X. Zhang, Z. Wei, Y. Zhu, M. Gu, and C. Zhao, *Phase-Controlled Synthesis of 2H/3R-$MoSe_2$ Nanosheets on P-Doped Carbon for Synergistic Hydrogen Evolution,* ACS Applied Nano Materials **3**, 6516 (2020), https://doi.org/10.1021/acsanm.0c00988 .

[6] J.-U. Lee, K. Kim, S. Han, G. H. Ryu, Z. Lee, and H. Cheong, *Raman Signatures of Polytypism in Molybdenum Disulfide,* ACS Nano **10**, 1948 (2016), pMID: 26756836, https://doi.org/10.1021/acsnano.5b05831 .

[7] A. A. Puretzky, L. Liang, X. Li, K. Xiao, K. Wang, M. Mahjouri-Samani, L. Basile, J. C. Idrobo, B. G. Sumpter, V. Meunier, and D. B. Geohegan, *Low-Frequency Raman Fingerprints of Two-Dimensional Metal Dichalcogenide Layer Stacking Configurations,* ACS Nano **9**, 6333 (2015), pMID: 25965878, https://doi.org/10.1021/acsnano.5b01884 .

[8] S. E. van Heijst, M. Mukai, E. Okunishi, H. Hashiguchi, L. I. Roest, L. Maduro, J. Rojo, and S. Conesa-Boj, *Illuminating the Electronic Properties of WS₂ Polytypism with Electron Microscopy,* Annalen der Physik **n/a**, 2000499, https://onlinelibrary.wiley.com/doi/pdf/10.1002/andp.202000499 .

[9] L. I. Roest, S. E. van Heijst, L. Maduro, J. Rojo, and S. Conesa-Boj, *Charting the low-loss region in electron energy loss spectroscopy with machine learning,* Ultramicroscopy **222**, 113202 (2021).

[10] T. Eknapakul, P. D. C. King, M. Asakawa, P. Buaphet, R.-H. He, S.-K. Mo, H. Takagi, K. M. Shen, F. Baumberger, T. Sasagawa, S. Jungthawan, and W. Meevasana, *Electronic Structure of a Quasi-Freestanding MoS₂ Monolayer,* Nano Letters **14**, 1312 (2014), pMID: 24552197, https://doi.org/10.1021/nl4042824 .

[11] K. F. Mak, C. Lee, J. Hone, J. Shan, and T. F. Heinz, *Atomically Thin MoS₂: A New Direct-Gap Semiconductor,* Phys. Rev. Lett. **105**, 136805 (2010).

[12] A. Splendiani, L. Sun, Y. Zhang, T. Li, J. Kim, C.-Y. Chim, G. Galli, and F. Wang, *Emerging Photoluminescence in Monolayer MoS2,* Nano Letters **10**, 1271 (2010), https://doi.org/10.1021/nl903868w .

[13] B. Radisavljevic, A. Radenovic, J. Brivio, V. Giacometti, and A. Kis, *Single-layer MoS₂ transistors,* Nature Nanotechnology **6**, 147 (2011).

[14] X. Wen, Z. Gong, and D. Li, *Nonlinear optics of two-dimensional transition metal dichalcogenides,* InfoMat **1**, 317 (2019), https://onlinelibrary.wiley.com/doi/pdf/10.1002/inf2.12024 .

[15] A. Castellanos-Gomez, R. Roldán, E. Cappelluti, M. Buscema, F. Guinea, H. S. J. van der Zant, and G. A. Steele, *Local Strain Engineering in Atomically Thin MoS₂,* Nano Letters **13**, 5361 (2013), pMID: 24083520, https://doi.org/10.1021/nl402875m .

[16] C. Palacios-Berraquero, D. M. Kara, A. R. P. Montblanch, M. Barbone, P. Latawiec, D. Yoon, A. K. Ott, M. Loncar, A. C. Ferrari, and M. Atatüre, *Large-scale quantum-emitter arrays in atomically thin semiconductors,* Nature Communications **8**, 15093 (2017).

[17] Y. Cao, V. Fatemi, S. Fang, K. Watanabe, T. Taniguchi, E. Kaxiras, and P. Jarillo-Herrero, *Unconventional superconductivity in magic-angle graphene superlattices,* Nature **556**, 43 (2018).

1

[18] R. Bistritzer and A. H. MacDonald, *Moiré bands in twisted double-layer graphene,* Proceedings of the National Academy of Sciences **108**, 12233 (2011), https://www.pnas.org/content/108/30/12233.full.pdf .

[19] K. Yao, N. R. Finney, J. Zhang, S. L. Moore, L. Xian, N. Tancogne-Dejean, F. Liu, J. Ardelean, X. Xu, D. Halbertal, K. Watanabe, T. Taniguchi, H. Ochoa, A. Asenjo-Garcia, X. Zhu, D. N. Basov, A. Rubio, C. R. Dean, J. Hone, and P. J. Schuck, *Enhanced tunable second harmonic generation from twistable interfaces and vertical superlattices in boron nitride homostructures,* Science Advances **7** (2021), 10.1126/sciadv.abe8691, https://advances.sciencemag.org/content/7/10/eabe8691.full.pdf .

[20] Z. Zhang, Y. Wang, K. Watanabe, T. Taniguchi, K. Ueno, E. Tutuc, and B. J. LeRoy, *Flat bands in twisted bilayer transition metal dichalcogenides,* Nature Physics **16**, 1093 (2020).

[21] F. Wu, T. Lovorn, E. Tutuc, I. Martin, and A. H. MacDonald, *Topological Insulators in Twisted Transition Metal Dichalcogenide Homobilayers,* Phys. Rev. Lett. **122**, 086402 (2019).

[22] M. P. Zach, K. H. Ng, and R. M. Penner, *Molybdenum Nanowires by Electrodeposition,* Science **290**, 2120 (2000), https://science.sciencemag.org/content/290/5499/2120.full.pdf .

[23] P. K. Sahoo, R. Janissen, M. P. Monteiro, A. Cavalli, D. M. Murillo, M. V. Merfa, C. L. Cesar, H. F. Carvalho, A. A. de Souza, E. P. A. M. Bakkers, and M. A. Cotta, *Nanowire Arrays as Cell Force Sensors To Investigate Adhesin-Enhanced Holdfast of Single Cell Bacteria and Biofilm Stability,* Nano Letters **16**, 4656 (2016), pMID: 27336224, https://doi.org/10.1021/acs.nanolett.6b01998 .

[24] P. Chen, T. Zhou, M. Chen, Y. Tong, N. Zhang, X. Peng, W. Chu, X. Wu, C. Wu, and Y. Xie, *Enhanced Catalytic Activity in Nitrogen-Anion Modified Metallic Cobalt Disulfide Porous Nanowire Arrays for Hydrogen Evolution,* ACS Catalysis **7**, 7405 (2017), https://doi.org/10.1021/acscatal.7b02218 .

[25] V. Gautam, S. Naureen, N. Shahid, Q. Gao, Y. Wang, D. Nisbet, C. Jagadish, and V. R. Daria, *Engineering Highly Interconnected Neuronal Networks on Nanowire Scaffolds,* Nano Letters **17**, 3369 (2017), pMID: 28437614, https://doi.org/10.1021/acs.nanolett.6b05288 .

[26] D. J. Carrad, A. B. Mostert, A. R. Ullah, A. M. Burke, H. J. Joyce, H. H. Tan, C. Jagadish, P. Krogstrup, J. Nygård, P. Meredith, and A. P. Micolich, *Hybrid Nanowire Ion-to-Electron Transducers for Integrated Bioelectronic Circuitry,* Nano Letters **17**, 827 (2017), pMID: 28002672, https://doi.org/10.1021/acs.nanolett.6b04075 .

[27] Y. Zhao, J. T. Smith, J. Appenzeller, and C. Yang, *Transport Modulation in Ge/Si Core/Shell Nanowires through Controlled Synthesis of Doped Si Shells,* Nano Letters **11**, 1406 (2011), pMID: 21417251, https://doi.org/10.1021/nl1031138 .

[28] Y. Li, Z. Zhou, S. Zhang, and Z. Chen, *MoS$_2$ Nanoribbons: High Stability and Unusual Electronic and Magnetic Properties,* Journal of the American Chemical Society **130**, 16739 (2008), pMID: 19007118, https://doi.org/10.1021/ja805545x .

[29] K. Dolui, C. D. Pemmaraju, and S. Sanvito, *Electric Field Effects on Armchair MoS$_2$ Nanoribbons,* ACS Nano **6**, 4823 (2012), pMID: 22546015, https://doi.org/10.1021/nn301505x .

[30] H. Xu, S. Liu, Z. Ding, S. J. R. Tan, K. M. Yam, Y. Bao, C. T. Nai, M.-F. Ng, J. Lu, C. Zhang, and K. P. Loh, *Oscillating edge states in one-dimensional MoS$_2$ nanowires,* Nature Communications **7**, 12904 (2016).

[31] H. Zhang, X.-B. Li, and L.-M. Liu, *Tunable electronic and magnetic properties of WS$_2$ nanoribbons,* Journal of Applied Physics **114**, 093710 (2013), https://doi.org/10.1063/1.4820470 .

[32] N. Choudhary, C. Li, H.-S. Chung, J. Moore, J. Thomas, and Y. Jung, *High-Performance One-Body Core/Shell Nanowire Supercapacitor Enabled by Conformal Growth of Capacitive 2D WS$_2$ Layers,* ACS Nano **10**, 10726 (2016), pMID: 27732778, https://doi.org/10.1021/acsnano.6b06111 .

[33] X. Xia, J. Tu, Y. Zhang, X. Wang, C. Gu, X.-b. Zhao, and H. J. Fan, *High-Quality Metal Oxide Core/Shell Nanowire Arrays on Conductive Substrates for Electrochemical Energy Storage,* ACS Nano **6**, 5531 (2012), pMID: 22545560, https://doi.org/10.1021/nn301454q .

[34] Z. Chen, D. Cummins, B. N. Reinecke, E. Clark, M. K. Sunkara, and T. F. Jaramillo, *Core-shell MoO$_3$-MoS$_2$ Nanowires for Hydrogen Evolution: A Functional Design for Electrocatalytic Materials,* Nano Letters **11**, 4168 (2011), pMID: 21894935, https://doi.org/10.1021/nl2020476 .

[35] D. R. Cummins, U. Martinez, R. Kappera, D. Voiry, A. Martinez-Garcia, J. Jasinski, D. Kelly, M. Chhowalla, A. D. Mohite, M. K. Sunkara, and G. Gupta, *Catalytic Activity in Lithium-Treated Core-Shell MoO$_x$/MoS$_2$ Nanowires,* The Journal of Physical Chemistry C **119**, 22908 (2015), https://doi.org/10.1021/acs.jpcc.5b05640 .

[36] D. R. Cummins, U. Martinez, A. Sherehiy, R. Kappera, A. Martinez-Garcia, R. K. Schulze, J. Jasinski, J. Zhang, R. K. Gupta, J. Lou, M. Chhowalla, G. Sumanasekera, A. D. Mohite, M. K. Sunkara, and G. Gupta, *Efficient hydrogen evolution in transition metal dichalcogenides via a simple one-step hydrazine reaction,* Nature Communications **7**, 11857 (2016).

[37] M. A. Lukowski, A. S. Daniel, F. Meng, A. Forticaux, L. Li, and S. Jin, *Enhanced Hydrogen Evolution Catalysis from Chemically Exfoliated Metallic MoS$_2$ Nanosheets,* Journal of the American Chemical Society **135**, 10274 (2013), pMID: 23790049, https://doi.org/10.1021/ja404523s .

[38] Y. J. Zhang, T. Ideue, M. Onga, F. Qin, R. Suzuki, A. Zak, R. Tenne, J. H. Smet, and Y. Iwasa, *Enhanced intrinsic photovoltaic effect in tungsten disulfide nanotubes,* Nature **570**, 349 (2019).

1

[39] X. Yin, Z. Ye, D. A. Chenet, Y. Ye, K. O'Brien, J. C. Hone, and X. Zhang, *Edge Nonlinear Optics on a MoS$_2$ Atomic Monolayer,* Science **344**, 488 (2014), https://science.sciencemag.org/content/344/6183/488.full.pdf .

[40] K.-I. Lin, Y.-H. Ho, S.-B. Liu, J.-J. Ciou, B.-T. Huang, C. Chen, H.-C. Chang, C.-L. Tu, and C.-H. Chen, *Atom-Dependent Edge-Enhanced Second-Harmonic Generation on MoS$_2$ Monolayers,* Nano Letters **18**, 793 (2018), pMID: 29327927, https://doi.org/10.1021/acs.nanolett.7b04006 .

[41] M. Bolhuis, J. Hernandez-Rueda, S. E. van Heijst, M. Tinoco Rivas, L. Kuipers, and S. Conesa-Boj, *Vertically-oriented MoS$_2$ nanosheets for nonlinear optical devices,* Nanoscale **12**, 10491 (2020).

2

FIRST-PRINCIPLE METHODS FOR ELECTRON ENERGY-LOSS SPECTROSCOPY INTERPRETATION

Electron energy-loss spectroscopy (EELS) in the Transmission Electron Microscope (TEM) represents a powerful tool to understand the behaviour of both valence and core electrons of a material. Here we describe how dielectric response theory can be used to characterise the main features displayed by EEL spectra. In order to understand the experimentally acquired spectra, we deploy first-principle methods in the context of density functional theory (DFT) as implemented in the `WIEN2k` *package. Furthermore, we describe the GW approximation (GWA) as implemented in the* `GAP2` *code. These ab initio techniques are used through this thesis to compare and validate the corresponding experimental EELS results. Specifically in Chapter 4 for modelling Zigzag MoS$_2$ nanowalls and in Chapter 7 to accurately determine the band gap of polytypes of WS$_2$.*

2.1. Introduction

In this chapter we review the dielectric response of a material under an external perturbation. A brief description on how the microscopic and macroscopic dielectric functions are related to the energy-loss function, and subsequently, the electron energy-loss function. We continue with describing the dielectric function of *the free electron gas*, a simple model that can be used to qualitatively describe the phenomenon of *plasmons* in solids. We combine the different approaches as described in [1–7] to come to an understanding of dielectric theory.

We continue with describing the electronic and dielectric response of materials with calculations based on first principles methods. In this work we will be carrying out *ab initio* calculations of different crystal structure configurations by means of Density Functional Theory (DFT) [8, 9] using the WIEN2k software package [10, 11].

Furthermore, in order to obtain accurate estimates of the band gap associated with the different polytypes of WS_2 (to be described in Chapter 7), we describe the GW approximation as implemented in the GAP2 code by Jiang *et al.* [12, 13]. To this purpose, the output of the WIEN2k DFT calculations are used as input for the GW calculations in the GAP2 code. With this combination of the DFT and GW calculations we are able to evaluate the density of states (DOS), the band structure, the joint density of states (JDOS), and the energy-loss function (ELF) [5, 14, 15].

2.2. The Macroscopic Dielectric Function

The response of a solid under an external time-dependent electromagnetic perturbation can be described by a complex *dielectric tensor*. The complex dielectric tensor is directly related to the polarization of the solid by the external electromagnetic field. In the case of an isotropic solid and cubic crystal the dielectric tensor reduces to a scalar quantity in what is termed the dielectric function

$$\epsilon = \epsilon_1 + i\epsilon_2 \tag{2.1}$$

To find the dielectric function we start with making the distinction between the *microscopic* and *macroscopic* dielectric functions. The microscopic dielectric function is quantity one acquires from a quantum mechanical calculation. However, this is not the quantity one *measures* in experiments. The measured optical quantities are related to the macroscopic dielectric function.

The aim of the next sections is to describe the relation between the microscopic and macroscopic dielectric functions. We first start by describing how the macroscopic dielectric function can be evaluated in terms of its microscopic counterpart. The microscopic dielectric function relates the external potential $V^{ext}(\mathbf{r'})$ caused by an excitation at position $\mathbf{r'}$ and frequency ω to the total potential of the system $V^{total}(\mathbf{r}, \omega)$ at position $\mathbf{r}$ by [5, 14]

$$V^{\text{total}}(\mathbf{r}, \omega) = \int \epsilon^{-1}(\mathbf{r}, \mathbf{r'}, \omega) V^{\text{ext}}(\mathbf{r'}) d\mathbf{r'} \tag{2.2}$$

where $\epsilon^{-1}(\mathbf{r}, \mathbf{r'}, \omega)$ is the inverse dielectric tensor. It is useful to study Eq. (2.2) in reciprocal space with reciprocal lattice vectors $\mathbf{G}$, and $\mathbf{G'}$

$$V_{\mathbf{G}}^{\text{total}}(\mathbf{q}, \omega) = \sum_{\mathbf{G'}} \epsilon_{\mathbf{GG'}}^{-1}(\mathbf{q}, \omega) V_{\mathbf{G'}}^{\text{ext}}(\mathbf{q}, \omega) \qquad (2.3)$$

where $\mathbf{q}$ is the wavevector of the external excitation. In the case of an external perturbation caused by incident light, short wavelength components can be neglected and we assume that only long wavelength components contribute to the external potential; in the case of light in the optical regime, the wavelength of the incident light is much larger than the lattice spacing. In the long wavelength limit it is reasonable to assume that the external potential is uniform over the unit cell, i.e. a *constant*. In this case, only the $\mathbf{G'} = 0$ component survives in the sum in Eq. (2.3)

$$V_{\mathbf{G}}^{total}(\mathbf{q}, \omega) = \epsilon_{\mathbf{G}0}^{-1}(\mathbf{q}, \omega) V_{0}^{ext}(\mathbf{q}, \omega) \qquad (2.4)$$

The macroscopic quantities we are interested in $V_{M}^{total}(\mathbf{q}, \omega)$ are connected to the average of the total potential in the unit cell $V_{\mathbf{G}}^{total}(\mathbf{q}, \omega)$,

$$V_{M}^{total}(\mathbf{q}, \omega) = \langle V_{\mathbf{G}}^{total}(\mathbf{q}, \omega) \rangle_{\mathbf{G'}=0} \qquad (2.5)$$

The macroscopic potential is determined by taking the $\mathbf{G} = 0$ component. We see then that the macroscopic potential is related to the average of the microscopic dielectric tensor in Eq. (2.4) by

$$V_{M}^{\text{total}}(\mathbf{q}, \omega) = \langle \epsilon_{\mathbf{GG'}}^{-1}(\mathbf{q}, \omega) \rangle_{\mathbf{G}=0, \mathbf{G'}=0} V_{0}^{\text{ext}}(\mathbf{q}, \omega) \qquad (2.6)$$

From Eq 2.6 we see that the macroscopic dielectric tensor is given by

$$\epsilon_{M}^{-1}(\mathbf{q}, \omega) = \langle \epsilon_{\mathbf{G}, \mathbf{G'}}^{-1}(\mathbf{q}, \omega) \rangle_{\mathbf{G}=0, \mathbf{G'}=0} \qquad (2.7)$$

In other words, the macroscopic dielectric function is found by calculating the inverse microscopic dielectric function up to a certain cut-off $\mathbf{G}$. Let us summarize the main findings of this discussion. With the considerations above, the macroscopic dielectric function is evaluated by

- calculating the microscopic dielectric function $\epsilon_{\mathbf{G}, \mathbf{G'}}$ up to a certain cut-off

- inverting the microscopic dielectric function $\epsilon_{\mathbf{G}, \mathbf{G'}}^{-1}$

- average over the microscopic dielectric function $\epsilon_{\mathbf{G}, \mathbf{G'}}^{-1}$ by taking the $\mathbf{G} = \mathbf{G'} = 0$ components $\langle \epsilon_{\mathbf{G}, \mathbf{G'}}^{-1}(\mathbf{q}, \omega) \rangle_{\mathbf{G}=0, \mathbf{G'}=0}$

- invert $\langle \epsilon_{\mathbf{G}, \mathbf{G'}}^{-1}(\mathbf{q}, \omega) \rangle_{\mathbf{G}=0, \mathbf{G'}=0}$ to acquire the macroscopic dielectric function

The above procedure results in a macroscopic dielectric function that describes the response of a solid that includes short wavelength components even in the presence of an external potential with long wavelength variations in space. The shorter wavelength components are termed *local field effects*. In practice, it is easier to first take the $\mathbf{G} = \mathbf{G}' = 0$ component of the inverse microscopic dielectric function, and then inverting the found quantity to find the macroscopic dielectric function, i.e.

$$\epsilon_M^{-1}(\mathbf{q}, \omega) = (\epsilon_{\mathbf{0}, \mathbf{0}}(\mathbf{q}, \omega))^{-1} \neq \langle \epsilon_{\mathbf{G}, \mathbf{G}'}^{-1}(\mathbf{q}, \omega) \rangle_{\mathbf{G}=0, \mathbf{G}'=0} \tag{2.8}$$

Effectively, this means averaging the response function over the unit cell and neglecting local field effects. For bulk solids and long wavelength external perturbations Eq. (2.8) give reasonable results [14]. However, care has to be taken when considering the response of nanostructures, as well as short wavelength perturbations, such as those caused by X-rays or fast electrons [2–4, 6, 14].

2.3. The Microscopic Dielectric Function

In the previous discussion we have seen how the dielectric tensor not only depends on the frequency ω of the external perturbation, but it also depends on the wavevector $\mathbf{q}$ of the external perturbation. We start here with defining the generalized microscopic dielectric tensor and then apply the approximations given at the end of the previous section. The microscopic dielectric tensor is given by [16]

$$\epsilon(\mathbf{r}, t; \mathbf{r}', t') = \delta(\mathbf{r} - \mathbf{r}')\delta(t - t') - \int P(\mathbf{r}, t; \mathbf{r}'', t')\nu(\mathbf{r}'' - \mathbf{r})d\mathbf{r}'' \tag{2.9}$$

where $\nu(\mathbf{r}'' \text{-} \mathbf{r}')$ is the bare Coulomb interaction and P is the polarization propagator. The polarization propagator in this case is restricted to the random phase approximation, which leads to the expression

$$\epsilon_{\mathbf{G}, \mathbf{G}'}(\mathbf{q}, \omega) = \delta_{\mathbf{G}, \mathbf{G}'} - \nu(\mathbf{q} + \mathbf{G})P_{\mathbf{G}, \mathbf{G}'}^0(\mathbf{q}, \omega) \tag{2.10}$$

where the polarization propagator $P_{\mathbf{G}, \mathbf{G}'}^0(\mathbf{q}, \omega)$ is given by

$$P_{\mathbf{G}, \mathbf{G}'}^0(\mathbf{q}, \omega) = \frac{1}{\Omega_c} \sum_{n', n, \mathbf{k}} \frac{f_0(E_{n, \mathbf{k}+\mathbf{q}}) - f_0(E_{n', \mathbf{k}})}{E_{n, \mathbf{k}+\mathbf{q}} - E_{n', \mathbf{k}} - \omega} M_{n', n}^{\mathbf{G}}(\mathbf{k}, \mathbf{q})^* M_{n', n}^{\mathbf{G}'}(\mathbf{k}, \mathbf{q}) \tag{2.11}$$

where $f_0(E_{n', \mathbf{k}})$ is the Fermi-Dirac distribution, Ω is the volume of the crystal. n' and n are the band indices for unoccupied and occupied bands, respectively. $M_{n', n}(\mathbf{k})$ is the momentum matrix element relating the transition from a filled level n of one band to the unoccupied band n' at a given $\mathbf{k}$ within the Brillouin zone. The matrix elements $M_{n', n}^{\mathbf{G}}(\mathbf{k}, \mathbf{q})$ are given by

$$M_{n', n}^{\mathbf{G}}(\mathbf{k}, \mathbf{q}) = \langle n', \mathbf{k}| e^{-i(\mathbf{q}+\mathbf{G})\cdot\mathbf{r}} |n, \mathbf{k} + \mathbf{q} \rangle \tag{2.12}$$

with the Bloch states $|n', \mathbf{k}\rangle$ in the real space representation given by

$$\langle \mathbf{r} | n', \mathbf{k} \rangle = \frac{1}{\sqrt{\Omega_c}} u_{\mathbf{k},n'}(\mathbf{r}) e^{i\mathbf{k}_{n'} \cdot \mathbf{r}} \tag{2.13}$$

where the modulation function $u_{\mathbf{k},n'}$ shares the periodicity of the solid and Ω_c is the unit cell volume. By solving the set of equations Eqns. (2.10)-(2.13) one can then calculate the dielectric function in the random phase approximation. Under the influence of an external perturbation, be it light or electrons, the microscopic dielectric function is in general a function of the frequency ω and momentum wave vector $\mathbf{q}$ of the perturbation $\epsilon(\mathbf{q}, \omega)$. We adopt the *Independent Particle Approximation* (IPA) and examine the case where $\mathbf{q} = 0$, which is what one assumes when one neglects the electron-hole interaction during the absorption process for a long wavelength external perturbation leading to a uniform external potential over the unit cell. We further neglect local field effects inside the unit cell. In such a case, the imaginary part of the dielectric function is given by (with $\mathbf{G} = \mathbf{G}' = 0$) [2]

$$\epsilon_2(0, \omega) = \frac{4\pi^2 e^2}{m^2 \omega^2} \sum_{n,n'} \int \frac{2}{(2\pi)^3} d^3\mathbf{k} |M_{n',n}(\mathbf{k})|^2 \delta(E_n(\mathbf{k}) - E_{n'}(\mathbf{k}) - \hbar\omega) \tag{2.14}$$

If the matrix elements show no $\mathbf{k}$ dependence, then the imaginary part of the dielectric function reads

$$\epsilon_2(0, \omega) \propto |M_{n',n}|^2 \times J_{n',n}(\hbar\omega) \tag{2.15}$$

where $J_{n',n}(\hbar\omega)$ is the joint density of states of the occupied and unoccupied states with energy difference $\hbar\omega$. In this approximation we can see that the imaginary part of the dielectric function can be directly connected to the band structure of the solid by way of the joint density of states. Once we have the imaginary part of the dielectric function, the real part can be calculated via the *Kramers-Kronig* relations

$$\epsilon_1(\omega) - 1 = \frac{1}{\pi} \mathscr{P} \int_{-\infty}^{\infty} \frac{\epsilon_2(\omega')}{\omega' - \omega} d\omega' \tag{2.16}$$

$$\epsilon_2(\omega) = \frac{1}{\pi} \mathscr{P} \int_{-\infty}^{\infty} \frac{\epsilon_1(\omega') - 1}{\omega' - \omega} d\omega' \tag{2.17}$$

where $\mathscr{P}$ is the Cauchy principle value of the integral. Having found the real and imaginary parts of the dielectric function the energy loss function can be calculated using the dielectric function

$$\Gamma_{ELF}(\omega) = \text{Im}\left[\frac{-1}{\epsilon(\omega)} \right] = \frac{\epsilon_2}{\epsilon_1^2 + \epsilon_2^2} \tag{2.18}$$

The relation Eq. (2.18) is related to the energy lost by long-wavelength electromagnetic radiation after interaction with a solid. In the next section we will see how the energy loss function is related to electron energy-loss spectroscopy.

2.4. The Dielectric Connection with EELS

In this section we give a brief sketch on the connection between dielectric response theory and electron energy-loss spectroscopy. For simplicity, we describe the non-retarded approximation, as is given in [1, 4]. In electron energy-loss spectroscopy one measures the energy-loss of an external electron after it has interacted with a solid. Effectively, one measures how the solid has slowed down the external electrons during the electron-solid interaction. An electron traveling along a straight-line trajectory $\mathbf{r} = \mathbf{r}_e(t)$ with a velocity $\mathbf{v}$ experiences an energy loss ΔE due to an induced electric field in the solid $\mathbf{E}^{ind}$ acting back on the external electron

$$\Delta E = e \int dt \mathbf{v} \cdot \mathbf{E}^{ind}[\mathbf{r}_e(t), t] = \int_0^\infty \hbar\omega d\omega \Gamma_{EELS}(\omega) \tag{2.19}$$

with

$$\Gamma_{EELS}(\omega) = \frac{e}{\pi\hbar\omega} \int dt \mathrm{Re}\{e^{-i\omega t}\mathbf{v} \cdot \mathbf{E}^{ind}[\mathbf{r}_e, t]\} \tag{2.20}$$

The loss probability $\Gamma(\omega)$ is given per unit of transferred frequency ω. The problem then lies in finding the induced electric field that the external electron generates $\mathbf{E}^{ind}$. For what follows, we use Poisson's equation in the non-retarded approximation. For simplicity let us assume that the electrons travel along the z-axis, such that $\mathbf{r}_e(t) = \mathbf{r}_0 + \mathbf{v}t$, $\mathbf{v} = v\hat{\mathbf{z}}$. Poisson's equation states that the electric field $\mathbf{E}(\mathbf{r},\omega)$ generated at position $\mathbf{r}$ by a potential $V(\mathbf{r},\omega)$ is related to the charge density $\rho(\mathbf{r},\omega)$ by

$$\mathbf{E}(\mathbf{r},\omega) = -\nabla V(\mathbf{r},\omega) \tag{2.21}$$

and

$$\nabla^2 V(\mathbf{r},\omega) = -\frac{\rho(\mathbf{r},\omega)}{\epsilon_0} \tag{2.22}$$

The potential V consists of the screened interaction $W(\mathbf{r},\mathbf{r}',\omega)$ at the point $\mathbf{r}$ by a unit charge located at $\mathbf{r}'$ and the charge density of a moving electron. The potential is given by

$$V(\mathbf{r},\omega) = -\frac{e}{v} \int dz' W(\mathbf{r}, \mathbf{R}_0, z', \omega) e^{i\omega(z'-z_0)/v} \tag{2.23}$$

where $\mathbf{R}_0$ is the electron impact parameter. Using Eq.(2.21) on Eq.(2.23) we find that the electron energy-loss probability is given by (and remembering that we only have an electron moving along the z-axis)

$$\Gamma_{EELS}(\mathbf{R}_0, \omega) = \frac{e^2}{\pi \hbar v^2} \int dz dz' \cos\left[\frac{\omega(z-z')}{v}\right] \times \text{Im}\{-W(\mathbf{R}_0, z, \mathbf{R}_0, z', \omega)\} \qquad (2.24)$$

where W is the frequency-dependent screened interaction. The above describes a semi-classical approach to connect the dielectric properties and energy loss function to EELS. A full quantum mechanical description of the solid and external electrons yields [17]

$$\Gamma_{EELS}(\omega) = \int d^2\mathbf{R} |\psi_{i\perp}(\mathbf{R})|^2 \Gamma_{EELS}(\mathbf{R}, \omega) \qquad (2.25)$$

where $\Gamma_{EELS}(\mathbf{R}, \omega)$ is the energy-loss in the classical dielectric formalism, and $\psi_{i\perp}(\mathbf{R})$ is the component of the incident electron wave function perpendicular to the electron beam direction. Eq. (2.25) tells us that the energy-loss can be described by using the energy-loss formulation in the classical dielectric formalism weighted by the intensity of the electron beam spot $|\psi_{i\perp}(\mathbf{R})|^2$ as long as all the inelastic signal is collected by the spectrometer. To calculate the energy-loss one needs to find a model for the screened interaction W. It is here where the dielectric response comes into the picture. Describing the screened interaction using the dielectric function as described in the previous sections yields a reliable measure of the electron energy-loss. In the case of a homogeneous medium in the non-relativistic limit the electron energy-loss of a bulk material is given by

$$\Gamma_{bulk}(\omega) = \frac{2e^2 L}{\pi \hbar v^2} \text{Im}\left\{\frac{-1}{\epsilon}\right\} \ln(q_c v/\omega) \qquad (2.26)$$

where it is assumed that the dielectric function has no $\mathbf{q}$ dependence as in the $\epsilon(o, \omega)$ description in the previous section and L is the thickness of the solid. Eq. (2.26) is valid when low enough momentum transfer is collected below a cutoff momentum q_c. We have now arrived at the connection between dielectric theory and the energy-loss of an external electron. It is instructive to see what this dielectric formalism can tell us by studying a simple model for the dielectric function ϵ. In the next section we will describe the dielectric function of a free electron gas and comment on the observable features of this model.

2.5. THE FREE ELECTRON GAS

The free electron gas can be used to give a qualitative feel of the phenomena that one can observe in the context of the dielectric response of a material. The qualitative behaviour of the valence electrons in a solid can be described as a set of coupled oscillators, which are considered as almost free particles. The equation of motion that describes the response of a "quasi free" electron with effective mass m, and damping constant Γ to a local electric field $\mathbf{E}$ is given by

$$m\ddot{\mathbf{x}} + m\Gamma\dot{\mathbf{x}} = -e\mathbf{E} \tag{2.27}$$

In the presence of a an oscillating external field $\mathbf{E} = \mathbf{E}e^{-i\omega t}$ the dielectric function for the free electron gas is given by

$$\epsilon(\omega) = \epsilon_1 + i\epsilon_2 = 1 - \frac{\omega_p^2}{\omega^2 + \Gamma^2} + \frac{i\Gamma\omega_p^2}{\omega(\omega^2 + \Gamma^2)} \tag{2.28}$$

where the plasma resonance frequency ω_p is a function of the valence electron density n

$$\omega_p = \sqrt{\frac{ne^2}{\epsilon_0 m}} \tag{2.29}$$

The transmitted external electron causes a collective excitation of the valence electrons with energy $E_p = \hbar\omega_p$, called a *plasmon*. By using the relation $E = \hbar\omega$ the energy loss function of the free electron gas can be written as

$$\mathrm{Im}\left\{\frac{-1}{\epsilon(E)}\right\} = \frac{E_p^2(E\hbar/\tau)}{(E^2 - E_p^2)^2 + (E\hbar/\tau)^2} \tag{2.30}$$

where $\tau = 1/\Gamma$ is the relaxation time of plasma oscillations. In practice, we do not deal with perfect infinite crystals. One has to take into account the presence of *interfaces* between two or multiple media. For simplicity, let us assume a slab of the solid of interest is in vacuum, such is the case for TEM-EELS measurements. In this case, a collective excitation is formed at the surface of the solid, and is termed a *surface plasmon*. The energy of the surface plasmon in the free electron gas is given by

$$\omega_s = \frac{\omega_p}{\sqrt{2}} \tag{2.31}$$

The free electron gas model for the dielectric response describes qualitatively quite well the sharp plasmon resonances of materials, and is a quite good estimation in the case of Al [2, 6]. A more accurate description of the dielectric response can be done by expanding the free electron gas model by including the effects of bound electrons, or carrying out a full quantum mechanical calculation. We have seen how dielectric response theory and EELS are connected, and how dielectric theory in the free electron gas can describe the existence of collective excitations. A natural extension is to use EELS to study other optical phenomena such as excitons, polaritons, and interband transitions of materials [2, 6, 18, 19].

2.6. Density Functional Theory

In the previous sections we described dielectric response theory and its connection to electron energy-loss spectroscopy. In order to use dielectric theory, it is important to use wavefunctions that accurately describe the solid of interest. One popular approach is to use *Density Functional Theory* (DFT). We start with defining the total energy of a system in DFT using the Born-Oppenheimer approximation [8–11, 20]:

$$E_{\text{tot}} = T_S + E_{\text{en}} + E_H + E_{xc} + E_{nn}, \tag{2.32}$$

where T_S is the kinetic energy of the electrons in the system, E_{en} is the electron-nucleus energy, E_H is the Hartree energy, E_{xc} is the exchange-correlation energy, and E_{nn} is the nucleus-nucleus energy. In this form all the many-body interactions are lumped into the exchange-correlation term E_{xc}. The ground state energy of the system is obtained by minimizing the total energy with respect to the total density $\rho(\mathbf{r})$

$$\frac{\delta E_{\text{tot}}(\mathbf{r})}{\delta \rho(\mathbf{r})} \tag{2.33}$$

where the density of the electrons $\rho(\mathbf{r})$ is given by

$$\rho(\mathbf{r}) = \sum_{i=1}^{N} |\psi_i(\mathbf{r})|^2 \tag{2.34}$$

$$\int d^3\mathbf{r}\rho(\mathbf{r}) = N \tag{2.35}$$

and the sum is over N orbitals $\psi_i(\mathbf{r})$, such that the constraint Eq. (2.35) is fulfilled where N is the total amount of electrons in the system. Minimizing the energy functional with the constraints above yields the Kohn-Sham equations

$$\left(-\frac{1}{2}\nabla^2 + V_{KS}\right)\psi_i(\mathbf{r}) = E_i\psi_i(\mathbf{r}) \tag{2.36}$$

where the Kohn-Sham potential V_{KS} is defined by

$$V_{KS}(\mathbf{r}) \equiv V_{en}(\mathbf{r}) + V_H(\mathbf{r}) + V_{xc}(\mathbf{r}) \tag{2.37}$$

and is the sum of the electron-nucleus $V_{en}(\mathbf{r})$, Hartree $V_H(\mathbf{r})$, and exchange-correlation (XC) $V_{xc}(\mathbf{r})$ potentials. In order to obtain the Kohn-Sham energies E_i and wavefunctions $\psi_i(\mathbf{r})$ an iterative procedure is carried out where 1) a trial electron density is used, 2) the trial density is used to solve the Kohn-Sham equations to obtain ψ_i, 3) the electron density with the obtained ψ_i are calculated and 4) compare the trial and calculated electron densities [21]. The whole procedure is repeated should the trial density and calculated

electron densities not match. A new trial density is formed by mixing the original trial density with the calculated electron density [10, 11, 21].

In order to solve the Kohn-Sham equations, one needs to find a potential functional which accurately describes the system of interest. A popular approach is to formulate a potential functional which is a simple function of the density itself, in what is called the *Local Density Approximation*(LDA). Another approach is to use potential functionals which consists of gradients of the density to correct for the non-homogeneity of the true electron density, in what is called the *Generalized Gradient Approximations*. The LDA and GGA frameworks are inadequate in describing the van der Waals interaction, namely the mathematical formulation of the functionals in the LDA and GGA frameworks are *local*. The van der Waals interaction is an essentially *nonlocal* effect. The non-local effects can be seen in the decay of the interaction energy of the different types of functionals, i.e. the van der Waals interaction leads to a decay in interaction energy proportional to r^{-6}, while the interaction energy in the local functionals decay approximately exponentially.

One possible way to correct for the non-local dispersion due to the van der Waals interaction is to introduce an empirical correction in the DFT calculations. The empirical correction obeys then the r^{-6} decay, while an appropriate damping should be introduced for correct accounting of the interactions when going from short-range to the long-range correlations [10, 11, 22–26]. While introducing an empirical correction in DFT to account for the van der Waals interaction has been quite successful, another approach is to introduce a nonlocal correlation-energy term, which is given by

$$E_c^{nl} = \frac{1}{2} \int d^3 r d^3 r' n(\mathbf{r}) \phi(\mathbf{r}, \mathbf{r}') n(\mathbf{r}') \tag{2.38}$$

where the kernel $\phi(\mathbf{r}, \mathbf{r}')$ accounts for the long-range correlation in an appropriate manner. The kernel is a function of the electron density, the derivative of the electron density, and on the distance $|\mathbf{r} - \mathbf{r}'|$. The double integration in Eq. (2.38) results in a computationally expensive procedure and improvements in implementation of the double integration has made calculations with large supercells feasible [27].

2.7. Implementation in WIEN2k

In this work we use the WIEN2k DFT package [10, 11], where a linearized augmented plane waves complemented by local orbitals (LAPW+lo) method is used to generate the basis set for the wavefunctions. In this method, the solid of interest is divided into an atomic region and an interstitial region. The basic idea of the LAPW+lo method as implemented in WIEN2k is to set up a basis of linearized plane waves inside the atomic region which includes local orbitals to properly account for the radial function variations. In atom t the atomic region basis set is formed by a linear combination of local atomic orbitals,

$$\phi_{tlm}^{lo} = \left[A_{tlm}^{lo} u_{tl}(r, E_{tl}) + B_{tlm}^{lo} \dot{u}_{tl}(r, E_{tl}) \right] Y_{lm}(\hat{\mathbf{r}}) \tag{2.39}$$

where $u_{tl}(r, E_{tl})$ are radial wavefunctions of atom t, $\dot{u}_{tl}(r, E_{tl})$ is the first energy deriva-tive of $u_{tl}(r, E_{tl})$ and $Y_{lm}(\hat{\mathbf{r}})$ are spherical harmonics. The local orbitals are zero outside the atomic region, and together with the condition of normalization of ϕ_{tlm}^{lo}, sets restric-tions on the values of the coefficients A_{tlm}^{lo} and B_{tlm}^{lo}. The unit cell is partitioned into atomic regions and interstitial regions, where in the interstitial regions a plane wave ex-pansion is used

$$\phi_{\mathbf{k}_n}^{\text{LAPW}} = \begin{cases} \sum_{l,m} \left[A_{tlm}^{\mathbf{k}_n} u_{tl}(r, E_{tl}) + B_{tlm}^{\mathbf{k}_n} \dot{u}_{tl}(r, E_{tl}) \right] Y_{lm}(\hat{\mathbf{r}}) & \text{inside sphere} \\ \frac{1}{\sqrt{\omega}} e^{i\mathbf{k}_n \cdot \mathbf{r}} & \text{interstitial region} \end{cases} \tag{2.40}$$

where $\mathbf{k}_n = \mathbf{k} + \mathbf{K}_n$. $\mathbf{K}_n$ are the reciprocal lattice vectors and $\mathbf{k}$ is the wave vector inside the first Brillouin zone. At the atomic sphere boundary the $\phi_{\mathbf{k}_n}^{\text{LAPW}}$ and its derivative are continuous, setting a restriction for the coefficients $A_{tlm}^{\mathbf{k}_n}$ and $B_{tlm}^{\mathbf{k}_n}$. The potential in this basis is set is expanded

$$V(\mathbf{r}) = \begin{cases} \sum_{l,m} V_{l,m} Y_{l,m}(\mathbf{r}) & \text{inside sphere} \\ \sum_{\mathbf{K}} V_{\mathbf{K}} e^{i\mathbf{K} \cdot \mathbf{r}} & \text{outside sphere} \end{cases} \tag{2.41}$$

Finally, the Kohn-Sham orbitals can be expanded, with band index n

$$\Psi_{n\mathbf{k}} = \sum_i c_{n\mathbf{k}}^i \phi_i, \tag{2.42}$$

where the coefficients $c_{n\mathbf{k}}^i$ can be found by solving the Kohn-Sham equations following the restrictions imposed in the previous section.

2.8. GW APPROXIMATION

One limitation of the DFT approach that often arises is the band gap problem [28, 29]. Calculations on the DFT level often underestimates or overestimates the band gap values of solids, and in some cases predicts insulating behaviour for known metals or vice versa. Several approaches exist that aim to ameliorate the band gap problem, including the use of semi-local potentials in the DFT calculations [28]. Another popular approach is the *GW approximation* [16], which involves using a one-particle Green's function approach to calculate accurate band structures for insulators and semiconductors as described by Hedin [16]. The *GW* approximation uses the one-particle Green's function G together with the dynamically screened Coulomb interaction W to calculate self-energy correc-tions to the KS ground state energy.

Here we briefly describe the GW approximation in the $G_0 W_0$ scheme using the random-phase approximation (RPA). The interacting single-particle Green's function $G(\mathbf{r}, \mathbf{r}'; \omega)$ corresponding to quasi-particle energies $E_{n\mathbf{k}}^{QP}$ is given by
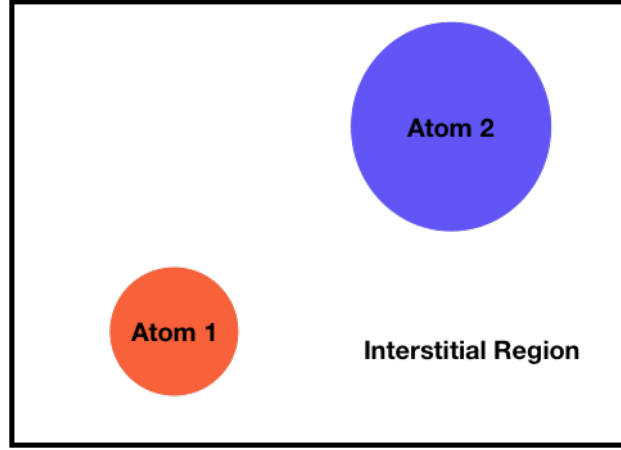
Figure 2.1: In the `WIEN2k` package, the basis functions are defined by separating the atomic and interstitial regions. The atomic regions are then described by linear combinations of atomic orbitals, while the interstitial region is instead described by an expansion in terms of plane waves.

$$G(\mathbf{r}, \mathbf{r}', \omega) = \sum_{n\mathbf{k}} \frac{\psi_{n\mathbf{k}}(\mathbf{r})\psi_{n\mathbf{k}}^*(\mathbf{r}')}{\omega - E_{n\mathbf{k}}^{QP}} \tag{2.43}$$

where $\psi(\mathbf{r})_{n\mathbf{k}}$ are the KS wavefunctions and $\mathbf{k}$ is the Bloch wavevector in the first Brillouin zone. The poles in the Green's functions represented by $E_{n\mathbf{k}}^{QP}$ can be calculated by solving the quasi-particle equation

$$\left[\frac{1}{2}\nabla^2 + V_{ext}(\mathbf{r}) + V_H(\mathbf{r})\right]\Psi_{n\mathbf{k}}(\mathbf{r}) + \int \Sigma(\mathbf{r}, \mathbf{r}'; E_{n\mathbf{k}}^{QP})\Psi_{n\mathbf{k}}(\mathbf{r})d\mathbf{r}' = E_{n\mathbf{k}}^{QP}\Psi_{n\mathbf{k}}(\mathbf{r}) \tag{2.44}$$

where $\Sigma(\mathbf{r}, \mathbf{r}'; E_{n\mathbf{k}}^{QP})$ is the self-energy which contains all the electron-electron interactions, and $\Psi_{n\mathbf{k}}(\mathbf{r})$ is the quasi-particle wavefunction. The external and Hartree potentials are given by $V_{ext}(\mathbf{r})$ and $V_H(\mathbf{r})$, respectively. The self-energy is given by

$$\Sigma(\mathbf{r}, \mathbf{r}'; \omega) = \frac{i}{2\pi}\int G(\mathbf{r}, \mathbf{r}'; \omega + \omega')W(\mathbf{r}', \mathbf{r}, \omega')e^{i\omega'\eta}d\omega' \tag{2.45}$$

where η is an infinitesimal positive number and $W(\mathbf{r}', \mathbf{r}, \omega')$ is the dynamically screened Coulomb potential. In general, the self-energy is non-Hermitian, where the real part of the self-energy represents the single-particle excitation energies and the excitation lifetime is related to the imaginary part of the self-energy. The dynamically screened Coulomb potential can be found by solving the following sets of equations [16, 30–34]

$$W(\mathbf{r}', \mathbf{r}, \omega') = v(\mathbf{r}, \mathbf{r}') + \int\int v(\mathbf{r}, \mathbf{r}_1)P(\mathbf{r}_1, \mathbf{r}_2; \omega)W(\mathbf{r}_2, \mathbf{r}')d\mathbf{r}_1 d\mathbf{r}_2 \tag{2.46}$$

$$P(\mathbf{r},\mathbf{r}';\omega) = -\frac{1}{2\pi}\int G(\mathbf{r},\mathbf{r}';\omega+\omega')G(\mathbf{r}',\mathbf{r};\omega')e^{i\omega'\eta}d\omega' \tag{2.47}$$

where the bare Coulomb potential is given by $v(\mathbf{r},\mathbf{r}') = 1/|\mathbf{r}-\mathbf{r}'|$ and $P(\mathbf{r},\mathbf{r}';\omega)$ is the polarizability or polarization propagator in the RPA [16], i.e. a one-particle Green function is used to describe the polarization. The above procedure calculates the quasi-particle energies using the G and W in a one shot calculation as a first-order correction to the KS ground state, and is termed the G_0W_0 scheme in the GW approximation. A fully self-consistent approach involving multiple iterative calculations of the G and W terms can be carried out by following Hedin's equations in combination with Dyson equations [16, 30–33]. With the above considerations the quasi-particle corrected energy to the KS energy E_i^{KS} is given by

$$E_{n\mathbf{k}}^{QP} = E_{n\mathbf{k}}^{KS} + Z_{n\mathbf{k}}\langle\psi_{n\mathbf{k}}|\Sigma_{xc}(E_{n\mathbf{k}}^{KS}) - V_{xc}|\psi_{n\mathbf{k}}\rangle \tag{2.48}$$

where the KS exchange-correlation potential is given by V_{xc} and the quasi-particle renormalization factor $Z_{n\mathbf{k}}$ is given by

$$Z_{n\mathbf{k}} \equiv \left(1 - \frac{\partial[\Sigma_{xc}(E)]_{n\mathbf{k}}}{\partial E}\right)^{-1}\bigg|_{E=E_{n\mathbf{k}}^{KS}} \tag{2.49}$$

In this thesis, the GW calculations are carried out using the GAP2 code [12, 13], an all-electron GW code interfaced with WIEN2k. The GW calculations are carried out on an equally spaced k-mesh using an auxiliary basis set $\chi_i^{\mathbf{q}}(\mathbf{r})$ where

$$\psi_{n\mathbf{k}}(\mathbf{r})\psi_{m\mathbf{k}-\mathbf{q}}^*(\mathbf{r}) = \sum_i M_{nm}^i(\mathbf{k},\mathbf{q})\chi_i^{\mathbf{q}}(\mathbf{r}) \tag{2.50}$$

$$M_{nm}^i(\mathbf{k},\mathbf{q}) = \int_\Omega \left[\chi_i^{\mathbf{q}}(\mathbf{r})\psi_{m\mathbf{k}-\mathbf{q}}^*(\mathbf{r})\right]^*\psi_{n\mathbf{k}}(\mathbf{r})d\mathbf{r} \tag{2.51}$$

defines a product basis set using the KS orbitals and Ω is the unit cell volume. QP energies at k-points that are not considered in the original GW calculations are obtained using the Fourier interpolation approach [35]. The wavefunctions acquired from the GW calculations are then used to calculate the density of states, band structure, and energy-loss function [14].

REFERENCES

[1] R. H. Ritchie, *Plasma losses by fast electrons in thin films*, Phys. Rev. **106**, 874 (1957).

[2] H. Raether, *Excitation of Plasmons and Interband Transitions by Electrons* (Springer Tracts in Modern Physics, 1980).

[3] R. Egerton, *Electron-Energy Loss Spectroscopy in the Electron Microscope* (Springer, 1980).

[4] F. J. García de Abajo, *Optical excitations in electron microscopy,* Rev. Mod. Phys. **82**, 209 (2010).

[5] C. Ambrosch-Draxl and J. O. Sofo, *Linear optical properties of solids within the full-potential linearized augmented planewave method,* Computer Physics Communications **175**, 1 (2006).

[6] H. Ibach and H. Lüth, *Solid-State Physics, An Introduction to Principles of Materials Science, Fourth Edition* (Springer, 2009).

[7] R. F. Egerton, *Electron energy-loss spectroscopy in the TEM,* Reports on Progress in Physics **72**, 016502 (2008).

[8] P. Hohenberg and W. Kohn, *Inhomogeneous electron gas,* Phys. Rev. **136**, B864 (1964).

[9] W. Kohn and L. J. Sham, *Self-consistent equations including exchange and correlation effects,* Phys. Rev. **140**, A1133 (1965).

[10] P. Blaha, K. Schwarz, G. K. Madsen, D. Kvasnicka, J. Luitz, *et al.,* *wien2k,* An augmented plane wave+ local orbitals program for calculating crystal properties (2001).

[11] P. Blaha, K. Schwarz, F. Tran, R. Laskowski, G. K. H. Madsen, and L. D. Marks, *WIEN2k: An APW+lo program for calculating the properties of solids,* The Journal of Chemical Physics **152**, 074101 (2020), https://doi.org/10.1063/1.5143061 .

[12] H. Jiang, R. I. Gómez-Abal, X.-Z. Li, C. Meisenbichler, C. Ambrosch-Draxl, and M. Scheffler, *Fhi-gap: A gw code based on the all-electron augmented plane wave method,* Computer Physics Communications **184**, 348 (2013).

[13] H. Jiang and P. Blaha, *GW with linearized augmented plane waves extended by high-energy local orbitals,* Phys. Rev. B **93**, 115203 (2016).

[14] V. Keast, *An introduction to the calculation of valence EELS: Quantum mechanical methods for bulk solids,* Micron **44**, 93 (2013).

[15] C. Hébert, *Practical aspects of running the WIEN2k code for electron spectroscopy,* Micron **38**, 12 (2007).

[16] L. Hedin, *New Method for Calculating the One-Particle Green's Function with Application to the Electron-Gas Problem,* Phys. Rev. **139**, A796 (1965).

[17] R. H. Ritchie and A. Howie, *Inelastic scattering probabilities in scanning transmission electron microscopy,* Philosophical Magazine A **58**, 753 (1988), https://doi.org/10.1080/01418618808209951 .

[18] A. Polman, M. Kociak, and F. J. García de Abajo, *Electron-beam spectroscopy for nanophotonics,* Nature Materials **18**, 1158 (2019).

[19] D. N. Basov, M. M. Fogler, and F. J. García de Abajo, *Polaritons in van der Waals materials,* Science **354** (2016), 10.1126/science.aag1992, https://science.sciencemag.org/content/354/6309/aag1992.full.pdf .

[20] J. Thijssen, *Computational Physics, Second Edition* (Cambridge University Press, 2007).

[21] D. S. Scholl and J. A. Steckel, *Density Functional Theory, A Practical Introduction* (Wiley, 2009).

[22] K. Berland, V. R. Cooper, K. Lee, E. Schröder, T. Thonhauser, P. Hyldgaard, and B. I. Lundqvist, *van der Waals forces in density functional theory: a review of the vdW-DF method,* Reports on Progress in Physics **78**, 066501 (2015).

[23] M. Dion, H. Rydberg, E. Schröder, D. C. Langreth, and B. I. Lundqvist, *Van der waals density functional for general geometries,* Phys. Rev. Lett. **92**, 246401 (2004).

[24] D. C. Langreth, B. I. Lundqvist, S. D. Chakarova-Käck, V. R. Cooper, M. Dion, P. Hyldgaard, A. Kelkkanen, J. Kleis, L. Kong, S. Li, P. G. Moses, E. Murray, A. Puzder, H. Rydberg, E. Schöder, and T. Thonhauser, *A density functional for sparse matter,* Journal of Physics: Condensed Matter **21**, 084203 (2009).

[25] F. Tran, L. Kalantari, B. Traoré, X. Rocquefelte, and P. Blaha, *Nonlocal van der Waals functionals for solids: Choosing an appropriate one,* Phys. Rev. Materials **3**, 063602 (2019).

[26] F. Tran, J. Stelzl, D. Koller, T. Ruh, and P. Blaha, *Simple way to apply nonlocal van der Waals functionals within all-electron methods,* Phys. Rev. B **96**, 054103 (2017).

[27] Riley, Kevin E. and Pitoňák, Michal and Jurečka, Petr and Hobza, Pavel, *Stabilization and Structure Calculations for Noncovalent Interactions in Extended Molecular Systems Based on Wave Function and Density Functional Theories,* Chemical Reviews **110**, 5023 (2010), pMID: 20486691, https://doi.org/10.1021/cr1000173 .

[28] D. Koller, F. Tran, and P. Blaha, *Improving the modified Becke-Johnson exchange potential,* Phys. Rev. B **85**, 155109 (2012).

[29] F. Tran, J. Doumont, L. Kalantari, A. W. Huran, M. A. L. Marques, and P. Blaha, *Semilocal exchange-correlation potentials for solid-state calculations: Current status and future directions,* Journal of Applied Physics **126**, 110902 (2019), https://doi.org/10.1063/1.5118863 .

[30] L. Reining, *The GW approximation: content, successes and limitations,* WIREs Computational Molecular Science **8**, e1344 (2018), https://onlinelibrary.wiley.com/doi/pdf/10.1002/wcms.1344 .

[31] F. Aryasetiawan and O. Gunnarsson, *"The GW method",* Reports on Progress in Physics **61**, 237 (1998).

2

[32] D. Golze, M. Dvorak, and P. Rinke, *The GW Compendium: A Practical Guide to Theoretical Photoemission Spectroscopy,* Frontiers in Chemistry **7**, 377 (2019).

[33] X. Leng, F. Jin, M. Wei, and Y. Ma, *GW method and Bethe-Salpeter equation for calculating electronic excitations,* WIREs Computational Molecular Science **6**, 532 (2016), https://www.onlinelibrary.wiley.com/doi/pdf/10.1002/wcms.1265 .

[34] X. Blase, I. Duchemin, D. Jacquemin, and P.-F. Loos, *The Bethe-Salpeter Equation Formalism: From Physics to Chemistry,* The Journal of Physical Chemistry Letters **11**, 7371 (2020), pMID: 32787315, https://doi.org/10.1021/acs.jpclett.0c01875 .

[35] W. E. Pickett, H. Krakauer, and P. B. Allen, *Smooth Fourier interpolation of periodic functions,* Phys. Rev. B **38**, 2721 (1988).

3

STRAIN-DEPENDENT EDGE STRUCTURES IN MOS$_2$ LAYERS

Edge structures are low-dimensional defects unavoidable in layered materials of the transition metal dichalcogenides (TMD) family. Among the various types of such structures, the armchair (AC) and zigzag (ZZ) edge types are the most common. It has been predicted that the presence of intrinsic strain localized along these edge structures can have direct implications for the customization of their electronic properties. However, pinning down the relation between local structure and electronic properties at these edges is challenging. Here we quantify the local strain field that arises at the edges of MoS$_2$ flakes by combining aberration-corrected transmission electron microscopy (TEM) with the geometrical phase analysis (GPA) method. We also provide further insight on the possible effects of such edge strain on the resulting electronic behavior by means of electron energy loss spectroscopy (EELS) measurements. Our results reveal that the two-dominant edge structures, ZZ and AC, induce the formation of different amounts of localized strain fields. We also show that by varying the free edge curvature from concave to convex, compressive strain turns into tensile strain. These results pave the way toward the customization of edge structures in MoS$_2$, which in turn can be used to engineer the properties of layered materials and thus contribute to the optimization of the next generation of atomic-scale electronic devices built upon them.

3.1. INTRODUCTION

Layered materials of the transition-metal dichalcogenide (TMD) family have experienced an impressive boost in recent years motivated by their striking physical functionalities. In particular, MoS$_2$ has become a very promising material exhibiting a wide range of possibilities in terms of applications from catalysis [1, 2] to electronic [3–5] and optical [6, 7] devices. For instance, when MoS$_2$ is thinned down to a single monolayer (ML), its indirect band gap switches to a direct bandgap [8, 9] of around 1.88 eV.

Recently, significant attention has been devoted to a specific type of low-dimensional defects, unavoidable in TMDs, known as the edge structures, which are also present in other important layered materials such as graphene [10–13]. These defects arise due to the lack of inversion symmetry in TMDs, which leads in turn to the formation of different edge configurations. Among the various types of possible edge terminations, the specific structures that exhibit a higher degree of symmetry are the so-called armchair (AC) and zigzag (ZZ) structures.

Remarkably, rather than representing a bottleneck for the customization of TMD-based devices, these edge structures allow the tailoring of their associated electronic properties [14, 15] as well as their chemical reactivity [16]. For instance, carrier transport in graphene has been demonstrated to depend drastically on its specific edge structures [17–19]. Another example is provided by triangular MoS$_2$ nanocrystals deposited on Au (111) substrate [20], which exhibit the presence of metallic edge modes in the ZZ terminations. These various features illustrate the potentialities of engineering edge structures in layered materials for application in electronics and optoelectronics [21, 22].

An important property that characterizes these edge structures is their intrinsic strain. In the case of graphene, it has been predicted that edges structures can be found under either compression or tension, depending on the specific type of edge structures [12, 13]. However, most of these studies are limited to density functional theory (DFT) calculations. Therefore, there is an urgency to carry out an experimental program to validate these theoretical expectations. Moreover, although strain is a well-understood mechanism from the theoretical point of view, the experimental quantification of its effects in edge structures in MoS$_2$ has never been performed so far [23], and thus its impact remains largely unexplored. Bridging this gap is therefore one of the main motivations of this work.

3.2. STRUCTURAL ANALYSIS

We combine aberration-corrected scanning transmission electron microscopy (AC-STEM) with the geometrical phase analysis (GPA) method to quantify the local strain field relaxation map in MoS$_2$ layers. First of all, the crystalline nature of the MoS$_2$ flakes is determined by means of AC HAADF-STEM. For these studies, MoS$_2$ flakes are mechanically exfoliated and subsequently transferred to a TEM grid. Figure 3.1a displays a AC-STEM image of a representative MoS$_2$ flake, obtained by operating the microscope at 200 kV. The characteristic hexagonal honeycomb atomic arrangement of [0001]-oriented MoS$_2$ flake is clearly resolved.
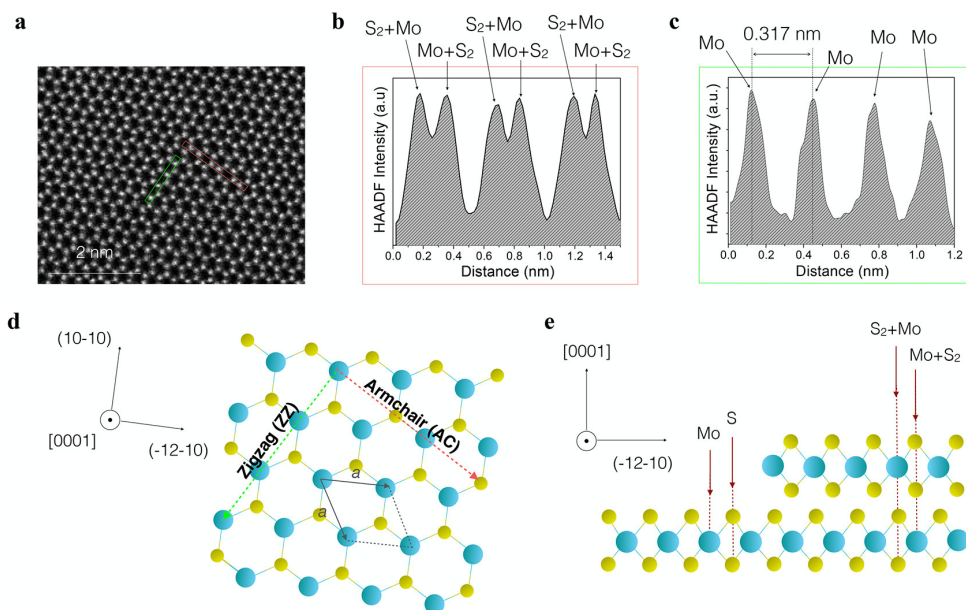
Figure 3.1: (a) Atomic-resolution STEM image of [0001]-oriented MoS$_2$ flake. (b, c) HAADF intensity profile taken along the AC and ZZ directions red and green rectangles in panel a, respectively. (d, e) Schematic atomic model of in-plane and out-of-plane 2H MoS$_2$, respectively. In panel d, the AC and ZZ directions have been indicated by red and green dashed arrows, respectively.

Together with the corresponding HAADF intensity profile (Figure 3.1b), which is directly related to the averaged atomic number and the thickness of the sample [24], this analysis confirms the hexagonal 2H crystalline phase of MoS$_2$. Note that here the HAADF intensity profile has been taken along the armchair (AC) direction (red rectangle in Figure 3.1a). For [0001]-oriented MoS$_2$ (Figure 3.1d), at the S-site, the electron beam interacts with a S atom first, while at the Mo site, the Mo atom is contacted first (Figure 3.1e). The fact that there are no variations in the relative intensities between the Mo-sites and S-sites indicates that in this specific region we have an even number of MoS$_2$ layers.

The lattice parameter of MoS$_2$ can be then determined by measuring the Mo−Mo bond length, which can be measured from the HAADF intensity profile (Figure 3.1c) taken along the zigzag (ZZ) edge bond direction (green rectangle in Figure 3.1a). The length of the Mo−Mo edge turns out to be 0.317 nm, which corresponds to the equilibrium lattice parameter of MoS$_2$ with hexagonal crystal structure [25]. This result indicates that the MoS$_2$ lattice is not perturbed in this region. Moreover, the absence of holes [26] and folds [27] formation during the measurements, which could compromise our results, ensures that the quality of the MoS$_2$ flakes is maintained when operating the microscope at 200 kV, as has been previously reported [28, 29].

3.3. STRAIN-DEPENDENT EDGE STRUCTURE IN A MoS$_2$ FLAKE

Figure 3.2a displays a AC HAADF-STEM image taken in the region around the transition from three to two MLs in the [0001]-oriented MoS$_2$ flake. The difference in contrast separates the 3 MLs (brighter) and 2 MLs (darker) regions. To map the strain field around the edges of MoS$_2$, the GPA method has been applied [30]. The basic idea of the GPA technique is to measure local phase distortions, which can be directly linked to any distortion in the lattice fringes in the atomic-resolution HAADF image with respect to a reference. The corresponding strain fields can be then calculated by tacking the derivative of the displacement field [31, 32].

The phase image (Figure 3.2d) was calculated for the set of (01−10) lattice fringes (Figure 3.2c), evaluated from the fast Fourier transform (FFT); see Figure 3.2b. The phase image exhibits a discontinuity from 0 to $\frac{\pi}{5}$ around the transition from 3MLs to 2MLs. Taking the x−axis parallel to $[-12-10]$, the corresponding strain field is shown in Figure 3.2e. Crucially, from the strain field map (Figure 3.2e) we observe a region exhibiting tensile strain, whose value ranges between 2% and 4%, localized exactly at the transition between the regions with 2MLs and with 3MLs.
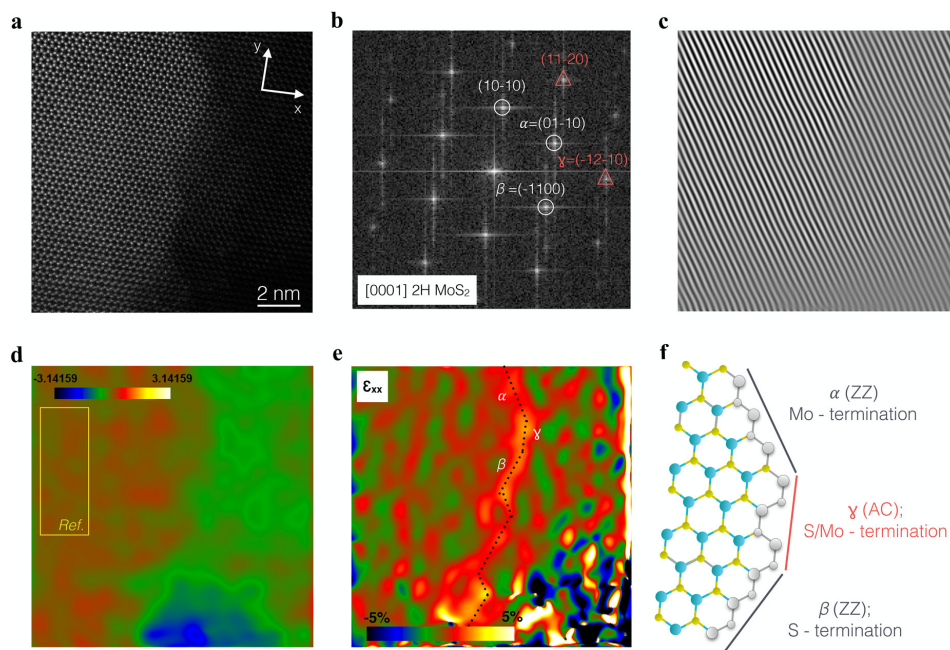
Figure 3.2: (a, b) Atomic-resolution HAADF image taken in the transition region between 3MLs and 2MLs and the corresponding fast Fourier transform (FFT), respectively. (c) (01–10) lattice fringes obtained by filtering. (d) Phase image of (01–10) lattice fringes, where the yellow rectangle indicates the reference region used for the strain field map calculation. The color range indicates variations from $-\pi$ to π. (e) The ϵ_{xx} strain component indicating the presence of strong tensile strain in this transition region. (f) Atomic model representing the structure of the ZZ and AC edge structures in MoS$_2$.

More specifically, such transition region is defined by the intersections of the family of planes {1100} and {1-210}. The atomic terminations of these two families of planes are known as zigzag (ZZ) and armchair (AC) configurations, respectively, and are represented in Figure 3.2f. Note that when two ZZ edges merge, the resulting junction defines the minimal unit of an AC edge. We find that the ZZ edges exhibit tensile strain ranging between (2 ± 0.5) % and (4 ± 1) %, where the later value arises at the junctions between two ZZ edges (that represents a short AC edge). However, the longer AC edge (labeled as γ) appears under a tensile strain of around (2 ± 0.5) %. Note that here we use a Fourier mask that leads to a spatial resolution of 0.5 nm. This choice represents an appropriate balance between smoother strain fields but worse spatial resolution (achieved with a small mask) and better spatial resolution but with a higher level of fluctuation.

The appearance of such localized strain at the ZZ and AC edges could be related to the edge relaxation mechanism itself, induced by the adjustment of the bond length and bond angles of the edge atoms [33]. In this scenario, the MoS$_2$ sheets generated by mechanical exfoliation initially have an excess of energy. Therefore, the free-edges (S-Mo-S) of the MoS$_2$ flakes are originated with stress. Subsequently, the MoS$_2$ sheet relaxes to reduce this excess of energy. Theoretical calculations of the elastic properties of phosphorene nanoribbons [34] reported a similar result, where the energy relaxation modifies the atomic arrangement of AC and ZZ edges, resulting into a tensile stress along the ZZ and AC edges consistent with our findings here. Moreover, we also found that this relaxation mechanism is translated into an out-of-plane distortion [35].

3.4. EELS Characterization of Electronic Properties of MoS$_2$ Flakes

To obtain further insight on the effects of edge strain on the resulting electronic behavior, we have carried out a direct correlation experiment by means of an electron energy loss spectroscopy (EELS) analysis [36]. For these measurements a monochromated electron source operating at 60 kV was used, which achieves an energy resolution of around 30 meV. A crucial advantage of EELS is that it allows achieving high-energy resolution while simultaneously leading to competitive spatial resolution [37].

Figure 7.8a displays a low-magnification HAADF-STEM image taken in the same region where the strain measurements were performed (see Figure 3.2a). Subsequently, point-by-point EELS spectra were recorded at different locations in the boundary region between 2MLs and 3MLs, indicated by the points S1 to S4 in Figure 3a. We focused on the low-loss energy region, ranging between electron energy losses of 0 and 4 eV. The most-distinctive features of the EELS spectra (Figure 7.8b) are the presence of two relatively narrow peaks, located at around 1.89 eV (peak A) and 2.05 eV (peak B), respectively. These two peaks in the MoS$_2$ EELS spectra can be interpreted as arising from the direct exciton transitions, specially due to band splitting effects induced to interlayer interaction and spin-orbit coupling [9, 38, 39]. Our measurements for the position of these EELS peaks are consistent with previously experimental [40] and theoretical studies [41].

We further quantify the properties of these exciton peaks by means of a fitting procedure, in which a double Gaussian is used for the signal combined with a quadratic polynomial
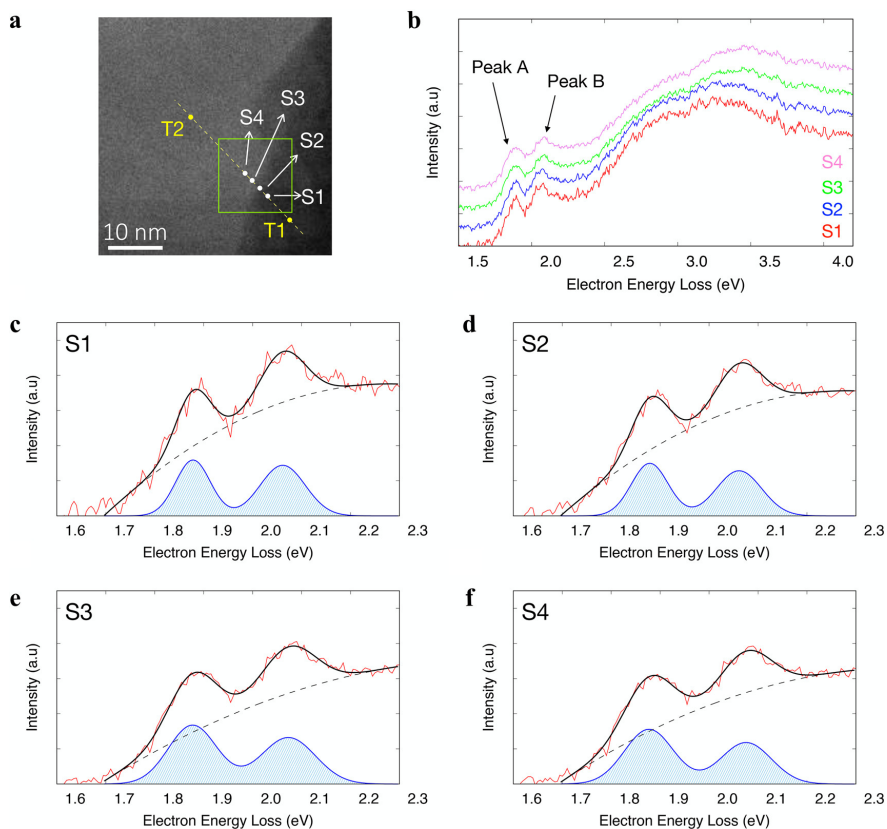
Figure 3.3: (a) Low-magnification HAADF–STEM image of the MoS2 flake in the transition region between 2 and 3 ML. (b) Offset of the EELS spectra corresponding to S1, S2, S3, and S4 in panel a. (c–f) EELS spectra recorded at S1, S2, S3, and S4 with the corresponding fits.

for the background. The comparison between the EELS measurements and the resulting fits is shown in Figures 7.8c-f, where we also show the two Gaussian peaks, denoted by peak A and peak B, with the background subtracted. One factor that is known to affect the peaks' width is the thickness of the MoS$_2$ layers [40]. Moreover, it is conceivable that the strain localized at the interface (see Figure 3.2e) might also induce variations in these widths.

To investigate the interplay between these two effects, we have recorded EELS spectra at two additional locations, labeled by T1 (in 2 MLs region) and T2 (in 3 MLs region) in Figure 7.8a. Because these EELS spectra correspond to regions far from the boundaries, no effects associated with edge strain are expected to arise. By comparing the values of the full-width at half-maximum (FWHM) of peak A (B) value between points T1 and T2, we find that it increases by around 70% (30%). However, when comparing the FWHM values of peak A (B) between the points S1 and S3 (see Figure 3.4) (that is, just before and after crossing the interface where, in addition to the different thicknesses, we must also
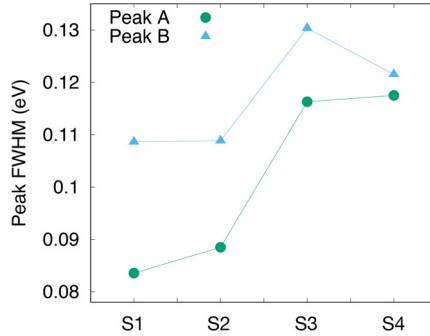
Figure 3.4: Variation of the full-width at half-maximum (FWHM) of peaks A and B along this transition region, where measurements corresponding to the points labeled as S1 to S4 in Figure 7.8a are shown.

account for the possible effects of strain), we find that the increase is now around 30% (15%). Therefore, we observe a nontrivial dependence of the FWHM values of the two exciton peaks at the interface region, which cannot be accounted purely by the change in thickness and, at least partly, should be understood in terms of the interface strain.

This remarkable correlation highlights the deep connection between structural and electronic properties of MoS_2, which can be tuned layer by layer. In this respect, new theoretical calculations would be required to fully disentangle the contribution of the various physical mechanisms that contribute to the exciton peak broadening, especially the interplay between the tensile strain at the edge and the layer thickness variation.

Concerning the peak positions as determined from the fit, we find values of 1.89 and 1.88 eV for peak A and 2.05 and 2.08 eV for peak B in the regions with two and three MLs, respectively. We therefore find that for peak B there is a clear difference in peak position between the two regions. This behavior could be understood as a direct consequence of the specific crystalline structure of MoS_2. Indeed, for an odd number of MoS_2 layers, the crystal belongs to the non-centrosymmetric D_{3h} space group. However, for an even number of layers instead, the crystal belongs to the D_{3d} space group, which is characterized by inversion symmetry.

3.5. STRAIN DEPENDENCE OF FREE-EDGE CURVATURE

Strain-dependent edge structures also arise at the interface between the MoS_2 flake and the vacuum, the so-called free edges. Figure 3.5 displays a AC HAADF-STEM image taken in a region that only exhibits ZZ edge terminations. As can be observed from the filtered lattice fringes image (Figure 3.5b), this free edge alternates concave and convex regions. These opposite-curvature regions are originated during the mechanical exfoliation process.

By applying the geometrical phase analysis method as described above, we can evaluate the local strain field map which allows us to distinguish regions with alternating localized compressive and tensile strain at the ZZ edges. In particular, the concave regions exhibit

3
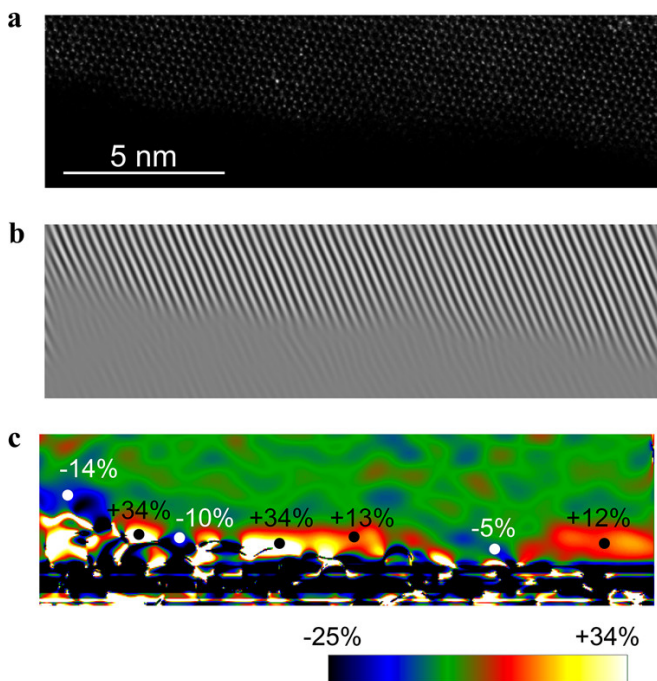
Figure 3.5: (a) AC HAADF-STEM image of a region exhibiting a free edge of MoS$_2$. (b) From the filtered lattice fringes, we can clearly identify concave and convex terminations. (c) The ϵ_{xx} strain component indicating the presence of compressive (tensile) strain in the concave (convex) region.

a compressive strain, while for the convex ones a tensile strain is exhibited. Moreover, as compared to the strain values reported at the interface between 2MLs and 3MLs (see Figure 3.2e), here the levels of strain reached are higher, with values up to around +30% in the convex regions and down to around 14% in the concave regions. These results suggest that the possibility of exploiting the free edge curvature to turn tensile into compressive strain could provide a novel handle to tune the electronic properties of layered materials.

3.6. Conclusion

To summarize, controlling and understanding the formation of localized strain at the edge structures of TMD materials is of great importance toward the customization of their electronic properties. Here, by combining aberration-corrected TEM with the geometrical phase analysis method, we have quantified the edge structures and elastic properties of MoS$_2$ flakes. We find that the relaxation of the ZZ and AC edge structures leads to the appearance of a tensile strain, with magnitude ranging between 2% and 4%. This implies that the tensile strain can lead to the elastic distortion of the edge.

Furthermore, the EELS analysis performed at the same transition region highlights an increase of the exciton A and B peak widths by around 30% and 15%, respectively, that

can at least partly be explained by the presence of such tensile strain at the edges. However, this broadening of the exciton peaks also receives contributions from the change of thickness of the MoS_2 layers. In this respect, new theoretical calculations would be required to fully disentangle the contribution of the various physical mechanisms that contribute to the exciton peak broadening, especially the interplay between the tensile strain at the edge and the layer thickness variation.

Finally, strain measurements performed at free edges between MoS_2 and a vacuum, which exhibit convex and concave regions, demonstrate the direct interplay between interface curvature and the presence of either tensile or compressive strain.

Even if in this work we have restricted ourselves to the analysis of MoS_2 flakes, our approach is fully general, and we plan to extend it to a comprehensive analysis of the strain-dependent edge structures in other layered materials. Our results could therefore pave the way toward the customization of electronic properties of TMD materials by means of strain-dependent edge structure.

REFERENCES

[1] M. A. Lukowski, A. S. Daniel, F. Meng, A. Forticaux, L. Li, and S. Jin, *Enhanced Hydrogen Evolution Catalysis from Chemically Exfoliated Metallic MoS$_2$ Nanosheets,* Journal of the American Chemical Society **135**, 10274 (2013), pMID: 23790049, https://doi.org/10.1021/ja404523s .

[2] D. Voiry, H. Yamaguchi, J. Li, R. Silva, D. C. B. Alves, T. Fujita, M. Chen, T. Asefa, V. B. Shenoy, G. Eda, and M. Chhowalla, *Enhanced catalytic activity in strained chemically exfoliated WS$_2$ nanosheets for hydrogen evolution,* Nature Materials **12**, 850 (2013).

[3] J. V. Lauritsen, J. Kibsgaard, S. Helveg, H. Topsøe, B. S. Clausen, E. Lægsgaard, and F. Besenbacher, *Size-dependent structure of MoS$_2$ nanocrystals,* Nature Nanotechnology **2**, 53 (2007).

[4] B. Radisavljevic, A. Radenovic, J. Brivio, V. Giacometti, and A. Kis, *Single-layer MoS$_2$ transistors,* Nature Nanotechnology **6**, 147 (2011).

[5] M.-Y. Li, Y. Shi, C.-C. Cheng, L.-S. Lu, Y.-C. Lin, H.-L. Tang, M.-L. Tsai, C.-W. Chu, K.-H. Wei, J.-H. He, W.-H. Chang, K. Suenaga, and L.-J. Li, *Epitaxial growth of a monolayer WSe$_2$-MoS$_2$ lateral p-n junction with an atomically sharp interface,* Science **349**, 524 (2015).

[6] Z. Yin, H. Li, H. Li, L. Jiang, Y. Shi, Y. Sun, G. Lu, Q. Zhang, X. Chen, and H. Zhang, *Single-Layer MoS$_2$ Phototransistors,* ACS Nano **6**, 74 (2012), pMID: 22165908, https://doi.org/10.1021/nn2024557 .

[7] A. F. Rigosi, H. M. Hill, Y. Li, A. Chernikov, and T. F. Heinz, *Probing Interlayer Interactions in Transition Metal Dichalcogenide Heterostructures by Optical Spectroscopy: MoS$_2$/WS$_2$ and MoSe$_2$/WSe$_2$,* Nano Letters **15**, 5033 (2015), pMID: 26186085, https://doi.org/10.1021/acs.nanolett.5b01055 .

[8] Y. Chen, J. Xi, D. O. Dumcenco, Z. Liu, K. Suenaga, D. Wang, Z. Shuai, Y.-S. Huang, and L. Xie, *Tunable Band Gap Photoluminescence from Atomically Thin Transition-Metal Dichalcogenide Alloys,* ACS Nano **7**, 4610 (2013), pMID: 23600688, https://doi.org/10.1021/nn401420h .

[9] K. F. Mak, C. Lee, J. Hone, J. Shan, and T. F. Heinz, *Atomically Thin MoS$_2$: A New Direct-Gap Semiconductor,* Phys. Rev. Lett. **105**, 136805 (2010).

[10] C. D. Reddy, A. Ramasubramaniam, V. B. Shenoy, and Y.-W. Zhang, *Edge elastic properties of defect-free single-layer graphene sheets,* Applied Physics Letters **94**, 101904 (2009), https://doi.org/10.1063/1.3094878 .

[11] C. K. Gan and D. J. Srolovitz, *First-principles study of graphene edge properties and flake shapes,* Phys. Rev. B **81**, 125445 (2010).

[12] V. B. Shenoy, C. D. Reddy, A. Ramasubramaniam, and Y. W. Zhang, *Edge-Stress-Induced Warping of Graphene Sheets and Nanoribbons,* Phys. Rev. Lett. **101**, 245501 (2008).

[13] S. Jun, *Density-functional study of edge stress in graphene,* Phys. Rev. B **78**, 073405 (2008).

[14] X. Peng, Q. Wei, and A. Copple, *Strain-engineered direct-indirect band gap transition and its mechanism in two-dimensional phosphorene,* Phys. Rev. B **90**, 085402 (2014).

[15] H. J. Conley, B. Wang, J. I. Ziegler, R. F. Haglund, S. T. Pantelides, and K. I. Bolotin, *Bandgap Engineering of Strained Monolayer and Bilayer MoS$_2$,* Nano Letters **13**, 3626 (2013), pMID: 23819588, https://doi.org/10.1021/nl4014748 .

[16] J. Kibsgaard, Z. Chen, B. N. Reinecke, and T. F. Jaramillo, *Engineering the surface structure of MoS$_2$ to preferentially expose active edge sites for electrocatalysis,* Nature Materials **11**, 963 (2012).

[17] N. M. R. Peres, J. N. B. Rodrigues, T. Stauber, and J. M. B. L. dos Santos, *Dirac electrons in graphene-based quantum wires and quantum dots,* Journal of Physics: Condensed Matter **21**, 344202 (2009).

[18] N. M. R. Peres, *Colloquium: The transport properties of graphene: An introduction,* Rev. Mod. Phys. **82**, 2673 (2010).

[19] A. C. Neto, F. Guinea, and N. M. Peres, *Drawing conclusions from graphene,* Physics World **19**, 33 (2006).

[20] S. Helveg, J. V. Lauritsen, E. Lægsgaard, I. Stensgaard, J. K. Nørskov, B. S. Clausen, H. Topsøe, and F. Besenbacher, *Atomic-Scale Structure of Single-Layer MoS$_2$ Nanoclusters,* Phys. Rev. Lett. **84**, 951 (2000).

[21] A. M. van der Zande, P. Y. Huang, D. A. Chenet, T. C. Berkelbach, Y. You, G.-H. Lee, T. F. Heinz, D. R. Reichman, D. A. Muller, and J. C. Hone, *Grains and grain boundaries in highly crystalline monolayer molybdenum disulphide,* Nature Materials **12**, 554 (2013).

[22] H. R. Gutiérrez, N. Perea-López, A. L. Elías, A. Berkdemir, B. Wang, R. Lv, F. López-Urías, V. H. Crespi, H. Terrones, and M. Terrones, *Extraordinary Room-Temperature Photoluminescence in Triangular WS$_2$ Monolayers,* Nano Letters **13**, 3447 (2013), pMID: 23194096, https://doi.org/10.1021/nl3026357 .

[23] Q. Wu, X. Li, A. A. Volinsky, and Y. Su, *Edge eigen-stress and eigen-displacement of armchair molybdenum disulfide nanoribbons,* Physics Letters A **381**, 1568 (2017).

[24] J. M. LeBeau and S. Stemmer, *Experimental quantification of annular dark-field images in scanning transmission electron microscopy,* Ultramicroscopy **108**, 1653 (2008).

[25] J. Kang, S. Tongay, J. Zhou, J. Li, and J. Wu, *Band offsets and heterostructures of two-dimensional semiconductors,* Applied Physics Letters **102**, 012111 (2013), https://doi.org/10.1063/1.4774090 .

[26] M. Sammalkorpi, A. Krasheninnikov, A. Kuronen, K. Nordlund, and K. Kaski, *Mechanical properties of carbon nanotubes with vacancies and related defects,* Phys. Rev. B **70**, 245416 (2004).

[27] A. Castellanos-Gomez, H. S. J. van der Zant, and G. A. Steele, *Folded MoS$_2$ layers with reduced interlayer coupling,* Nano Research **7**, 572 (2014).

[28] J. Brivio, D. T. L. Alexander, and A. Kis, *Ripples and Layers in Ultrathin MoS$_2$ Membranes,* Nano Letters **11**, 5148 (2011), pMID: 22010987, https://doi.org/10.1021/nl2022288 .

[29] Y. Shi, J.-K. Huang, L. Jin, Y.-T. Hsu, S. F. Yu, L.-J. Li, and H. Y. Yang, *Selective Decoration of Au Nanoparticles on Monolayer MoS$_2$ Single Crystals,* Scientific Reports **3**, 1839 (2013).

[30] M. Hÿtch, E. Snoeck, and R. Kilaas, *Quantitative measurement of displacement and strain fields from HREM micrographs,* Ultramicroscopy **74**, 131 (1998).

[31] S. Conesa-Boj, F. Boioli, E. Russo-Averchi, S. Dunand, M. Heiss, D. Rüffer, N. Wyrsch, C. Ballif, L. Miglio, and A. F. i. Morral, *Plastic and Elastic Strain Fields in GaAs/Si Core-Shell Nanowires,* Nano Letters **14**, 1859 (2014), pMID: 24564880, https://doi.org/10.1021/nl4046312 .

[32] J. H. Warner, N. P. Young, A. I. Kirkland, and G. A. D. Briggs, *Resolving strain in carbon nanotubes at the atomic level,* Nature Materials **10**, 958 (2011).

[33] Y. Huang, C. Ling, H. Liu, and S. Wang, *Edge-, width- and strain-dependent semiconductor-metal transition in SnSe nanoribbons,* RSC Adv. **4**, 6933 (2014).

3

[34] V. Sorkin and Y. W. Zhang, *The structure and elastic properties of phosphorene edges,* Nanotechnology **26**, 235707 (2015).

[35] V. V. Ivanovskaya, P. Wagner, A. Zobelli, I. Suarez-Martinez, A. Yaya, and C. P. Ewels, *Graphene edge structures: Folding, scrolling, tubing, rippling and twisting,* in *GraphITA 2011,* edited by L. Ottaviano and V. Morandi (Springer Berlin Heidelberg, Berlin, Heidelberg, 2012) pp. 75–85.

[36] R. Arenal, O. Stéphan, M. Kociak, D. Taverna, A. Loiseau, and C. Colliex, *Electron Energy Loss Spectroscopy Measurement of the Optical Gaps on Individual Boron Nitride Single-Walled and Multiwalled Nanotubes,* Phys. Rev. Lett. **95**, 127601 (2005).

[37] F. J. García de Abajo, *Optical excitations in electron microscopy,* Rev. Mod. Phys. **82**, 209 (2010).

[38] A. Splendiani, L. Sun, Y. Zhang, T. Li, J. Kim, C.-Y. Chim, G. Galli, and F. Wang, *Emerging Photoluminescence in Monolayer MoS$_2$,* Nano Letters **10**, 1271 (2010), pMID: 20229981, https://doi.org/10.1021/nl903868w .

[39] X. Fan, D. J. Singh, and W. Zheng, *Valence Band Splitting on Multilayer MoS$_2$: Mixing of Spin-Orbit Coupling and Interlayer Coupling,* The Journal of Physical Chemistry Letters **7**, 2175 (2016), pMID: 27225320, https://doi.org/10.1021/acs.jpclett.6b00693 .

[40] H. C. Nerl, K. T. Winther, F. S. Hage, K. S. Thygesen, L. Houben, C. Backes, J. N. Coleman, Q. M. Ramasse, and V. Nicolosi, *Probing the local nature of excitons and plasmons in few-layer MoS$_2$,* npj 2D Materials and Applications **1**, 2 (2017).

[41] H.-P. Komsa and A. V. Krasheninnikov, *Effects of confinement and environment on the electronic structure and exciton binding energy of MoS$_2$ from first principles,* Phys. Rev. B **86**, 241201 (2012).

4

METALLIC EDGE-STATES IN ZIG-ZAG VERTICALLY-ORIENTED MoS$_2$ NANOWALLS

In Chapter 3 we have seen how the specific edge configuration of an exfoliated flake of MoS$_2$ can affect the strain and electronic structure of the flake. In order to unambiguously probe the corresponding physical properties, accurate control of the structural design of nanostructures based on layered materials is necessary. The remarkable properties of layered materials such as MoS$_2$ strongly depend on their dimensionality. Beyond manipulating their dimensions, it has been predicted that the electronic properties of MoS$_2$ can also be tailored by carefully selecting the type of edge sites exposed. However, achieving full control over the type of exposed edge sites while simultaneously modifying the dimensionality of the nanostructures is highly challenging. Here we adopt a top-down approach based on focus ion beam in order to selectively pattern the exposed edge sites. This strategy allows us to select either the armchair (AC) or the zig-zag (ZZ) edges in the MoS$_2$ nanostructures, as confirmed by high-resolution transmission electron microscopy measurements. The edge-type dependence of the local electronic properties in these MoS$_2$ nanostructures is studied by means of electron energy-loss spectroscopy measurements. This way, we demonstrate that the ZZ-MoS$_2$ nanostructures exhibit clear fingerprints of their predicted metallic character. Our results represent a stepping stone towards novel approaches for the design and fabrication of more complex nanostructures based on MoS$_2$ and related layered materials for applications in fields such as electronics, optoelectronics, photovoltaics, and photocatalysts.

4.1. INTRODUCTION

T HE ability of crafting new materials in a way that makes possible controlling and enhancing their properties is one of the main requirements of the ongoing nanotechnology revolution [1, 2]. In this context, a family of materials that has attracted intense attention recently are two-dimensional (2D) layered materials of the Transition Metal Dichalcogenide (TMD) family such as MoS$_2$. These materials have been extensively studied due to their promising electrical and optical properties [3–6].

A defining feature of TMDs is that they exhibit a lack of inversion symmetry, which leads to the appearance of a variety of different edge structures. The most common of these, consisting of dangling bounds, are the armchair (AC) and the zig-zag (ZZ) edge structures. Of particular relevance in this context, the electronic properties of MoS$_2$ have been predicted to be affected by the presence of the different edge structures in rather different ways. For instance, the AC edges have been predicted to be semiconducting, while the ZZ edges should exhibit instead metallic behavior [7–10]. Moreover, *ab-initio* theoretical calculations predict that these metallic states at the edges of MoS$_2$ could lead to the formation of plasmons [11]. Beyond this tuning of electronic properties, other attractive applications of these active edge sites arise in photocatalysis, such as their use in hydrogen evolution reactions (HER) [12–15].

With these motivations, it is clear that the design and fabrication of MoS$_2$ nanostructures with morphologies that maximize the number of exposed active edge sites is a key aspect for further improvements in terms of applications. In this respect, significant efforts have been pursued to realize the systematic bottom-up growth of vertically-oriented standing MoS$_2$ layers. This configuration leads to the edge sites facing upwards, therefore maximizing the number of exposed edge sites as compared with the more common horizontal configuration, where its basal plane lies parallel to the substrate [16–23].

However, this bottom-up approach is hampered by a lack of reproducibility due to the complexities of the growth mechanism. Another limitation within the bottom-up approach is that the specific type of edges exposed cannot be selectively grown. Ideally, one would like to combine the best of both worlds. On the one hand, it is important to be able to controllably grow MoS$_2$ nanostructures that exhibit the largest possible surface area of edge structures, as it is achieved by the bottom-up strategy summarized above. On the other hand, one would also like to be able to select the specific type of edge sites exposed, in particular, by selecting whether these correspond to AC or to ZZ edges. Therefore, the main goal of this work is to bridge these two requirements by realizing a novel approach to the growth of vertically-oriented standing MoS$_2$ layers with full control on the nature of the exposed edge sites.

To achieve this goal, here we adapt a well-established top-down approach based on focus ion beam (FIB) in a way that allows us to selectively pattern both types of edges (AC and ZZ) within out-of-plane (vertical) MoS$_2$ nanostructures. In the context of patterning layered materials, the usefulness of FIB has been repeatedly demonstrated [24–26]. By means of this technique, we are able to selectively maximize the density of exposed edge sites while controlling their type. Subsequently, by combining high-resolution transmission electron microscopy (TEM) with electron energy-loss spectroscopy (EELS) mea-

surements, we are able to confirm not only the crystallographic nature of both the AC and ZZ MoS_2 surfaces, but also we can demonstrate that, despite the roughness and imperfections induced during the fabrication procedure, the ZZ MoS_2 nanostructures clearly exhibit a metallic character, in agreement with the theoretical predictions from *ab-initio* calculations [11]. The results of this study should open new opportunities for the nanoengineering of the edge types in MoS_2 nanostructures as well as in related layered materials, paving the way towards novel exciting opportunities both for fundamental physics and technological applications in fields such as electronics, optoelectronics, photovoltaics, and photocatalysts.

4.2. Focus ion beam patterning for the fabrication of edge-controlled MoS_2 nanowalls

MoS_2 bulk crystal obtained from Alfa Aesar (with a 99.999% purity) was mechanically exfoliated with Poly-Di-Methyl-Siloxaan (PDMS) and then transferred to a SiO_2/Si substrate. The MoS_2 nanostructures were milled using a FEI Helios G4 CX focus ion beam. The ion milling procedure was carried out using a very low energy electron beam of 15 kV, and an ion beam of 2 pA. From crystal structure considerations, the possible angles between adjacent flat edges within MoS_2 flakes should be multiples of 30°. Specifically, the expected angles between adjacent AC and ZZ edge structures in a MoS_2 flake such as that of Figure 4.1a should be 30°, 90°, and 120°, as illustrated in Figure 4.1b. Taking into account this information, we designed the orientation of the different areas of the MoS_2 flake that subsequently will be patterned. In this way, we can ensure the full control over the resulting specific edge crystallographic orientation. Figure 4.1c,d display a scanning electron microscopy (SEM) image of the MoS_2 flake that has been used for the fabrication of the nanostructures, taken before and after the milling respectively. Before the milling is performed, a protective metallic layer of tungsten (W) with a thickness of 500nm was deposited on top of the selected areas of the MoS_2 flake. Subsequently, we performed a series of milling and cleaning processes in order to construct the vertically-aligned MoS_2 nanostructures. Figure 4.1d displays three ordered vertically-oriented patterned arrays of MoS_2 nanostructures, which in the following are denoted as nanowalls (NWs). Two of these sets of nanowalls are oriented perpendicularly with respect to each other, guaranteeing that this way one of two arrays will correspond to AC (ZZ) NWs while the other array will correspond instead to the complementary ZZ (AC) ones. These NWs are found to exhibit a uniform thickness being (89±5) nm (central array in Figure 4.1d) and (68±5) nm (rightmost array in Figure 4.1d). Note that the left-most array was fabricated without the protective metal layer.

4.3. Structural Characterisation of MoS_2 nanowalls

4.3.1. Chemical Mapping

To further examine the crystallographic nature of the resulting vertical MoS_2 nanostructures, transmission electron microscopy (TEM) studies were carried out. For these studies, we lifted out two of the MoS_2 NWs from the two different patterned NWs arrays using a micromanipulator. Subsequently, the nanostructure was mounted onto a TEM half-
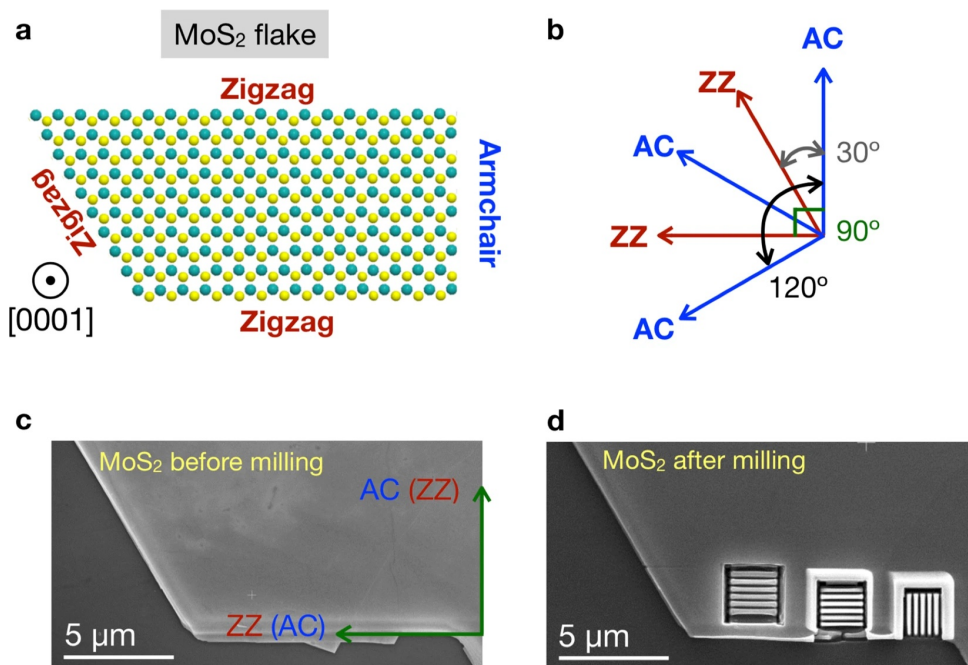
Figure 4.1: (a) Atomic model of a MoS$_2$ flake viewed along the [0001] direction, where we indicate the corresponding zig-zag (ZZ) and armchair (AC) edges. (b) From geometric considerations, we can determine the possible values that the angles between adjacent AC and ZZ edges should take; (c) and (d) SEM micrographs of the MoS$_2$ flake used for patterning the nanowalls, taken before and after the milling respectively. In (d), three different set of arrays can be observed. The left-most array was fabricated without the protective metal layer, while the other arrays used instead this protective metal layer.

grid. This whole procedure takes place within the FIB chamber.

Figure 4.2a displays a high-angle annular dark-field scanning transmission electron microscopy (HAADF-STEM) image of a selected region of the ZZ MoS$_2$ nanowall, bracketed between the Si substrate and the metallic protective layer. Figure 4.2b shows the corresponding chemical composition of this nanowall obtained by means of Energy Dispersive X-ray Spectroscopy (EDS) measurements. From the EDS map, the different chemical components of the NWs can be clearly distinguished: the MoS$_2$ segment, embedded within the protective metal layer tungsten (W), and the silicon (Si) substrate.

4.3.2. FINGERPRINTING THE EDGE-TYPE NATURE OF MoS$_2$ NANOWALLS
From the crystalline structure studies carried out by means of high-resolution TEM measurements (Figure 4.3), we are able to confirm the specific edge site configuration for the two NW arrays. Figures 4.3a and 4.3b display the results of the TEM measurements on the AC and ZZ MoS$_2$ surfaces respectively. By comparing the two crystallographic orientations, AC and ZZ, we can observe the differences between the atomic arrangement of each surface, which are consequently characterized by different fast Fourier transforms
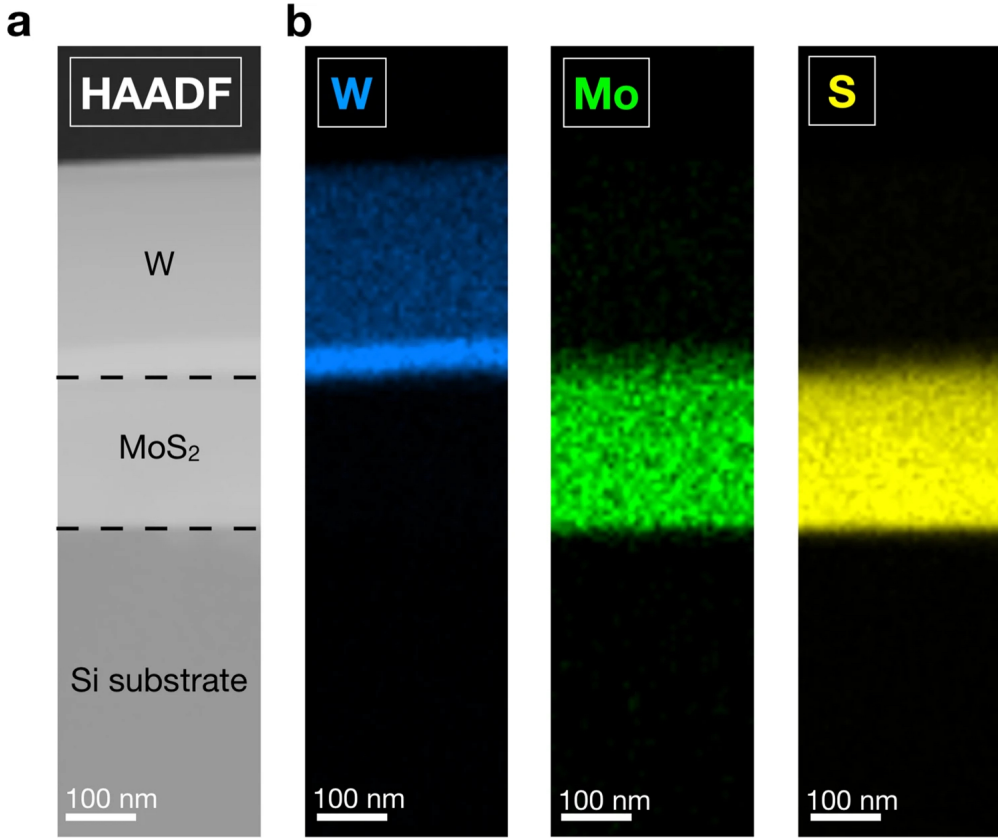
Figure 4.2: (a) HAADF-STEM image of an area of the ZZ MoS_2 NW, which is bracketed between the Si substrate and the metallic protective layer; (b) The corresponding EDX compositional maps (Mo in green, S in yellow, W in blue).

(FFTs) (shown in the insets of Figure 4.3a,b). From these results, it is clearly noticeable the excellent agreement between the experimental FFTs obtained from the TEM measurements and the corresponding ones calculated theoretically in terms of the expected atomic configuration (shown in Figure 4.3c,d). These results provide direct confirmation that these vertically-oriented MoS_2 nanowalls are in fact exposing ZZ and AC edge terminations, therefore validating our fabrication strategy.

4.4. Edge-dependent electronic behaviour

In order to pin down the local electronic properties of the AC and ZZ MoS_2 NWs, electron energy-loss spectroscopy (EELS) measurements have been carried out in a scanning transmission electron microscope (STEM). In Figure 4.4 we show the energy-loss spectra corresponding to both the AC and ZZ surfaces taken at different points along the length of the nanowall, spanning multiple layers of MoS_2. As it can be observed in the two sets
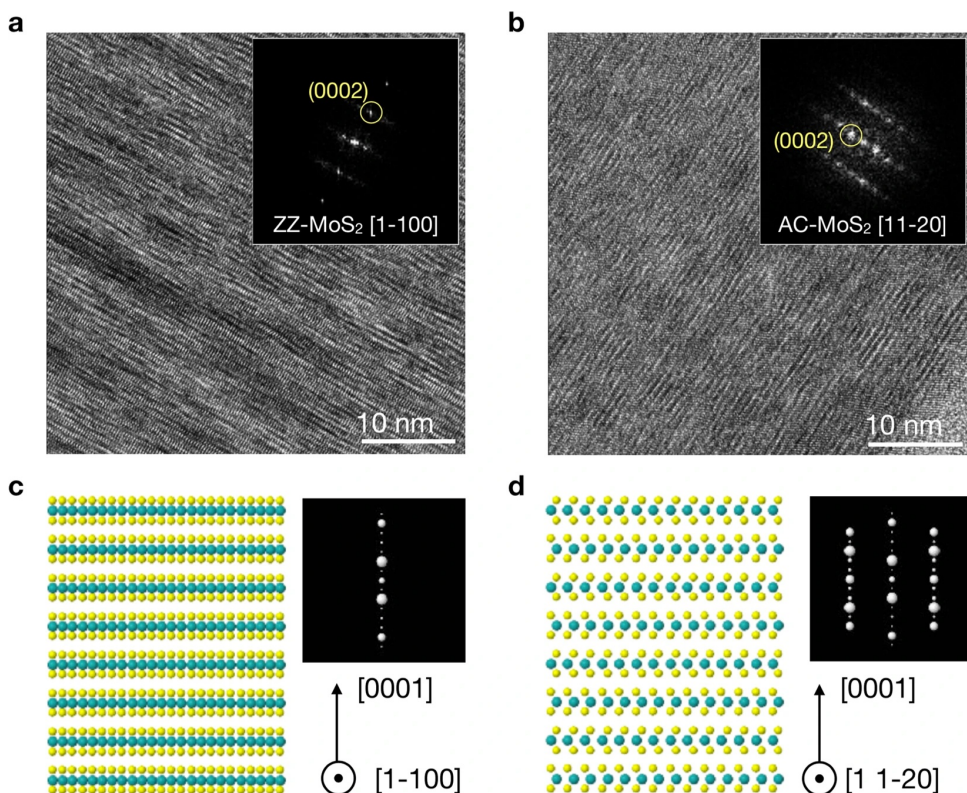
Figure 4.3: (a,b) HRTEM micrographs of representative ZZ and AC MoS$_2$ nanowalls, respectively. The insets indicate the corresponding fast Fourier transform (FFT). (c) and (b) The atomic modelling associated to the AC and ZZ orientations of the NWs, together with the theoretical calculation of the expected FFTs.

of EELS spectra, the MoS$_2$ bulk plasmon signal appears at 23.4 eV in both samples with similar intensities and general shape, in agreement with previous analyses [27, 28].

Nevertheless, the MoS$_2$ surface plasmon peak, present at 15.2 eV, turns out to appear only on a restricted subset of the spectra of the ZZ-nanowalls. Considering that the fabricated AC-nanowalls are thinner than the ZZ-terminated ones, the presence of the surface MoS$_2$ plasmon on the ZZ-nanowalls cannot be attributed to a lower thickness of the sample. Therefore, the origin of this peak should be caused by another phenomena. In that respect, it is important to notice that the MoS$_2$ surface plasmon peak appears and disappears in a periodic manner, depending on the specific position along the nanowall where the EELS spectrum is collected.

It is found that the positions which correspond to local maxima of the intensity associated to this surface plasmon peak are separated by around 12 nm between each other. This behavior can be attributed to the presence of metallic surface plasmon polaritons (SPP), which are planar waves appearing at the interfaces between a metal and a dielec-
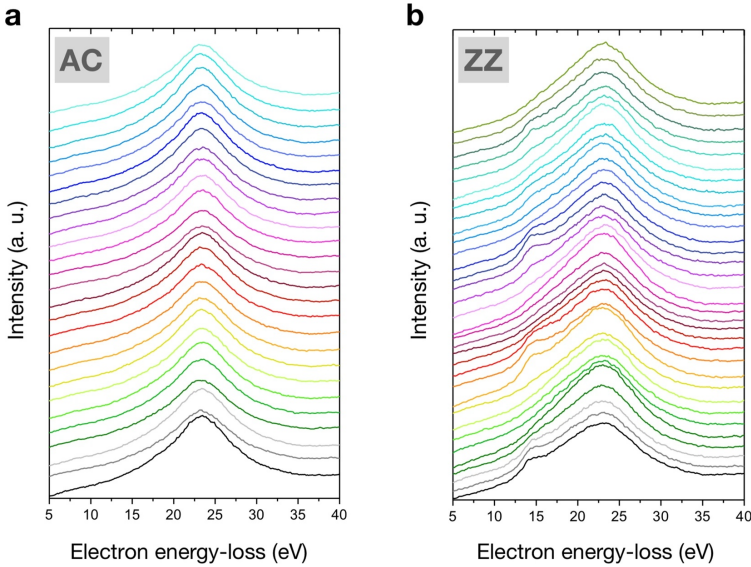
Figure 4.4: EELS spectra taken at different positions of the armchair (a) and zig-zag (b) nanowalls respectively, for the region of electron energy losses between 5 and 40 eV. Each curve corresponds to a different position along the nanowalls, spaced 1 nm apart.

tric material under some external excitation, such as an electron beam [29]. That could correspond to the oscillatory character present in our EELS spectra. Therefore, from this analysis, we can conclude that the ZZ MoS₂ NWs surfaces present a clear metallic character. On the contrary, the AC MoS₂ NWs do not exhibit such metallic behavior. With this result, we can hereby confirm that the ZZ MoS₂ NWs are dominantly enclosed by zig-zag edges structures. It is also worth mentioning here that no signal arising from neither the metal layer nor the Ga used for the FIB milling were present at any of the acquired EELS spectra, indicating that the possible contamination from Ga in the nanowalls is non-existing.

4.5. Aв -initio calculation of the density of states in MoS₂ nanowalls

In order to further validate the onset of the metallic behavior observed in the ZZ MoS₂ nanowalls, we calculated the corresponding density of states (DoS) by means of *ab-initio* calculations in the framework of density functional theory (DFT). The van der Waals (vdW) interactions characteristic of MoS₂ were incorporated by using the non-local vdW functional model [30] as implemented in the `WIEN2k` code [31]. The density of states calculations were performed using both linearized augmented plane wave (LAPW) and local orbitals (LO) methods implemented in the `WIEN2k` package.
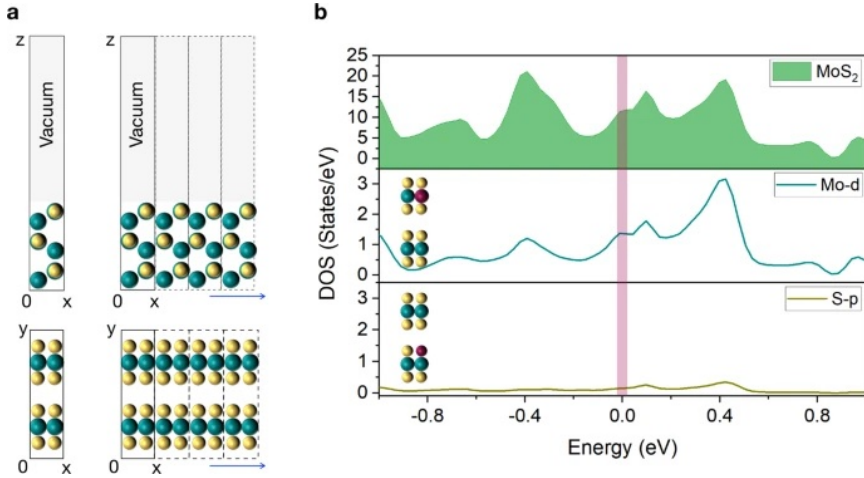
Figure 4.5: (a) The ZZ MoS$_2$ nanowall can be modelled by constructing a $1 \times 3 \times 1$ supercell with vacuum in the z direction. A vacuum layer with length of 17.170 Å was inserted along the ZZ edge of the nanowall, in order to to avoid spurious interactions between the repeating supercell images. This $1 \times 3 \times 1$ supercell in the x and z directions was used to determine the density of states associated to the ZZ MoS$_2$ nanowall, which can be treated as a two-dimensional sheet composed by ZZ nanorribons stacked along the y direction. (b) Density of states of ZZ MoS$_2$ nanowalls (top panel) and the individual contributions to the DOS from the Mo and S atoms located at the ZZ surface (central and bottom panels).

In these calculations, the nonlocal van der Waals [32, 33] (vdW) interactions used for the DoS calculations adopts optB88 [34] for the exchange term, the local density approximation [35] (LDA) for the correlation term, and the DRSLL kernel for the non-local term [36]. For the non-local vdW integration, the cut-off density r$_c$ was set to 0.3 bohr^{-3}, while the plane wave expansion cut-off G$_{max}$ was set to 20 bohr^{-1}. No spin polarization was considered. The lattice parameters were found by volume and force optimization of the supercell, such that the force on each atom was less than 1.0 mRy/bohr.

The total energy convergence criteria was set to be 0.1 mRy between self-consistent field (SCF) cycles, while the charge convergence criteria was set to 0.001e, with e the elementary unit charge. The core and valence electron states were separated by an energy gap of 6.0 Ry. Furthermore, the calculations used an $R \times k_{max}$ value of 6.0, where R is the radius of the smallest Muffin Tin sphere, and k_{max} is the largest k-vector. The first Brillouin zone for the lattice parameter calculations was sampled with 100 k-points using the tetrahedon method of Blöchl et al. [37], which corresponds to 21 k-points in the irreducible Brillouin zone. With the above parameters the optimized lattice parameters were a = 3.107Å and c = 12.087Å, which are in good agreement with the experimental values a = 3.161Å and c = 12.295 Å [38].

The DoS was calculated with a denser k-point sampling of the Brillouin zone consisting of 1600 k-points, corresponding to 630 k-points in the irreducible Brillouin zone. We modeled the ZZ MoS$_2$ nanowall by constructing a $1 \times 3 \times 1$ supercell of MoS$_2$, as shown in Figure 4.5a. In order to minimize the interactions between periodic images due to the

3D boundary conditions, we introduced a vacuum layer such that the distance between periodic images is 17.170 Å.

The resulting calculated total DoS for the ZZ MoS_2 nanowalls is displayed in Figure 4.5b. A clear absence of a gap in the DOS near the Fermi energy is observed, which implies a finite probability (11.65 states/eV) for states just below and above the Fermi energy level being populated, highlighting the metallic behavior of the ZZ MoS_2 NWs. Figure 4.5b (middle panel) also displays the individual contributions of the 4d states of Mo atoms located at the surface of the ZZ MoS_2 nanowall. These 4d states of Mo are also observed to cross over the Fermi energy (1.35 states/eV), contributing therefore to the metallic character of the ZZ MoS_2 nanowall. The individual contribution of the 3p states of S atoms located at the surface of the NW turns out to be much smaller from the DFT calculation, 0.08 states/eV. Therefore, the dominant contribution to the metallic character of ZZ MoS_2 nanowalls can be confidently attributed to Mo-4d states of MoS_2.

4.6. CONCLUSION

In this study we have presented a novel approach for the top-down fabrication of ordered vertically-oriented MoS_2 nanostructures (denoted as nanowalls) which makes possible to achieve at the same time, a large density of exposed active edge sites while also to controllably select whether these are of the AC or ZZ types. The crystallographic nature of the exposed surfaces has been validated by means of high-resolution TEM measurements. We have also studied the local electronic properties of these NW surfaces by means of EELS, finding direct evidence of the metallic character of the ZZ surfaces as indicated by the presence of MoS_2 surface plasmon peak.

The metallic nature of the ZZ MoS_2 nanowalls demonstrated in this work could be exploited to open new opportunities for nanoengineering the edge type in MoS_2 nanostructures, as well as in related layered materials for example within the TMD family. These prospects could impact both for fundamental physics and technological applications in fields such as electronics, optoelectronics, photovoltaics, and photocatalysts.

REFERENCES

[1] B. Bhattacharyya, A. Sharma, B. Sinha, K. Shah, S. Jejurikar, T. D. Senguttuvan, and S. Husale, *Evidence of robust 2D transport and Efros-Shklovskii variable range hopping in disordered topological insulator (Bi_2Se_3) nanowires,* Scientific Reports **7**, 7825 (2017).

[2] B. Bhattacharyya, A. Sharma, V. P. S. Awana, A. K. Srivastava, T. D. Senguttuvan, and S. Husale, *Observation of quantum oscillations in FIB fabricated nanowires of topological insulator (Bi_2Se_3),* Journal of Physics: Condensed Matter **29**, 115602 (2017).

[3] K. F. Mak, C. Lee, J. Hone, J. Shan, and T. F. Heinz, *Atomically Thin MoS_2: A New Direct-Gap Semiconductor,* Phys. Rev. Lett. **105**, 136805 (2010).

[4] A. Splendiani, L. Sun, Y. Zhang, T. Li, J. Kim, C.-Y. Chim, G. Galli, and F. Wang,

Emerging Photoluminescence in Monolayer MoS$_2$, Nano Letters **10**, 1271 (2010), https://doi.org/10.1021/nl903868w .

[5] B. Radisavljevic, A. Radenovic, J. Brivio, V. Giacometti, and A. Kis, *Single-layer MoS$_2$ transistors,* Nature Nanotechnology **6**, 147 (2011).

[6] K. F. Mak, K. He, J. Shan, and T. F. Heinz, *Control of valley polarization in monolayer MoS$_2$ by optical helicity,* Nature Nanotechnology **7**, 494 (2012).

[7] Y. Li, Z. Zhou, S. Zhang, and Z. Chen, *MoS$_2$ Nanoribbons: High Stability and Unusual Electronic and Magnetic Properties,* Journal of the American Chemical Society **130**, 16739 (2008), pMID: 19007118, https://doi.org/10.1021/ja805545x .

[8] H. Pan and Y.-W. Zhang, *Edge-dependent structural, electronic and magnetic properties of MoS$_2$ nanoribbons,* J. Mater. Chem. **22**, 7280 (2012).

[9] D. Davelou, G. Kopidakis, G. Kioseoglou, and I. N. Remediakis, *MoS$_2$ nanostructures: Semiconductors with metallic edges,* Solid State Communications **192**, 42 (2014).

[10] J. V. Lauritsen, M. Nyberg, R. T. Vang, M. V. Bollinger, B. S. Clausen, H. T. e, K. W. Jacobsen, E. L. gsgaard, J. K. N. rskov, and F. Besenbacher, *Chemistry of one-dimensional metallic edge states in MoS$_2$ nanoclusters,* Nanotechnology **14**, 385 (2003).

[11] T. P. Rossi, K. T. Winther, K. W. Jacobsen, R. M. Nieminen, M. J. Puska, and K. S. Thygesen, *Effect of edge plasmons on the optical properties of MoS$_2$ monolayer flakes,* Phys. Rev. B **96**, 155407 (2017).

[12] J. Kibsgaard, Z. Chen, B. N. Reinecke, and T. F. Jaramillo, *Engineering the surface structure of MoS$_2$ to preferentially expose active edge sites for electrocatalysis,* Nature Materials **11**, 963 (2012).

[13] D. Voiry, M. Salehi, R. Silva, T. Fujita, M. Chen, T. Asefa, V. B. Shenoy, G. Eda, and M. Chhowalla, *Conducting MoS$_2$ Nanosheets as Catalysts for Hydrogen Evolution Reaction,* Nano Letters **13**, 6222 (2013), pMID: 24251828, https://doi.org/10.1021/nl403661s .

[14] M. A. Lukowski, A. S. Daniel, F. Meng, A. Forticaux, L. Li, and S. Jin, *Enhanced Hydrogen Evolution Catalysis from Chemically Exfoliated Metallic MoS$_2$ Nanosheets,* Journal of the American Chemical Society **135**, 10274 (2013), pMID: 23790049, https://doi.org/10.1021/ja404523s .

[15] T. F. Jaramillo, K. P. Jørgensen, J. Bonde, J. H. Nielsen, S. Horch, and I. Chorkendorff, *Identification of Active Edge Sites for Electrochemical H$_2$ Evolution from MoS$_2$ Nanocatalysts,* Science **317**, 100 (2007), https://science.sciencemag.org/content/317/5834/100.full.pdf .

[16] M.-A. Kang, S. K. Kim, J. K. Han, S. J. Kim, S.-J. Chang, C.-Y. Park, S. Myung, W. Song, S. S. Lee, J. Lim, and K.-S. An, *Large scale growth of vertically standing MoS$_2$ flakes on 2D nanosheet using organic promoter,* 2D Materials **4**, 025042 (2017).

[17] A. V. Agrawal, N. Kumar, S. Venkatesan, A. Zakhidov, C. Manspeaker, Z. Zhu, F. Robles Hernandez, J. Bao, and M. Kumar, *Controlled Growth of MoS$_2$ Flakes from in-Plane to Edge-Enriched 3D Network and Their Surface-Energy Studies,* ACS Applied Nano Materials **1**, 2356 (2018), https://doi.org/10.1021/acsanm.8b00467 .

[18] Y. Teng, H. Zhao, Z. Zhang, Z. Li, Q. Xia, Y. Zhang, L. Zhao, X. Du, Z. Du, P. Lv, and K. Åwierczek, *MoS$_2$ Nanosheets Vertically Grown on Graphene Sheets for Lithium-Ion Battery Anodes,* ACS Nano **10**, 8526 (2016), pMID: 27556425, https://doi.org/10.1021/acsnano.6b03683 .

[19] X. Zeng, H. Hirwa, M. Ortel, H. C. Nerl, V. Nicolosi, and V. Wagner, *Growth of large sized two-dimensional MoS$_2$ flakes in aqueous solution,* Nanoscale **9**, 6575 (2017).

[20] X. Wang, H. Feng, Y. Wu, and L. Jiao, *Controlled Synthesis of Highly Crystalline MoS$_2$ Flakes by Chemical Vapor Deposition,* Journal of the American Chemical Society **135**, 5304 (2013), pMID: 23489053, https://doi.org/10.1021/ja4013485 .

[21] Y. Jung, J. Shen, Y. Sun, and J. J. Cha, *Chemically Synthesized Heterostructures of Two-Dimensional Molybdenum/Tungsten-Based Dichalcogenides with Vertically Aligned Layers,* ACS Nano **8**, 9550 (2014), pMID: 25153809, https://doi.org/10.1021/nn503853a .

[22] D. Kong, H. Wang, J. J. Cha, M. Pasta, K. J. Koski, J. Yao, and Y. Cui, *Synthesis of MoS$_2$ and MoSe$_2$ Films with Vertically Aligned Layers,* Nano Letters **13**, 1341 (2013), pMID: 23387444, https://doi.org/10.1021/nl400258t .

[23] H. Wang, C. Tsai, D. Kong, K. Chan, F. Abild-Pedersen, J. K. Nørskov, and Y. Cui, *Transition-metal doped edge sites in vertically aligned MoS$_2$ catalysts for enhanced hydrogen evolution,* Nano Research **8**, 566 (2015).

[24] S. Friedensen, J. T. Mlack, and M. Drndić, *Materials analysis and focused ion beam nanofabrication of topological insulator Bi$_2$Se$_3$,* Scientific Reports **7**, 13466 (2017).

[25] P. A. Sharma, A. L. Lima Sharma, M. Hekmaty, K. Hattar, V. Stavila, R. Goeke, K. Erickson, D. L. Medlin, M. Brahlek, N. Koirala, and S. Oh, *Ion beam modification of topological insulator bismuth selenide,* Applied Physics Letters **105**, 242106 (2014), https://doi.org/10.1063/1.4904936 .

[26] D. S. Fox, Y. Zhou, P. Maguire, A. OâNeill, C. ÃâCoileÃ¡in, R. Gatensby, A. M. Glushenkov, T. Tao, G. S. Duesberg, I. V. Shvets, M. Abid, M. Abid, H.-C. Wu, Y. Chen, J. N. Coleman, J. F. Donegan, and H. Zhang, *Nanopatterning and Electrical Tuning of MoS$_2$ Layers with a Subnanometer Helium Ion Beam,* Nano Letters **15**, 5307 (2015), pMID: 26154305, https://doi.org/10.1021/acs.nanolett.5b01673 .

4

[27] B. Yue, F. Hong, K.-D. Tsuei, N. Hiraoka, Y.-H. Wu, V. M. Silkin, B. Chen, and H.-k. Mao, *High-energy electronic excitations in a bulk MoS$_2$ single crystal,* Phys. Rev. B **96**, 125118 (2017).

[28] L. Martin, R. Mamy, A. Couget, and C. Raisin, *Optical Properties and Collective Excitations in MoS$_2$ and NbSe$_2$ in the 1.7 to 30 eV Range,* physica status solidi (b) **58**, 623 (1973), https://onlinelibrary.wiley.com/doi/pdf/10.1002/pssb.2220580223 .

[29] D. N. Basov, M. M. Fogler, and F. J. García de Abajo, *Polaritons in van der Waals materials,* Science **354** (2016), 10.1126/science.aag1992, https://science.sciencemag.org/content/354/6309/aag1992.full.pdf .

[30] F. Tran, J. Stelzl, D. Koller, T. Ruh, and P. Blaha, *Simple way to apply nonlocal van der Waals functionals within all-electron methods,* Phys. Rev. B **96**, 054103 (2017).

[31] P. Blaha, K. Schwarz, G. K. H. Madsen, D. Kvasnicka, L. J., L. R., F. Tran, and L. D. Marks, *WIEN2k, An Augmented Plane Wave + Local Orbitals Program for Calculating Crystal Properties (Karlheinz Schwarz, Techn. Universität Wien, Austria), 2018. ISBN 3-9501031-1-2,* .

[32] J. Klimeš, D. R. Bowler, and A. Michaelides, *Chemical accuracy for the van der Waals density functional,* Journal of Physics: Condensed Matter **22**, 022201 (2009).

[33] J. c. v. Klimeš, D. R. Bowler, and A. Michaelides, *Van der Waals density functionals applied to solids,* Phys. Rev. B **83**, 195131 (2011).

[34] A. D. Becke, *Density-functional exchange-energy approximation with correct asymptotic behavior,* Phys. Rev. A **38**, 3098 (1988).

[35] J. P. Perdew and Y. Wang, *Accurate and simple analytic representation of the electron-gas correlation energy,* Phys. Rev. B **45**, 13244 (1992).

[36] M. Dion, H. Rydberg, E. Schröder, D. C. Langreth, and B. I. Lundqvist, *Van der Waals Density Functional for General Geometries,* Phys. Rev. Lett. **92**, 246401 (2004).

[37] P. E. Blöchl, O. Jepsen, and O. K. Andersen, *Improved tetrahedron method for Brillouin-zone integrations,* Phys. Rev. B **49**, 16223 (1994).

[38] B. Schönfeld, J. J. Huang, and S. C. Moss, *Anisotropic mean-square displacements (MSD) in single-crystals of 2H- and 3R-MoS$_2$,* Acta Crystallographica Section B **39**, 404 (1983).

5

MOLYBDENUM NANOPILLAR ARRAYS: FABRICATION AND ENGINEERING

In the previous chapters we have studied the edge properties of flakes of exfoliated MoS$_2$. The exfoliation process of the flakes is one of limited control and scalability. As a consequence of the limitations of the exfoliation process we do not have control of the specific edge structures formed and the total amount of exposed edges of an exfoliated flake. An alternative to exfoliation is the use of top-down and bottom-up approaches to have the desired control of the structural properties of transition metal dichalcogenides (TMDs). In this chapter we report on the large-scale fabrication of molybdenum (Mo) nanopillar (NP) arrays with NP widths down to 75 nm by means of deep-reactive ion etching at cryogenic temperatures. A variable-thickness Mo metal layer sputtered onto a Si$_3$N$_4$/Si substrate makes possible NPs with different lengths in a controllable manner. We demonstrate how our fabrication strategy leads to tunable cross-sections with different geometries, including hexagonal, cylindrical, square and triangular shapes, by using electron beam lithography on hydrogen silsesquioxane negative tone resist. To ensure well-defined facets and surfaces, we employ deep-reactive ion etching in a gas mixture of SF$_6$ and O$_2$ at cryogenic temperatures in an inductively coupled plasma reactive ion etching (ICP-RIE) system. Furthermore, these Mo NPs will represent the template for the fabrication of core-shell Mo-MoS$_2$ one-dimensional nanostructures to be discussed in Chapter 6. These results represent an attractive route towards the realization of high-density TMDs NP arrays for applications from nanoelectronics to quantum sensing and hydrogen evolution reaction catalysis.

5.1. Introduction

One-dimensional (1D) Molybdenum (Mo) nanostructures have garnered significant attention recently due to their potential uses in a wealth of applications from interconnects in nanoelectronic devices to promoting the hydrogen evolution reaction [1–6]. This potential stems from their remarkable properties, such as efficient electron emission and structural stability

Of particular interest for applications in nanoelectronics is the fact that 1D Mo nanostructures exhibit reduced resistivity is their widths are decreased [1], thus making 1D Mo nanostructures promising candidates for interconnects for nanodevices. Furthermore, arranging 1D Mo nanostructures into geometric arrays whose axis is perpendicular to the substrate surface represents one of the main challenges for concerning their integration into nanoelectronic applications. Previous works have extensively studied the bottom-up fabrication of 1D Mo nanostructures, focusing mostly on approaches such as electrodeposition and reduction, hydrogenation, and chemical vapour deposition [1–7]. However, these approaches have some limitations in terms of scalability as well as concerning the control on the orientation, shape, and density of the 1D nanostructures at spatially well-defined locations.

With this motivation, the main goal of this work is to bridge this gap by demonstrating a novel top-down approach for the large-scale fabrication of 1D Mo nanostructures, denoted in the following as nanopillars (NPs), arrays whose shape, width, pitch, and length can be fully controlled by deploying a combination of sputter-deposition, electron beam lithography, and cryogenic deep-reactive ion etching techniques. Our strategy for the large-scale fabrication of Mo NPs draws inspiration from the cryogenic deep-reactive ion etching of silicon, where micron-depth smooth vertical sidewalls can be formed when using a SF_6/O_2 gas mixture [8–12].

The close similarity between the etching processes of refractory metals and of Si suggests that a cryogenic deep-reactive ion etching process could be adopted to fabricate nanostructures with well-defined sidewalls also in the case of Mo. Taking into account these considerations, in this work we modify the electron beam lithography and cryogenic deep-reactive ion etching procedure for Si NP fabrication [13–16]to fabricate Mo NPs. We believe that these results would enable a wide range of technological applications.

5.2. Fabrication of Mo Nanopillars

Here we modify the electron beam lithography and cryogenic deep reactive ion etching procedure for Si NP fabrication [13–16] to fabricate Mo NPs. We show how the adhesion layer and development process for the used resists for electron lithography can affect the patterned Mo. Our fabrication strategy is schematically displayed in Figure 5.1. Pieces of 1 x 1cm^2 p-doped Si(001) are used throughout the whole process. Firstly, the Si pieces are cleaned via the RCA process [17]. Secondly, a low-stress Si_3N_4 layer is grown on top of the silicon pieces by means of low pressure chemical vapour deposition (LPCVD) in a Tempress furnace. The Si_3N_4 layer is used as a protective layer for the Si pieces, since it is well-known that Si is also etched in SF_6/O_2 gas mixtures. Subsequently, a layer of
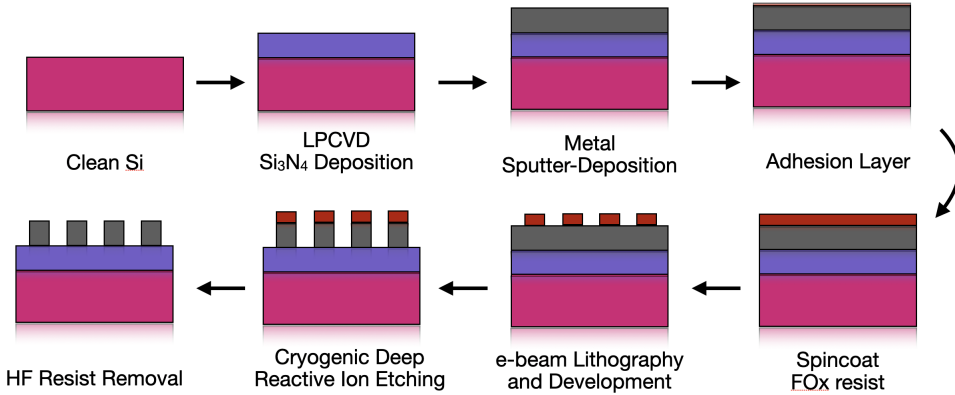
Figure 5.1: Schematic of the fabrication approach of the Mo NP arrays adopted in this work. The process starts with the LPCVD deposition of the Si_3N_4 layer and ends with the HF resist removal which reveals the NP arrays.

5

molybdenum (Mo) is sputter-deposited on top of this Si_3N_4 layer by using an Alliance Concept Ac 450 sputter-deposition system with an DC power of 100 W at a pressure of 3.4 μbar.

5.2.1. ELECTRON-BEAM LITHOGRAPHY

Afterwards, a spin coating of negative tone resist is carried out on top of the Mo metal layer. Crucially, in order to ensure the desired NP dimensions, the resist mask needs to have high plasma resistance while also being able to maintain the mask shape during the etching process. To fulfill these requirements, Flowable Oxide-16 (FOx-16) and Flowable Oxide-25, (FOx-25) from Dow Corning were adopted in this work [18].

Before applying the FOx resist, a monolayer of HexaMethylDiSilazane (HMDS) adhesion promoter is evaporated on top of the metal layer using a Delta RC80 apparatus from Suss Microtech [19]. The FOx resist is left to warm up to room temperature [20] and then a spincoat speed between 1500 and 10000 rpm is used to acquire a uniform resist layer on the samples. A resist thickness between 800 nm and 400 nm was achieved with the FOx-25 resist for the used spincoat speeds, while for the case of FOx-16 a resist thickness between 600 nm and 400 nm is achieved.

The samples are then baked on hotplates in two consecutive baking steps of 150 C and 220° C for 2 minutes each. The desired NP arrays patterns are written in a RAITH 5000+ EBPG or in a RAITH 5200 EBPG system at 100 keV accelerating voltage. Proximity Effect Correction (PEC) was implemented via a Monte Carlo approach in the TRACER program from GenISys GmbH to ensure sharp edges of the smallest NP patterns. The optimal dose depends both on the size of the NP patterns and on the pitch-to-pitch distance between NPs. It is found that a larger dose is needed when decreasing the size of the NP patterns and that resist NP widths down to 30 nm are achieved by the combination of large dose and small pitch-to-pitch NP distance. After exposure, the FOx-16 was developed in 6.25% TMAH for 45 seconds at room temperature. In the case of FOx-25 resist, a

different development procedure is required when resist layers thicker than 600 nm are used as described below.

5.2.2. Cryogenic Deep Reactive Ion Etching

Vertical sidewall formation in silicon is achieved via cryogenic deep reactive ion etching in a SF_6/O_2 gas mixture [8–12]. The fabrication of sharp vertical sidewalls is achieved by a combination of sidewall protection due to a passivation layer along the sidewalls and a reduction in the reaction probability of chemical etching [21–24]. In the SF_6/O_2 plasma SF_6 decomposes into SF_5^+ ions and F radicals. Ion bombardment of the radicals with silicon in the SF_6/O_2 plasma results in the formation of volatile SiF_4 which is pumped away during etching. An oxyfluoride layer of SiO_xF_y (x =1,2 ,y = 2,4) is formed alongside the formation of SiF_4. The SF_5^+ ions locally etch away SiO_xF_y, where the etching of SiO_xF_y is a chemical etching process and depends strongly on the process temperature. The chemical etching of SiO_xF_y is reduced by etching the silicon at cryogenic temperatures [10, 13, 22, 25–27].

Similarly, in fluorine-oxygen based plasma etching of refractory metals Me (Me = Mo or W) a metal hexafluoride MeF_6 compound is formed along with an oxyfluoride layer MeO_xF_y [17, 27, 28], where the formed MeO_xF_y is less volatile than MeF_6 [29–31]. As in the case of silicon, the more volatile MeF_6 is pumped away during etching, while the MeO_xF_y formation reduces the etch rate of the metal [30, 31]. The MeO_xF_y is etched away in a chemical etching process by ions formed in the plasma.

Different SF_6/O_2 mixtures were used in order to acquire the optimal etch-passivation ratio, with the most successful mixture being a gas mixture of 200.0 sccm SF_6 and 5.0 sccm O_2. A platen power of 70 W combined with an ICP power of 1100 W was used to etch the NP structures. With these conditions, an etch rate of 140 nm/min was found for the Mo structures. Cryogenic deep reactive ion etching of the developed samples was subsequently carried out in an Oxford Instruments PlasmaPro 100 Estrelas system. The sample was placed on a carrier wafer that is clamped to a cryogenic holder which was cooled by a flow of liquid N_2. Helium backing is used to ensure proper thermal contact between the holder and the sample.

Before starting the etch a 30 minute O_2 plasma clean of the chamber is carried out at -20°C. The system is subsequently cooled down to the etching temperature of -100°C ±2°C. The etching was carried out in pulsed sequences of 100 kHz with a duty cycle of 10%. The slit-valve was left fully opened to ensure the lowest possible pressure during the etch. A three minute pre-conditioning step of the chamber is carried out in order to encourage reproducibility between different etching sessions [32]. Fomblin oil was placed between the sample and carrier wafer to further improve thermal contact. A waiting time of 1 minute is carried out after the carrier wafer with the sample is placed inside the process chamber.

5.2.3. Removal of Residual Resist

After cryogenic etching the remaining FOx resist, along with the SiO_2 adhesion layer, is removed by a diluted solution of hydrofluoric acid (HF). A 5% HF dip for 120 seconds
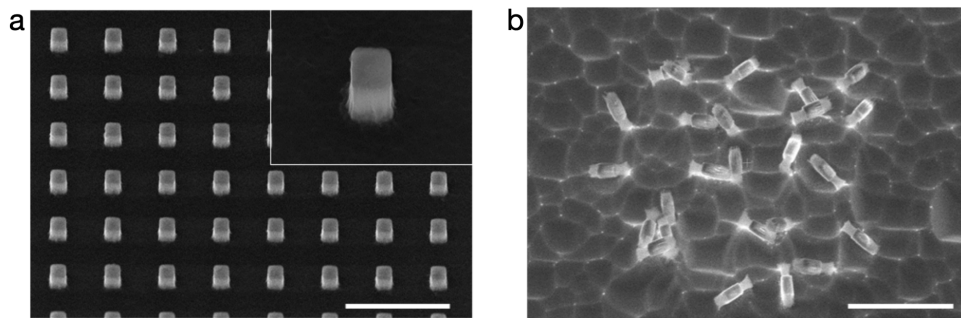
Figure 5.2: SEM images of Mo NPs with square cross-sections fabricated on top of a Si wafer either with (a) and without (b) a protective Si_3N_4 layer, demonstrating how only in the first case a regular NP array is obtained. The inset in (a) displays a representative NP. The scale bar is 2 μm.

resulted in all the FOx resist and SiO_2 being removed from the NP structures. We also note that the HF dip did not affect the shape of the NPs and barely etched away any of the underlying Si_3N_4.

5.3. RESULTS

5.3.1. HMDS ADHESION LAYER

Figure 5.2a displays an array of Mo NPs with square cross-sections, with the inset focusing on a representative NP, demonstrating that a high yield of Mo NPs characterized by regular sidewalls is achieved. In Figure 5.2 a 340 nm film of Mo was used for the NP fabrication. Figure 5.2b illustrates the role played by the Si_3N_4 protective layer in the fabrication process: since the etch chemistry for Mo is presumably different from the one required for Si etching the underlying Si is etched away at a higher rate than the Mo. In turn, this higher Si etch rate leads to an undercut that results into the Mo NPs toppling onto the Si substrate.

To further demonstrate how our fabrication strategy offers precise control on the geometry of the resulting Mo NPs, equilateral triangles, circular, and hexagonal patterns are designed in a 500 nm Mo film and the resulting Mo NP arrays are displayed in Figure 5.3. The insets are top views of the respective NPs, highlighting the corresponding geometrical cross-sections. One can observe from Figure 5.3 how Mo regular arrays of NPs with well-defined facets and varying cross-sectional shapes can be reliably fabricated for large (between 200 nm and 300 nm) nanostructures where their shapes are retained down to the 100 nm range.

Furthermore, NP arrays with varying pitches are designed in order to determine the minimum distance achievable between the NPs of an array. The results for this pitch distance analysis are presented in Figure 5.4. A minimum pitch distance of 300 nm was achieved in the case of NP with widths of 100 nm. It is found that decreasing the NP dimensions results in smaller pitch distances available before overexposure results. The dosage required for the different NP shapes does not vary significantly when considering the total
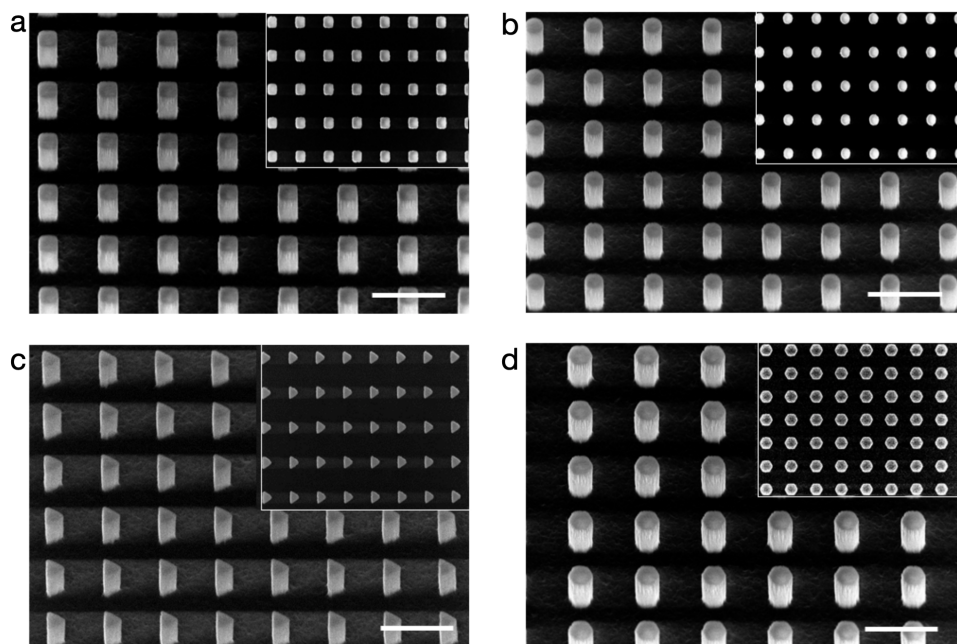
Figure 5.3: SEM images of regular arrays of Mo NPs exhibiting (a) square, (b) circular, (c) triangular, and (d) hexagonal cross-sections respectively, as illustrated by the corresponding top-view images shown in the insets. The scale bar is 1 μm.

area of each respective NP, as indicated in Figure 5.5.

5.3.2. SiO$_2$ ADHESION LAYER

During the optimization process for the NP structures both the FOx-16 and FOx-25 reached their shelf-life. One of the effects of the aged resist is the observation of a worsening of the adhesion of the resists to the Mo surface, even when HMDS is used as an adhesion promotor. In order to reacquire good adhesion to the Mo surface a SiO$_2$ layer was used as an alternative adhesion layer due to its close similarity to the FOx molecular structure. We note that FOx resists consists of a cage-like structure of Si-H and Si-O bonds. After exposure and development of the FOx resists the Si-H bonds are broken and only the Si-O bonds are left [32, 33]. Due to the remaining Si-O bonds in the FOx patterns a thin layer of SiO$_2$ was used as an alternative to HMDS as an adhesion layer.

Before applying the FOx resist a 15 nm layer of SiO$_2$ on top of the Mo metal was deposited via Plasma Enhanced Chemical Vapour Deposition (PECVD) in an Oxford Instruments PlasmaPro 80 system.

After exposure the FOx was developed in heated Microposit MF321 at 50°C for 5 minutes, followed by a 30 second dip in H$_2$O. After the H$_2$O dip the samples were placed in a beaker filled with isopropanol, with care being taken such that the surface of the substrates always has liquid on it when transferring the substrates to the different solutions
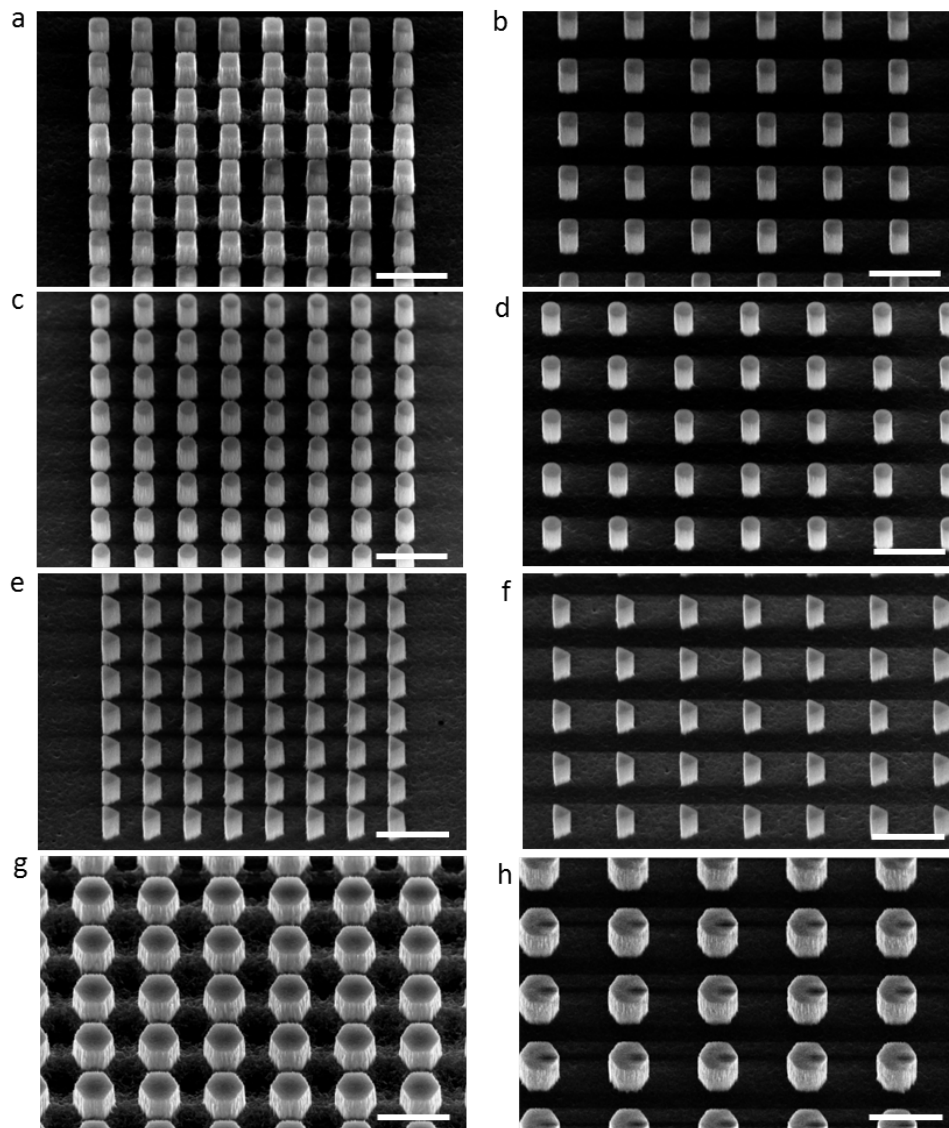
Figure 5.4: Different pitches for Mo NP arrays with a pitch of 300 nm (a,c,e,g) and of 600 nm (b,d,f,h). As in Figure 5.3 these NP exhibit square (a,b), circular (c,d), triangular (e,f) and hexagonal (g,h) cross-sections respectively. The scale bar is 1 μm
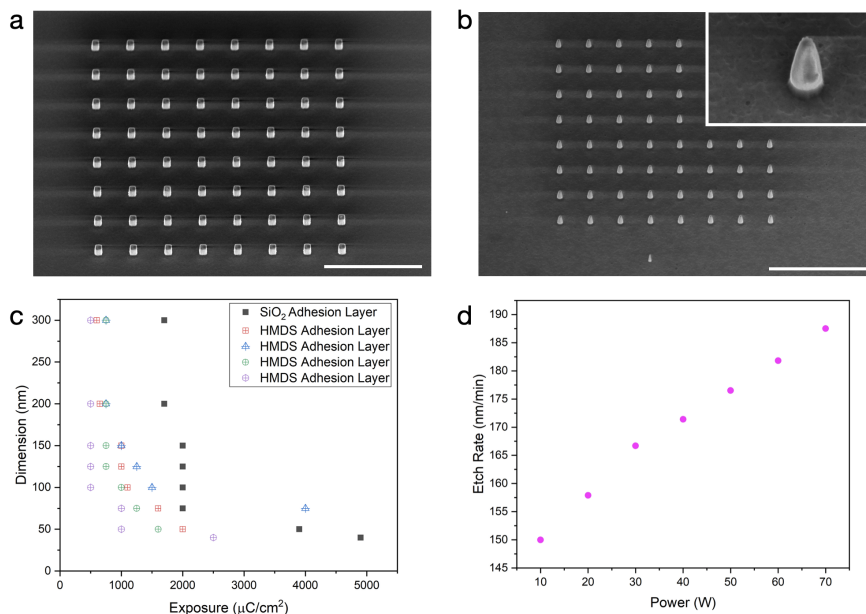
Figure 5.5: (a) SEM images of the Mo NP array with square cross-sections fabricated with the modified resist recipe. (b) Same as (a) now for Mo nanocone arrays. Both in (a) and (b) the scale bar is 5 μm. (c) Dosage needed as function of the nanostructure dimensions. The shape of each marker is the same as the cross-section of the corresponding NPs. (d)Etch rate (in nm/min) as a function of the platen power at 1100 W ICP power.

mentioned above. After the development step the samples are placed in a Leica super critical CO_2 drying system. The use of supercritical resist drying is known to be advantageous when patterning resist structures with large aspect-ratios [7, 34–36]. We note that the combination of critical point drying (CPD) together with SiO_2 as an adhesion layer is necessary to counteract the aged FOx resist issue. In Figure 5.5 the nanostructures fabricated with the modified resist recipe can be seen.

First of all, with the modified recipe we are able to reproduce NP structures with the desired etch profile, as shown in Figure 5.5a for the case of NPs with square cross-sections. Furthermore, we are able to fabricate NPs of Mo where the base is noticeably wider than the top, which will be referred to as nanocones in the following, and that are displayed in Figure 5.5b. The fabrication of such Mo nanocones is achieved by slightly modifying the etching process.

For the etching procedure of the straight sidewall structures, a Si carrier wafer is used where a thick layer of SiO_2 is deposited via LPCVD. Instead, for the nanocones etching procedure, a Si carrier wafer is used where both sides have a thick layer of SiO_2. For these Mo nanocones, only a square design for the patterned HSQ resist was used. The Mo nanocones tend to retain the shape profile of the HSQ resist at the top of the nanocone for all patterned diameters. The morphology along the entire length of the nanocone depends on the lateral size of the HSQ resist structure at the top of the nanocone. Mo

nanocones with a patterned HSQ width between 200 nm - 300 nm retain the square shape along the entire nanocone length. The sharp edges of the nanocones tend to become rounded for smaller HSQ resist diameters after etching.

In both lithographic processes (leading to the square cross-section NP and the nanocones) we observed that the dosage needed to produce nanostructures of specific diameters varies with the size of these structures. Figure 5.5c displays the dose required for specific dimensions and shapes of the resulting Mo NPs. In both cases, it is found that the smaller structures require a higher exposure. Additionally, in order to ensure straight sidewalls, it is necessary to avoid a too high platen power which could etch away the FOx resist before all the unexposed Mo metal is etched away. Figure 5.5d indicates the etch rate as a function of platen power at fixed ICP power and gas flows. For the sub-150 nm structures, lower platen power (below 70 W) results in the formation of straight sidewalls in the Mo metal.

We note that the etch rate in the ICP-RIE system changed abruptly during the optimization process and Figure 5.5d denotes the current etch rates for Mo in the Oxford Instruments PlasmaPro 100 Estrelas ICP-RIE system. A higher etch rate for the Mo NP structures was found after the abrupt etch rate change. Decreasing the platen power led to recovering the Mo NP structures with the desired etch profiles. The etch rate in ICP-RIE systems tend to drift over time, which could be a consequence of a change in the process chamber, e.g Helium leakage into the process chamber, or using different clamping rings in the process chamber [37, 38]. As of writing the etch rates denoted in Figure 5.5d have remained stable. Further research is necessary to understand the origin of the abrupt change in etch rate of the ICP-RIE system.

5.3.3. High-Aspect Ratio Structures
Finally, in Figure 5.6 the limits of our modified and unmodified resist recipes and etching procedures can be seen. In Figure 5.6(a,b) HSQ resist NPs made with the modified resist recipe in a 800 nm thick HSQ layer can be seen. Widths down to 40 nm are achieved at relatively high exposures(~5300 μC/cm^2) with the modified HSQ resist recipe. For resist NP widths below 100 nm a minimum of 100 nm pillar-to-pillar distance can be achieved with the modified resist recipe before overexposure becomes an issue. In Figure 5.6(c,d) square Mo NPs with a length of 880 nm and width down to 60 nm made with a HSQ resist mask of 600 nm using the unmodified recipe can be seen. For the Mo NP structures in Figure 5.6(c,d) the HSQ resist was completely etched away during the cryogenic etching process, which can explain the loss of shape retention of the NP. For both the modified and unmodified resist recipes we note that for features below 75 nm in size the shape of the Mo NPs are not reliably maintained after cryogenic etching.

The loss of shape for small diameters could be due to the very aggressive plasma parameters used. We found that NP widths down to 50 nm can recovered by lowering the platen power to 30 W. We have observed that the exposure needed for the HSQ resist for features greater than 100 nm tends to stay stable over the span of months, while the exposure required for sub-100 nm structures tends to increase as the HSQ resist ages, both for the modified and unmodified resist recipes.
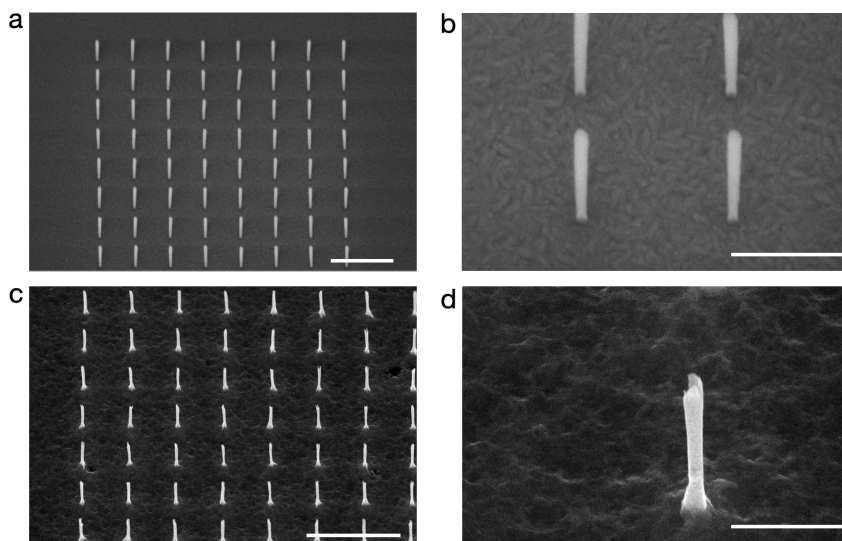
Figure 5.6: (a,b) SEM images of 800 nm thick HSQ resist NP array. Widths down to 40 nm with square cross-sections fabricated with the modified resist recipe. (c,d) Mo metal NPs fabricated with the unmodified resist process, with a length of 880 nm and width of 60 nm. The scale bar in (a) is 1 μm, and the scale bar in (c) is 2 μm. Both in (b) and (d) the scale bar is 400 nm.

5.4. CONCLUSIONS & OUTLOOK

In this chapter, we have demonstrated the feasibility of a novel strategy for the top-down large-scale fabrication of geometric arrays of Mo NPs with different cross-sectional shapes as well as of nanocones. Our approach is based on the combination of electron beam lithography and cryogenic deep-reactive ion etching, and makes possible a precise control on the shapes, lengths, widths, and pitches of the resulting Mo NP arrays, which in all cases are characterized by well-defined smooth sidewalls. The proposed top-down approach is not limited to the fabrication of NPs, since one can easily modify the shape of the etched molybdenum by changing the exposure design of the resist mask. We also note that the use of a SiO$_2$ adhesion layer for the FOx resist might also be implemented for other metals, such as Cu or Au, where adhesion is known to be a problem[19]. In this respect, our method for the deep etching of structures in molybdenum could also be used to etch metals with similar etch chemistries. It is found that the limiting factor for large-aspect ratio of the NPs is the thickness of the resist mask, where the used FOx resist has a low selectivity during cryogenic reactive ion etching of the molybdenum. These results represent an attractive route towards the realization of high-density Mo NP arrays for applications from nanoelectronics to quantum sensing and hydrogen evolution reaction catalysis.

REFERENCES

[1] M. P. Zach, K. H. Ng, and R. M. Penner, *Molybdenum Nanowires by Electrodeposition,* Science **290**, 2120 (2000), https://science.sciencemag.org/content/290/5499/2120.full.pdf .

[2] A. Kovic, A. Znidarsic, A. Jesih, A. Mrzel, M. Gaberscek, and A. Hassanien, *A novel facile synthesis and characterization of molybdenum nanowires,* Nanoscale research letters **7**, 567 (2012).

[3] J. Zhou, S. Deng, L. Gong, Y. Ding, J. Chen, J. Huang, J. Chen, N. Xu, and Z. L. Wang, *Growth of Large-Area Aligned Molybdenum Nanowires by High Temperature Chemical Vapor Deposition: Synthesis, Growth Mechanism, and Device Application,* The Journal of Physical Chemistry B **110**, 10296 (2006), pMID: 16722732, https://doi.org/10.1021/jp061213z .

[4] C. A. Spindt, I. Brodie, L. Humphrey, and E. R. Westerberg, *Physical properties of thin-film field emission cathodes with molybdenum cones,* Journal of Applied Physics **47**, 5248 (1976), https://doi.org/10.1063/1.322600 .

[5] D. Dvorsek, M. Zumer, V. Nemanic, D. Mihailovic, and D. Vengust, *Growth and field emission properties of vertically aligned molybdenum-sulfur-iodine nanowires on molybdenum and quartz substrates,* Journal of Applied Physics **102**, 114308 (2007), https://doi.org/10.1063/1.2820009 .

[6] X. Zhang, F. Zhou, W. Pan, Y. Liang, and R. Wang, *General Construction of Molybdenum-Based Nanowire Arrays for pH-Universal Hydrogen Evolution Electrocatalysis,* Advanced Functional Materials **28**, 1804600 (2018), https://onlinelibrary.wiley.com/doi/pdf/10.1002/adfm.201804600 .

[7] K. S. Yeong and J. T. L. Thong, *Field-emission properties of ultrathin 5nm tungsten nanowire,* Journal of Applied Physics **100**, 114325 (2006), https://aip.scitation.org/doi/pdf/10.1063/1.2400722 .

[8] C. P. D'Emic, K. K. Chan, and J. Blum, *Deep trench plasma etching of single crystal silicon using SF_6/O_2 gas mixtures,* Journal of Vacuum Science & Technology B: Microelectronics and Nanometer Structures Processing, Measurement, and Phenomena **10**, 1105 (1992), https://avs.scitation.org/doi/pdf/10.1116/1.586085 .

[9] T. Syau, B. J. Baliga, and R. W. Hamaker, *Reactive Ion Etching of Silicon Trenches Using SF_6/O_2 Gas Mixtures,* Journal of The Electrochemical Society **138**, 3076 (1991).

[10] B. Wu, A. Kumar, and S. Pamarthy, *High aspect ratio silicon etch: A review,* Journal of Applied Physics **108**, 051101 (2010), https://doi.org/10.1063/1.3474652 .

[11] R. Legtenberg, H. Jansen, M. de Boer, and M. Elwenspoek, *Anisotropic Reactive Ion Etching of Silicon Using SF_6/O_2/CHF_3 Gas Mixtures,* Journal of The Electrochemical Society **142**, 2020 (1995).

5

[12] H. Jansen, M. de Boer, J. Burger, R. Legtenberg, and M. Elwenspoek, *The black silicon method ii:the effect of mask material and loading on the reactive ion etching of deep silicon trenches,* Microelectronic Engineering **27**, 475 (1995).

[13] P. V. Antonov, M. R. Zuiddam, and J. W. M. Frenken, *Fabrication of high-aspect ratio silicon nanopillars for tribological experiments,* Journal of Micro/Nanolithography, MEMS, and MOEMS **14**, 1 (2015).

[14] C. Fischer, J. W. Menezes, S. A. Moshkalev, C. VerÃssimo, A. R. Vaz, and J. W. Swart, *Fabrication of high-aspect ratio silicon nanopillars and nanocones using deep reactive ion etching,* Journal of Vacuum Science & Technology B: Microelectronics and Nanometer Structures Processing, Measurement, and Phenomena **27**, 2732 (2009), https://avs.scitation.org/doi/pdf/10.1116/1.3246359 .

[15] L. S. Golobokova, Y. V. Nastaushev, F. N. Dultsev, D. V. Gulyaev, A. B. Talochkin, and A. V. Latyshev, *Fabrication and optical properties of silicon nanopillars,* Journal of Physics: Conference Series **541**, 012074 (2014).

[16] X.-L. Han, G. Larrieu, P.-F. Fazzini, and E. Dubois, *Realization of ultra dense arrays of vertical silicon nanowires with defect free surface and perfect anisotropy using a top-down approach,* Microelectronic Engineering **88**, 2622 (2011), proceedings of the 36th International Conference on Micro- and Nano-Engineering (MNE).

[17] S. Franssila, *Introduction to Microfabrication, Second Edition* (Bantam, 2010).

[18] A. E. Grigorescu and C. W. Hagen, *Resists for sub-20-nm electron beam lithography with a focus on HSQ: state of the art,* Nanotechnology **20**, 292001 (2009).

[19] Z. Zhang, H. Duan, Y. Wu, W. Zhou, C. Liu, Y. Tang, and H. Li, *Improving the adhesion of hydrogen silsesquioxane (hsq) onto various substrates for electron-beam lithography by surface chemical modification,* Microelectronic Engineering **128**, 59 (2014).

[20] M. Häffner, A. Haug, A. Heeren, M. Fleischer, H. Peisert, T. Chasse, and D. P. Kern, *Influence of temperature on HSQ electron-beam lithography,* Journal of Vacuum Science & Technology B: Microelectronics and Nanometer Structures Processing, Measurement, and Phenomena **25**, 2045 (2007), https://avs.scitation.org/doi/pdf/10.1116/1.2794324 .

[21] M. J. de Boer, J. G. E. Gardeniers, H. V. Jansen, E. Smulders, M. . Gilde, G. Roelofs, J. N. Sasserath, and M. Elwenspoek, *Guidelines for etching silicon MEMS structures using fluorine high-density plasmas at cryogenic temperatures,* Journal of Microelectromechanical Systems **11**, 385 (2002).

[22] S. Tachi, K. Tsujimoto, and S. Okudaira, *Low-temperature reactive ion etching and microwave plasma etching of silicon,* Applied Physics Letters **52**, 616 (1988), https://doi.org/10.1063/1.99382 .

[23] S. Tachi, K. Tsujimoto, S. Arai, and T. Kure, *Low-temperature dry etching,* Journal of Vacuum Science & Technology A **9**, 796 (1991), https://doi.org/10.1116/1.577364 .

[24] K. Tsujimoto, S. Okudaira, and S. Tachi, *Low-Temperature Microwave Plasma Etching of Crystalline Silicon,* Japanese Journal of Applied Physics **30**, 3319 (1991).

[25] N. Chekurov, K. Grigoras, A. Peltonen, S. Franssila, and I. Tittonen, *The fabrication of silicon nanostructures by local gallium implantation and cryogenic deep reactive ion etching,* Nanotechnology **20**, 065307 (2009).

[26] H. Jansen, H. Gardeniers, M. de Boer, M. Elwenspoek, and J. Fluitman, *A survey on the reactive ion etching of silicon in microtechnology,* Journal of Micromechanics and Microengineering **6**, 14 (1996).

[27] H. V. Jansen, M. J. de Boer, S. Unnikrishnan, M. C. Louwerse, and M. C. Elwenspoek, *Black silicon method: X. A review on high speed and selective plasma etching of silicon with profile control: an in-depth comparison between Bosch and cryostat DRIE processes as a roadmap to next generation equipment,* Journal of Micromechanics and Microengineering **19**, 033001 (2009).

[28] S. Ma, Y. Xia, Y. Wang, K. Ren, R. Luo, L. Song, X. Chen, J. Chen, and Y. Jin, *Fabrication and characterization of a tungsten microneedle array based on deep reactive ion etching technology,* Journal of Vacuum Science & Technology B **34**, 052002 (2016), https://doi.org/10.1116/1.4960715 .

[29] T. P. Chow and A. J. Steckl, *Plasma Etching of Refractory Gates for VLSI Applications,* Journal of The Electrochemical Society **131**, 2325 (1984).

[30] W. S. Pan and A. J. Steckl, *Selective reactive ion etching of tungsten films in CHF_3 and other fluorinated gases,* Journal of Vacuum Science & Technology B: Microelectronics Processing and Phenomena **6**, 1073 (1988), https://avs.scitation.org/doi/pdf/10.1116/1.584300 .

[31] A. Picard and G. Turban, *Plasma etching of refractory metals (W, Mo, Ta) and silicon in SF_6 and SF_6-O_2. An analysis of the reaction products,* Plasma Chemistry and Plasma Processing **5**, 333 (1985).

[32] H. Namatsu, Y. Takahashi, K. Yamazaki, T. Yamaguchi, M. Nagase, and K. Kurihara, *Three-dimensional siloxane resist for the formation of nanopatterns with minimum linewidth fluctuations,* Journal of Vacuum Science & Technology B: Microelectronics and Nanometer Structures Processing, Measurement, and Phenomena **16**, 69 (1998), https://avs.scitation.org/doi/pdf/10.1116/1.589837 .

[33] C. L. Frye and W. T. Collins, *Oligomeric silsesquioxanes, (HSiO3/2)n,* Journal of the American Chemical Society **92**, 5586 (1970), https://doi.org/10.1021/ja00722a009 .

[34] T. Wahlbrink and Daniel Küpper and Y.M. Georgiev and J. Bolten and M. Möller and David Küpper and M.C. Lemme and H. Kurz, *Supercritical drying process for high aspect-ratio hsq nano-structures,* Microelectronic Engineering **83**, 1124 (2006), micro- and Nano-Engineering MNE 2005.

5

[35] A. Agarwal and M. J. Kushner, *Seasoning of plasma etching reactors: Ion energy distributions to walls and real-time and run-to-run control strategies,* Journal of Vacuum Science & Technology A **26**, 498 (2008), https://doi.org/10.1116/1.2909966 .

[36] A. N. Chaika, N. N. Orlova, V. N. Semenov, E. Y. Postnova, S. A. Krasnikov, M. G. Lazarev, S. V. Chekmazov, V. Y. Aristov, V. G. Glebovsky, S. I. Bozhko, and I. V. Shvets, *Fabrication of [001]-oriented tungsten tips for high resolution scanning tunneling microscopy,* Scientific Reports **4**, 3742 (2014).

[37] I. Marinkovic, *Optomechanical Devices in the Quantum Regime* (Ph.D. Thesis, Delft University of Technology, 2019).

[38] J. T. Hill, *Nonlinear Optics and Wavelength Translation Via Cavity-Optomechanics* (Ph.D. Thesis, California Institute of Technology, 2013).

5

6

SYNTHESIS AND CHARACTERIZATION OF CORE-SHELL MO-MOS$_2$ NANOPILLARS

The fabrication of two-dimensional (2D) materials, such as transition metal dichalcogenides (TMDs), in geometries beyond the standard platelet-like configuration exhibits significant challenges which severely limit the range of available morphologies. These challenges arise due to the anisotropic character of their bonding, van der Waals out-of-plane while covalent in-plane. Furthermore, industrial applications based on TMDs nanostructures with non-standard morphologies require full control on the size-, morphology- and position on the wafer scale. Such a precise control remains an open problem whose solution would lead to the opening of novel directions in terms of electronic and optoelectronic applications. Here, we report on a novel strategy to fabricate vertical position-controlled Mo-MoS$_2$ core-shell nanopillars (NPs). Metal-molybdenum (Mo) NPs are first patterned on a silicon wafer using lithography and cryo-etching, as described in chapter 5. These Mo NPs are then used as scaffolds for the synthesis of Mo-MoS$_2$ core-shell NPs by exposing them in a rich sulfur environment. Cross-sectional transmission electron microscopy (TEM) analysis reveals the well-defined morphologies and the Mo-MoS$_2$ core-shell nature of the NPs. We demonstrate that individual Mo-MoS$_2$ core-shell NPs exhibit enhanced second order nonlinear optical processes, such as sum frequency generation (SFG). Our results represent an important step towards realising one-dimensional TMD-based nanostructures as building blocks of a new generation of sensors, nanophotonic devices, and hydrogen evolution reactions.

6.1. Introduction

One-dimensional (1D) nanostructures have repeatedly demonstrated their relevance for applications ranging from biological sensors [1–3], single electron emitters [4, 5], to clean energy harvesting [6, 7]. Effectively deploying 1D nanomaterials for such applications requires achieving an excellent and reproducible control of their sizes, shapes, and morphologies. While these conditions have been realised with astonishing degree of precision in the case of conventional semiconductor materials and heterostructures built upon them, the same level of control remains to be achieved for materials of the transition metal dichalcogenides (TMD) family.

The challenge in assembling one-dimensional nanostructures based on TMD materials lies in the anisotropic character of their bonding, which favours the formation of platelet-like structures when growing them using bottom-up approaches and thus limits the range of available morphological configurations. Realising the size- and morphology-controllable fabrication of 1D TMD nanomaterials would make possible several novel directions in terms of applications. Specifically, 1D TMD-based heterostructures which combine different materials would benefit from a greatly expanded portfolio of tunable properties, leading to emerging functionalities different from those found in the individual components. For instance, core-shell WO$_x$-WS$_2$ nanowires have been shown to outperform stand-alone two-dimensional TMD-based capacitors due to the interplay between the conductive WO$_x$ core and a WS$_2$ shell that favors fast ionic adsorption and transport [8]. Likewise, MoO$_x$-MoS$_2$ nanowires exhibit an enhanced HER catalytic activity compared to 2D layers of MoS$_2$, due to the interplay between the conductive MoO$_x$ core and the catalytically active MoS$_2$ shell [9, 10].

With this motivation, here we develop a novel strategy for the fabrication of metal-TMD core-shell 1D nanostructures based on the combination of top-down and bottom-up approaches, and demonstrate its feasibility for the fabrication of vertically-aligned Mo-MoS$_2$ core-shell heterostructures denoted as nanopillars (NPs). Metal-semiconductor heterostructures have been shown to represent an alternative pathway to favourable catalytic [11], optical [12], and electronic properties [13]. Our strategy builds upon the top-down fabrication approach to the Mo nanopillars described in the previous chapter, and is based on the sulfurisation of the as-prepared Mo NPs in a Chemical Vapour Deposition (CVD) setup [14, 15] leading to core-shell Mo-MoS$_2$ one-dimensional NPs.

We then employ several characterization techniques to explore their structural, electronic, and optical properties. First of all, Raman spectroscopy along with Energy Dispersive X-ray (EDX) spectroscopy in the Transmission Electron Microscope (TEM) confirms the growth of a MoS$_2$ shell on the as-fabricated Mo NPs. We then study the dependence of the formed MoS$_2$ shell as function of pillar-to-pillar distance and NP width. Subsequently, High-Resolution Transmission Electron Microscopy (HR-TEM) is used to pin down the atomic configuration of the core-shell structures, while Electron Energy Loss Spectroscopy (EELS) makes possible elucidating their local electronic behaviour and correlating it with structural features. Finally, nonlinear optical measurements are carried out, demonstrating an enhanced nonlinear optical response of the core-shell structures as compared to a reference composed by 2D MoS$_2$ flakes.

6.2. SULFURIZATION OF MO NANOPILLARS

6.2.1. SULFURIZATION PROCESS

In this work, we develop a procedure to fabricate core-shell Mo-MoS$_2$ NPs with the following design criteria in mind: (1) a metallic Mo core whose shape can be easily tailored for specific applications, (2) a MoS$_2$ shell whose size and shape can be controlled, and (3) vertical alignment of the core-shell NPs with respect to the substrate surface to provide a large amount of exposed MoS$_2$ edges.

The core-shell Mo-MoS$_2$ NPs are synthesized using a two-step chemical vapor deposition (CVD) process. We first fabricate Mo NPs as described in Chapter 5 (see Figure 6.1(a,b) for representative Mo NP arrays) and then use these Mo NPs as scaffolds for the MoS$_2$ shell growth, in a process known as sulfurization. We briefly describe here the sulfurization process, see [15] for further details. To begin with,the wafer containing the Mo NPs are placed in the middle zone of a three zone, split-tube, CVD furnace containing a quartz reaction tube, as schematically represented in Figure 6.1(c). The sulfur powder used as a precursor is placed upstream in a separate zone. The synthesis is performed at ambient pressure and argon (Ar) is used as a carrier gas. The separate zones of the CVD furnace allow us to control the temperature of the Mo-metal NPs and the sulfur precursor independently. From previous experience, we know that the growth rate of MoS$_2$ in this two-step process can be precisely controlled by adjusting the reaction temperature, reaction time and the flow rate of the Ar carrier gas. A reaction temperature of 650°C and an Ar gas flow of 150 sccm results in controllable growth of the core-shell Mo-MoS$_2$ NPs. We also discuss the effects of a reaction temperature of 750°C. We vary the reaction time for various core-shell Mo-MoS$_2$ NP synthesis experiments keeping a constant reaction temperatore of 650° for each corresponding synthesis.

The reaction tube is flushed with Ar gas for 30 minutes at 500 sccm before each synthesis to make sure that all oxygen is vacated from the system. This flow rate is maintained until the Mo NPs reach a temperature of 500°C after which the Ar gas flow is reduced down to 150 sccm. The temperature in the middle zone, containing the Mo NPs, is heated to the target temperature of 650°C at a rate of 10°C/min. Once the sample reaches the target temperature the sulfur will be heated up to 220°C, also at a rate of 10°C/min. At this moment the reaction timer is started. After the reaction time has elapsed, the entire system is naturally cooled down to room temperature, while maintaining an Ar gas flow of 150 sccm.

6.2.2. RESULTS

To illustrate the end product of the sulfurisation process, Figure 6.1(d,e) displays the resulting vertically-aligned metal-TMD Mo-MoS$_2$ NPs obtained from the sulfurisation of the Mo NPs from Figure 6.1(a,b). At a reaction temperature of 650°C and reaction time of 5 minutes, the MoS$_2$ growth tends to have the same morphology as the fabricated Mo NPs, as can be seen by comparing the top with the bottom panels of Figure 6.1. The NPs are surrounded at their base by what appears to be horizontal MoS$_2$ layers, where the size of the horizontal layer increases as the electron beam exposure during the lithography step is increased, as well as when the NP pitch is decreased.

6
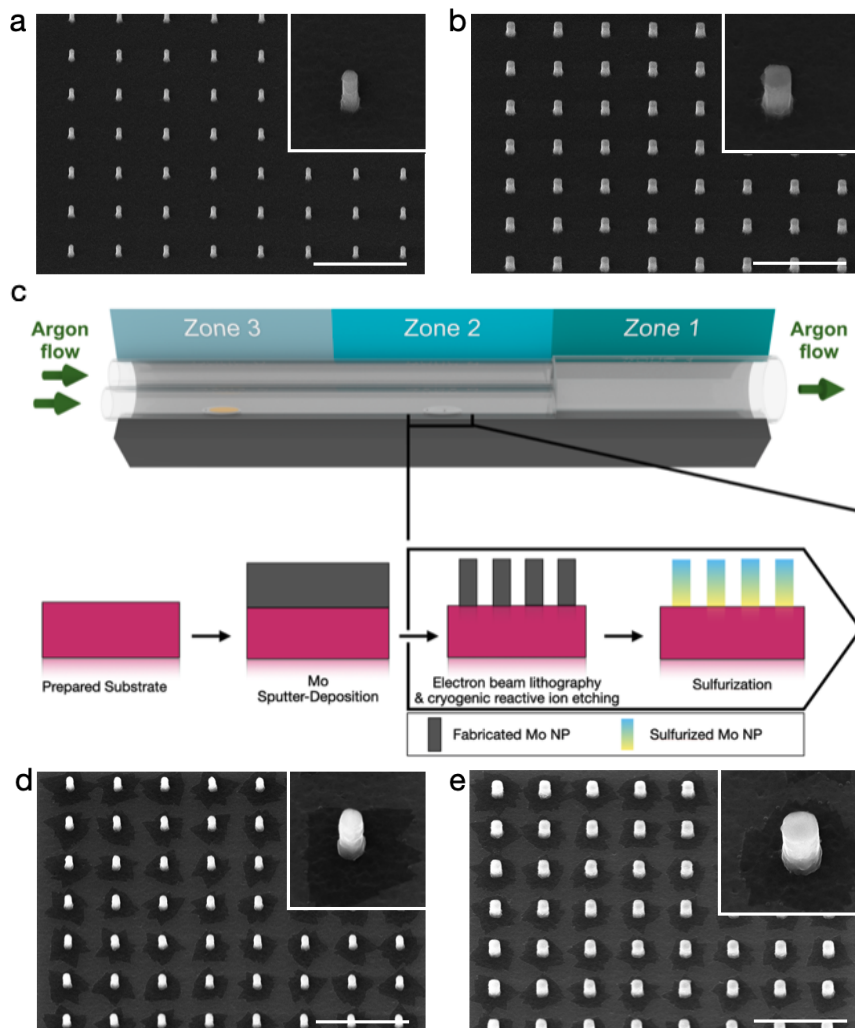
Figure 6.1: ((a,b), Scanning Electron Micrograph (SEM) of Mo NP array corresponding to 350 nm thick Mo layer before sulfurization. c, Schematic of sulfurization of Mo nanopillars, (d) Sulfurized Mo NPs corresponding to (a) and (e) sulfurized Mo NPS corresponding to (b). The scale bar is 2 μm.
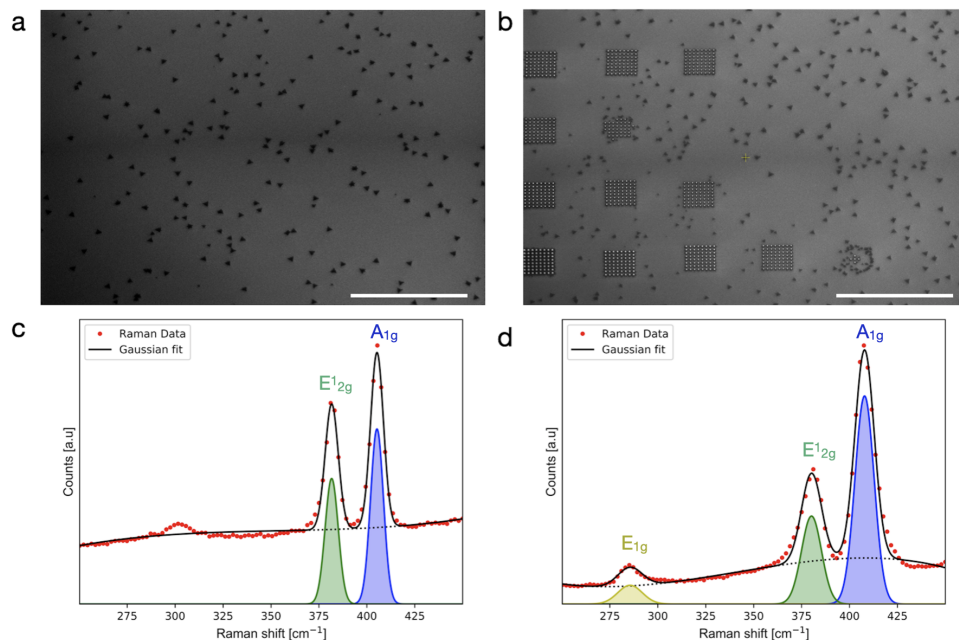
Figure 6.2: (a) SEM image of triangular MoS$_2$ flakes nearby sulfurized Mo NP arrays, and (b) overview of sulfurized Mo NPs arrays. In (a,b) the scale bar is 30 μm. Raman spectrum of (c) substrate not containing the NPs arrays and (d) representative sulfurized Mo NPs array.

The presence of MoS$_2$ on the substrate and on the NP arrays is confirmed by Raman spectroscopy measurements, as illustrated by Figure 6.2(c,d). On all arrays, we find the in-plane E$_{2g}^1$ and out-of-plane A$_{1g}$ Raman modes characteristic for trigonal prismatic (2H-MoS$_2$) crystal phase, which demonstrates the consistent MoS$_2$ growth from the fabricated Mo nanostructures. Additionally, we observe the E$_{1g}$ peak in the Raman spectra, suggesting that vertically-grown MoS$_2$ is present on the substrate. The E$_{1g}$ peak gradually disappears as we go to smaller NP diameters, which can be explained by a weaker signal due to the smaller diameters. Another indication of vertically-aligned MoS$_2$ nanosheets can be found by comparing the ratio of intensities of the E$_{2g}^1$ and A$_{1g}$ peaks. For all arrays the ratio of the intensities of the A$_{1g}$ and E$_{2g}^1$ peaks remain the same, suggesting the presence of vertically-aligned MoS$_2$ layers.

Furthermore, we find nearby the fabricated NPs the presence of triangular flakes on the substrate. Raman spectroscopy confirms that these triangular flakes are layers of MoS$_2$, where in some cases the E$_{1g}$ peak is also found, indicating thick layers of MoS$_2$ on the surface of the substrate that may have vertically-oriented layers. We suspect that a small fraction of the Mo NPs sublimate and react with the S vapour to form these structures on other parts of the substrate. Alternatively, residual Mo may be present after the cryogenic etching step. The residual Mo on the substrate surface reacts with the S vapor to form the horizontal MoS$_2$ flakes.

The consistent growth of the MoS$_2$ shell is obtained for Mo NPs corresponding to different cross-sectional geometries, a representative subset of which is displayed in Figure 6.3. In Figure 6.3(a-c) the results of the sulfurization process of Mo NPs with hexagonal, circular, and triangular cross-sections geometries is displayed for a reaction time and temperature of 5 minutes and 650°C, respectively. For these specific sulfurization conditions, one verifies that the cross-sectional shape of the original Mo template structures is preserved once the MoS$_2$ shell is incorporated. In addition we find that, for some of the sulfurized core-shell NPs, very thin protrusions are formed on their surface, such as in the case displayed in Figure 6.3(d), which could be explained as the growth of nanotubes of MoS$_2$ on the surface of the shell. Nevertheless, a detailed structural characterisation analysis is required to confirm the composition of these protrusions.

We find that the results of the sulfurisation process is strongly sensitive on the cryogenic etching conditions. Figure 6.3(e,f) illustrates the consequences of a non-optimal etching procedure. For this specific sample, during the cryogenic etching the liquid nitrogen became depleted, resulting in a significant increase in the process chamber temperature, leading to a rough etching of the Mo nanopillars. The subsequent sulfurization of the structures in Figure 6.3(e,f) at 650°C for 5 minutes resulted in ripped sulfurized nanostructures for fabricated structures with large original widths(widths before sulfurization in the 200 nm and 300 nm range), as in Figure 6.3(e). For fabricated structures with smaller widths we find NPs with poorly defined boundaries compared to a successful etching procedure, as in Figure 6.3(f).

The MoS$_2$ growth dependence on reaction temperature is briefly explored by carrying out a sulfurization process of fabricated NPs at a reaction temperature of 750°C. In Figure 6.3(g,h) Mo NPs are fabricated in a 880nm Mo layer and are subsequently sulfurized with a reaction time of 5 minutes and reaction temperature of 750°C. We observe the presence of MoS$_2$ grains on the entire surface of the substrate. The presence of MoS$_2$ on the entire substrate surface is confirmed by Raman spectroscopy to be MoS$_2$.

In thin films of Mo it has been reported that the rate of sulfurization of the Mo seed layer exponentially increases with increasing reaction temperature[15]. An exponential dependence on reaction temperature can be the cause of the bending of the sulfurized Mo NPs in Figure 6.3(g,h). We should note that the bending of the sulfurized Mo NPs can also be attributed to the high-aspect ratio of the original Mo NPs in Figure 6.3(g,h). Sulfurized Mo NPs with diameters down to 130 nm, paired with NP lengths up to 1.30 μm have been achieved. In this respect, we show that a high yield of high-aspect ratio sulfurized Mo NP is also possible, however the vertical yield of the NPs is diminished.

Finally, we note the appearance of a grainy substrate surface surrounding the sulfurized NPs, which is also found on the entire substrate surface. The grainy substrate surface can be a consequence of a higher degree of sublimation of the Mo structures caused by the higher sulfurization temperature where subsequent reaction with the sulfur vapour causes redeposition of MoS$_2$ on the substrate surface. We note that the grainy substrate surface can also be a consequence of insufficient etching of the unprotected Mo in the fabrication step.
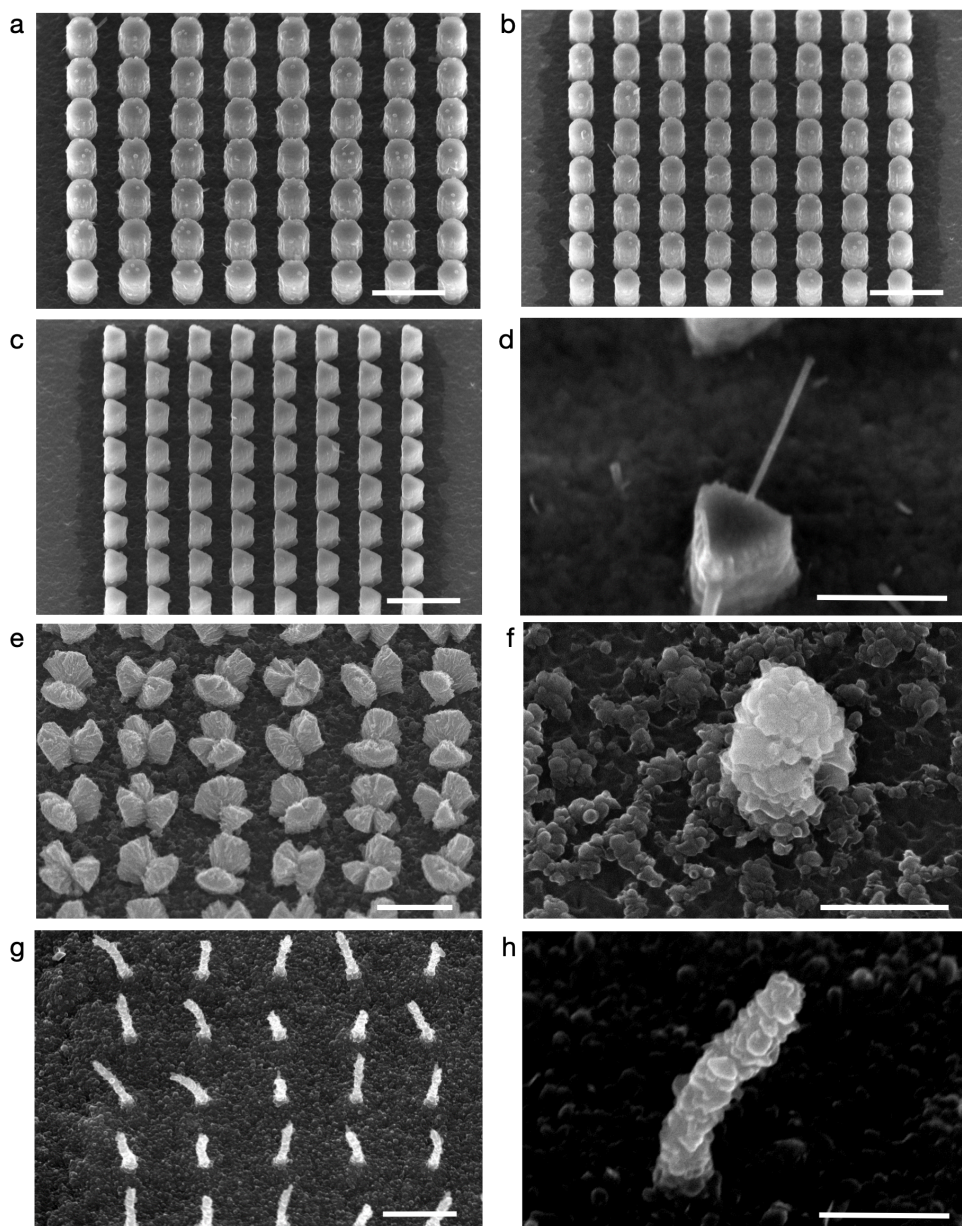
Figure 6.3: The fabricated shapes of (a) hexagonal (b) circular, (c,d) triangular structures can still be seen after sulfurization. Reaction temperature is in (a-f) 650°C, and in (g,h) 750°C. The thickness of the Mo layer used in the nanofabrication process is (a-c) 500 nm, (d) 440 nm, (e,f) 350 nm, and (g-h) 880 nm. The scale bar in (a,b,c,e) is 1μm and in (d,f,h) the scale bar is 400 nm.
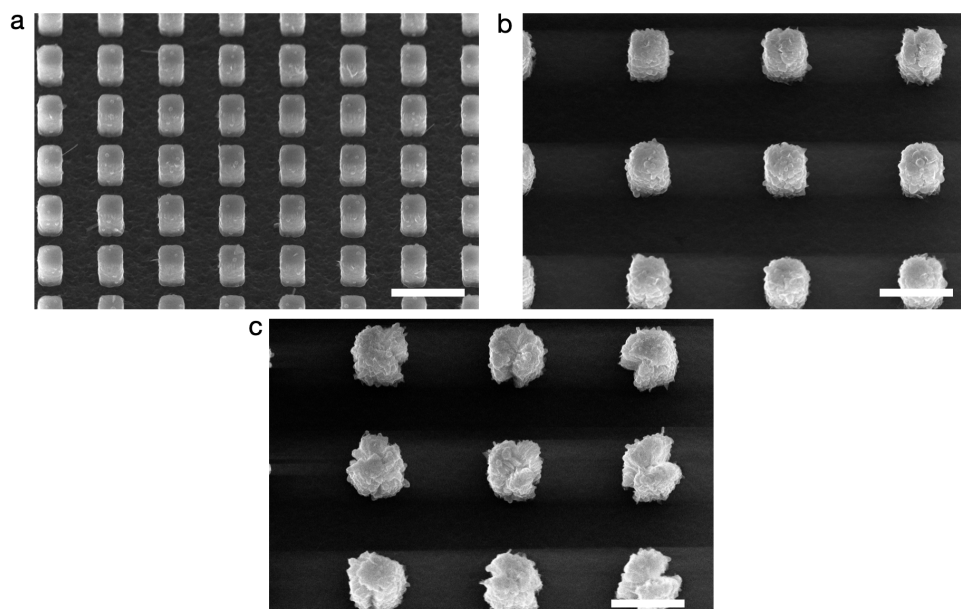
Figure 6.4: The results of the sulfurization of squared cross-section Mo NP with widths of 300 nm for three different reaction times: (a) 5 min, (b) 7.5 min, and (c) 10 min. The scale bar is 1 μm.

6.2.3. Reaction Time Dependence

From the above discussion we have seen how the reaction temperature can affect the nanofabricated structures and the underlying substrate. Namely, a high reaction temperature (750°C) leads to a high degree of MoS₂ growth on the substrate surface, and what appears to be full sulfurization of the Mo NPs. In contrast, for a reaction temperature of 650° and 5 minutes reaction time the sulfurized NPs retain the shape of the unsulfurized nanofabricated Mo NPs. It is for this reason we use for the remainder of this chapter a reaction temperature of 650°C for the subsequent sulfurization processes. We continue with studying the effects of reaction time on the nanofabricated structures. We compare sulfurized Mo NPs with the same square nanofabricated shape and with similar widths and lengths. Mo NPs were fabricated starting from a 500nm thick Mo layer. The fabricated Mo NPs were subsequently sulfurized while only varying the reaction times for the sulfurization process of the different Mo NPs substrates. Figure 6.4 displays the outcome of the sulfurization of squared cross-section Mo NPs with widths approximately 300nm for three different reaction times: 5 min, 7.5 min, and 10 min. As we increase the reaction time the sulfurized Mo NPs gradually lose their original nanofabricated shape. Furthermore, a sizeable increase in NP width is observed when the reaction time is increased. We attribute this loss of shape and increase in the width of the nanofabricated structures to a higher degree of sulfurization of the Mo metal. In the case of fabricated Mo NPs with widths in the 100nm-150nm range we see little difference between the 7.5 min and 10 min reaction times. We will later see that this is due to full sulfurization of these smaller nanofabricated NPs.
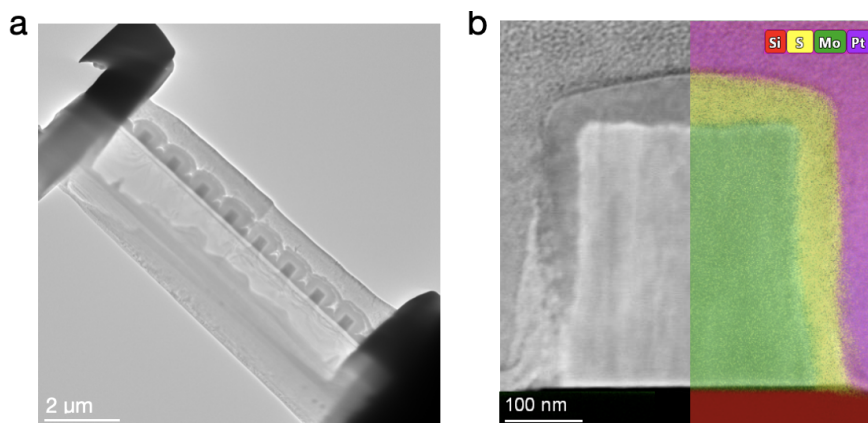
Figure 6.5: (a) Low-magnification HRTEM image of a slab of sulfurized Mo nanopillars. (b) Composition of a high-angle annular dark-field (HAADF) STEM image (left side) with the corresponding compositional EDX map (right side) associated to the cross-section of this sulfurised NPs.

6.3. STRUCTURAL ANALYSIS OF SULFURIZED MO NANOPILLARS

6.3.1. CHEMICAL COMPOSITION OF SULFURIZED MO NANOPILLARS

The core-shell structure of the sulfurized Mo NPs is confirmed using Energy-Dispersive X-ray spectroscopy in the Scanning Transmission Electron Microscope (STEM-EDX). We carry out STEM-EDX in a Titan Cube microscope operated at 300 kV to determine the specific chemical composition of the sulfurized Mo NPs. In order to prepare the sample for TEM inspection, cross-section lamellas are prepared with a focused ion beam (FIB) milling approach using a FEI Helios G4 CX focus ion beam. The ion milling procedure was carried out using a very low energy electron beam of 10 kV, and an ion beam of 18 pA. Note that a Pt protective layer is deposited on top of the NPs to avoid damage during ion beam milling. Markers are placed aligned with a row of sulfurized NPs to assist with precise milling of the lamella near the NPs of interest. Care is taken to limit the SEM exposure of the NPs during the lamella fabrication procedure, as too much SEM exposure leads to contamination visible during TEM inspection.

Figure 6.5(a) displays a low-magnification TEM image of a cross-section of sulfurized Mo NPs with a starting length of 350nm with square cross-sections corresponding to a reaction time of 5 minute. The Mo core can be seen along with a bright shell surrounding the core. Figure 6.5(b) shows a composition of an high-angle annular dark-field (HAADF) STEM image (left side) with the corresponding compositional EDX map (right side) associated to the cross-section of this core-shell nanopillars, where the latter confirms the Mo-MoS_2 nature of the core-shell configuration.
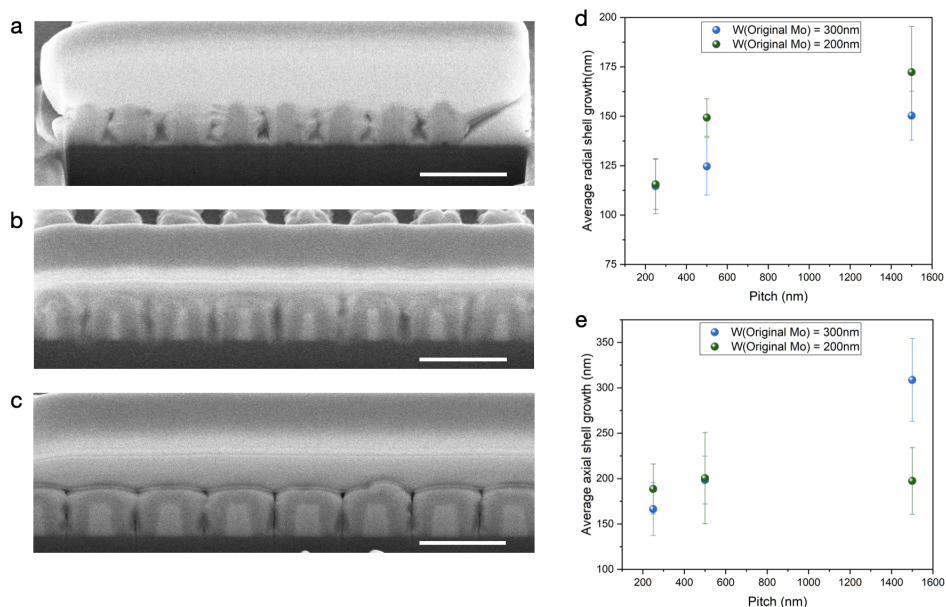
Figure 6.6: (a)-(c) SEM images of FIB cross-sections carried our for three different NP arrays. The original Mo NP widths are 100 nm (a), 200 nm (b), and 300 nm (c), the pitch for all three arrays is 500 nm, and the scale bar is 1 μm. The light (dark) contrast indicates the Mo core (MoS₂ shell). (d) and (e) Average thickness of the MoS₂ shell growth (evaluated over 10 NPs in each case) in the radial and axial directions respectively, as a function of the pitch for a fixed growth time of 7.5 min. We show results corresponding to NPs with original widths of both 200 and 300 nm. The increase in the MoS₂ shell growth as the pitch increases highlights the effect of the competitive growth-regime between nearby NPs. Error bars indicating standard deviation.

6.3.2. SHELL-PITCH DEPENDENCE

We prepare cross-sections of different arrays using focus ion beam (FIB) to determine the shell-thickness of various nanopillar widths. SEM images of FIB cross-sections performed for three different NP arrays are displayed in Figs. 6.6(a-c). The information provided by these cross-sectional SEM images is used to determine the thickness of the MoS₂ shell in the axial and radial direction for the NP arrays considered. The original Mo NP widths are 100 nm (Fig. 6.6(a)), 200 nm (Fig. 6.6(b)), and 300 nm (Fig. 6.6(c)), the pitch for all three arrays is 500 nm, and a fixed growth time of 7.5 min is adopted. Thanks to the difference in contrast, these cross-sectional SEM images reveal the Mo core and MoS₂ shell morphology of the sulfurized Mo NPs for the NPs with original Mo widths of 200 nm and specially for 300 nm, see Figs. 6.6(b) and Fig.6.6(c) respectively. By averaging over 10 NPs in each of the two arrays corresponding to Mo NPs with original widths of 200 and 300 nm, one can determine the thickness of the radial and axial MoS₂ shell growth as a function of the pitch, displayed in Figs. 6.6(d) and 6.6(e) respectively. On the one hand, the thickness of the MoS₂ shell in the radial direction appears to be larger as the pitch is increased, with the NPs with original Mo width of 200 nm exhibiting the thicker shell. One possible explanation for this trend is that the direct flux of the sulfur precursor impinging on the Mo NP sidewalls is one of the main pathways contributing
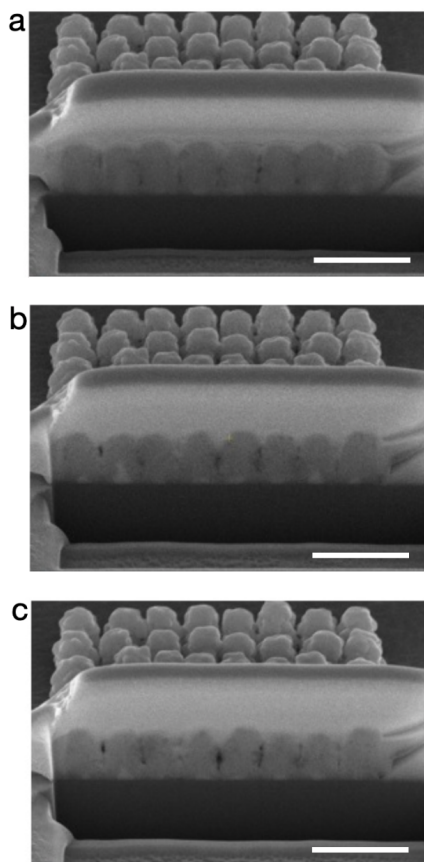
Figure 6.7: SEM images of FIB cross sections corresponding to a sulfurized Mo NP array with 150 nm starting width and reaction time of 7.5 minutes. Each of the three images displays different slices of the same row within the NP array, revealing an almost completely consumed Mo core. The scale bar is 1 μm.

to the growth of MoS$_2$. This contribution decreases when the distance between Mo NPs (pitch) is reduced due to the competition between nearby NPs. Concerning the growth of the MoS$_2$ shell along the axial direction, we observe that the thickness of the MoS$_2$ shell does not vary with the pitch of the Mo NPs for an original width of 200 nm. For the NPs with larger original width instead (300 nm), the shell thickness increases with respect to the pitch.

In the case of original Mo NP widths smaller than 150 nm (Fig. 6.6(a)), the sulfurization appears to be almost complete. Nevertheless, a closer inspection of the cross-sections taken in a sequence of milling steps (Fig. 6.7) indicate that a small metal-Mo core still remains at the central region close to the base of the NPs. Figs. 6.10(a-c) display FIB cross sectional images of a sulfurized Mo NP array with 150 nm starting diameter, where each of the three images correspond to the same row of sulfurized Mo NPs being milled

in subsequent FIB milling steps. These Mo NPs were sulfurized for 7.5 minutes. We can conclude from the difference in contrast of the SEM images that for this specific configuration the Mo core is close to being completely consumed and turned into MoS_2. However, we also note that a small metal-Mo core still remains at the central region of the NP.

6.3.3. Shell Structural Characterisation

We proceed to assess the structural properties of core-shell Mo-MoS₂ NPs. In particular, we are interested in the specific orientation of the MoS_2 layers in the shell with respect to the Mo core NP. The structural analysis in Figure 6.8 was carried out in an JEOL mono-ARM200F microscope operated at 200 kV in TEM mode. In all these images, a spot of size 3 was used, the monochromator was activated without any slit. First of all, Figure 6.8(a) displays a low-magnification bright-field HRTEM image taken on a representative core-shell NP sulfurized with a reaction time of 7.5 minutes. Figure 6.8(b-d) display the corresponding high-magnification TEM images taken at various locations at the interface between the Mo core and the MoS_2 shell: top, right side, and left side respectively. From these images one can clearly see that the MoS_2 layers grow perpendicularly with respect to the surface of the Mo core: the top region exhibits vertical MoS_2 layers (see Figure 6.8(b), while the side regions display instead MoS_2 layers with an horizontal orientation with respect to the substrate. The presence of MoS_2 layers with consistently perpendicular orientations with respect to the Mo core surface suggest that the outer boundary of the core-shell NPs contain a high density of MoS_2 edge terminations. We note that confirming the boundary composition of the core-shell NPs is not possible with the lamella cross-section technique due to the protective Pt layer deposited on top of the NPs. An alternative method to determine the precise boundary of the NPs could be to use ultrasonication of the NPs and directly depositing the solution of ultrasonicated NPs onto a TEM grid.

From Figure 6.8(b-d) one observes that in the top and side regions of the NPs the MoS_2 layers display a certain disorder in their relative orientations, while maintaining their global orientation with respect to the Mo surface. Figure 6.8(f) displays an intensity profile corresponding to a linescan acquired in the region displayed with a black square in (e), which in turn is marked as a blue square in (d). The interlayer distance is measured to be 0.64 ± 0.01 nm, consistent with previous growth of vertically-aligned MoS_2 sheets [15]. Furthermore, we have determined that the orientation of the MoS_2 layers in the shell exhibit identical structural properties irrespectively of the reaction times; in other words, the reaction time mostly dictates the amount of Mo consumed and transformed into MoS_2, and therefore the overall thickness of the shell.

6.4. Electronic and Optical Properties

6.4.1. Electron energy-loss spectroscopy Characterization

In the previous sections we discussed the structural properties of the core-shell Mo-MoS₂ NPs. We continue here with probing the electronic properties of the sulfurized NPs using spatially-resolved electron energy-loss spectroscopy in the scanning transmission electron microscope (STEM-EELS). The nature of collective excitations of the
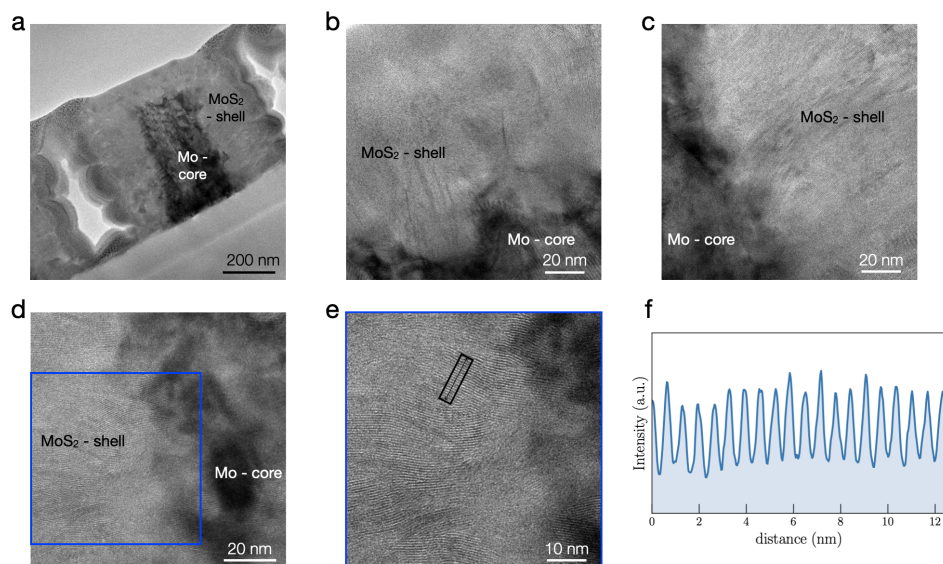
Figure 6.8: (a) Low-magnification bright-field HRTEM image of the cross-section associated to a representative core-shell Mo-MoS$_2$ NP, corresponding to a sulfurisation time of 7.5 minutes. (b,c,d) High-magnification HRTEM images taken at various locations at the interface between the Mo core and the MoS$_2$ shell: top, right side, and left side respectively. (f) Linescan of the region displayed in (e), which in turn is marked as a blue square in (d).

constituents of the core-shell NPs is investigated with spatially-resolved EELS. The electron energy-loss spectral image shown in Figure 6.9 and Figure 6.10 was also recorded in the JEOL mono-ARM200F microscope operated at 200 kV using the STEM mode. The monochromator was set up on with a slit of 0.1 μm inserted. A probe size of 6C, a CL2 aperture of 30 μm, and a camera length of 12 cm were employed. The EELS was recorded using a a Gatan GIF Continuum spectrometer with dispersion of 0.015 eV/ch, the aperture of the GIF was set to 5 mm, and the pixel time was 1.3 s. Figure 6.9 displays a spatially resolved EELS map of a core-shell NP sulfurized with a 7.5 min reaction time, where each pixel corresponds to an individual EEL spectrum comprising an area of 1nm^2. We aim to study the interplay between the Mo core and MoS$_2$ shell and so the regions of interest are 1) the Mo core (1-2), 2) the Mo-MoS$_2$ interface (3-4), and 3) the MoS$_2$ shell (5-6), which can be seen in Figure 6.9(c). In order to increase the signal-to-noise ratio Figure 6.9 we analyze the EEL spectra of the regions of interest by taking the average EEL spectra of squares of 5x5 pixels in order to increase the signal-to-noise ratio.

Averaged EEL spectra corresponding to the regions of interest described above can be seen in Figure 6.9b. We start with the MoS$_2$ shell, given by spectra sp5 and sp6. In both sp5 and sp6 a peak is found at 22.48 eV, which can be attributed to the bulk plasmon peak of MoS$_2$ [16–20]. Furthermore, a feature located at around 8 eV is also observed in the MoS$_2$ shell, which is similar to the π-character interlayer excitations of the electrons that are not involved in ionic-covalent bonding [19, 20]. The presence of interlayer exci-
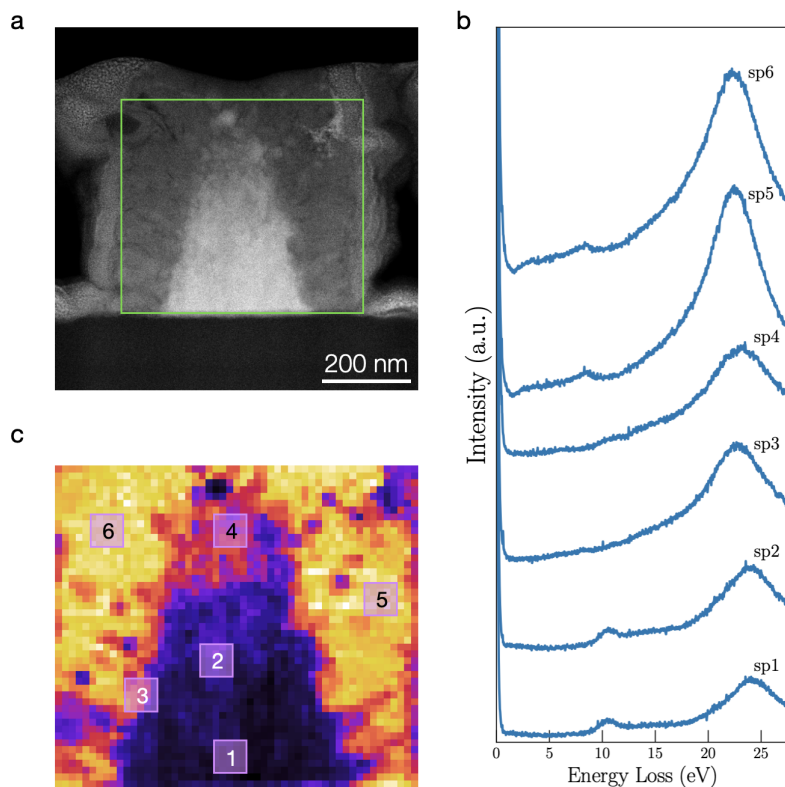
Figure 6.9: Core-shell Mo-MoS$_2$ NPs synthesized with a reaction time of 7.5 minutes with (a) low-magnification image showing the region of interest with the green outline indicating the boundaries for the EELS map. (c) An area of 5x5 pixels in the spectral map is taken to improve the signal to noise ratio. The different areas (1-6) are chosen such that we have the contributions mainly from the Mo core(1-2), from the shell(5-6), and in the interface region(3-4). (b) EEL spectra corresponding to the averaged areas denoted in (c)

tations should only be possible if the electron beam is perpendicular to the MoS$_2$ layers. The interlayer excitations can be due to the horizontal layers of the different facets of the NPs curving slightly upwards. The behaviour of the Mo core is given by the averaged spectra sp1 and sp2. There are two main peaks present in the Mo core, a large peak located at 24.0 eV and a smaller peak located at 10.3 eV. Both peaks in sp1 and sp2 can be attributed to the two bulk plasmon peaks found in metallic Mo [21]. The interface region, given by spectra sp3 and sp4, we see a large peak located between the bulk plasmon peak of MoS$_2$ and the bulk plasmon peak of Mo located at 24 eV. It is possible that the peak at 24.0 eV is a consequence of the averaging of the 5 × 5 pixels that is being used here, leading to overlapping of the bulk plasmons peaks of the core and shell. In order to properly disentangle the contributions from the core and shell and have sufficient signal-to-noise ratio we average over 3x3 pixels, the results of which can be seen in Figure 6.10.
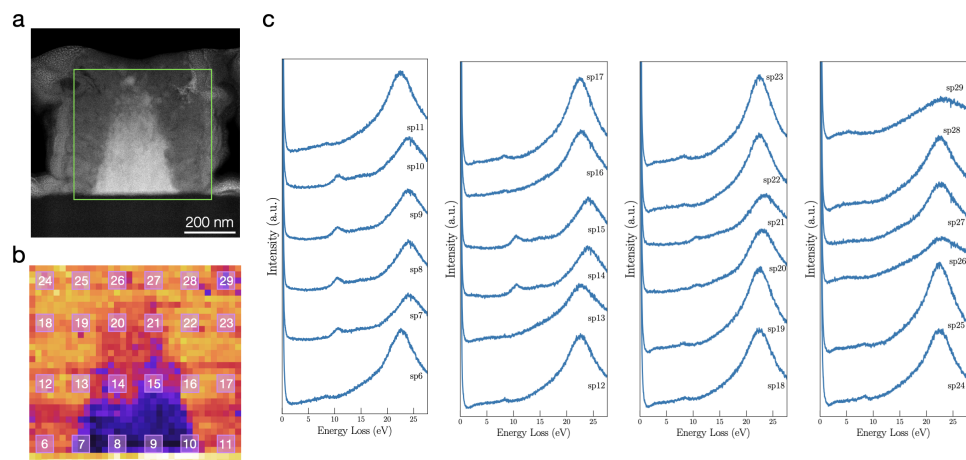
Figure 6.10: Core-shell Mo-MoS$_2$ NPs synthesized with a reaction time of 7.5 minutes with (a) low-magnification image displaying the region of interest for the EELS map. (b) Positions of the averaged(3x3 pixels) EEL spectra which are taken in regular spatial intervals, with (c) the corresponding averaged EEL spectra.

The averaged spectra are taken in regular spatial intervals across the spectral image, where all the regions(core, shell, interface) of interest are taken into account. Inspection of the spectral image in Figure 6.10 reveals the presence of the bulk plasmon peaks already found in Figure 6.9 for the Mo core and MoS$_2$ shell. Additionally, we do not find the peak at 24.0 eV for the averaged EEL spectra at the Mo-MoS$_2$ interfaces, suggesting that the large peak found in sp3 and sp4 in Figure 6.9 is a result of the larger averaging area at the interface of the Mo-MoS$_2$.

6.4.2. NON-LINEAR OPTICAL BEHAVIOUR

We next study the nonlinear response of the core-shell NPs by using two different color ultrashort laser pulses. These two pulses have wavelengths of 775 nm and 1200 nm respectively and a pulse duration of around 150 fs for both pulses with a 80 MHz repetition rate. The average power of the laser pulses is set to 3.8 mW and 3.6 mW for the 1200 nm and 775 nm pulse respectively. Both laser pulses are focused onto the sample and are spatially and temporally overlapped to generate the nonlinear signals. The spectra of the nonlinear signals are measured using a high sensitivity spectrometer. The laser pulses were generated by a femtosecond laser oscillator (Tsunami, Spectra-Physics) and an optical parametric oscillator (OPAL, Spectra-Physics). Both laser beams were focused onto the sample using a microscope objective (Olympus UP-LSAPO 40×/0.95), which also collects the emitted light originated through the nonlinear laser-NPs interaction. The collected light was filtered and imaged onto the slit of a spectrometer (PI, Spectra Pro 2300I).

In Figure 6.11 the nonlinear optical response of a representative NP array is presented. Five peaks are visible which can attributed to second-harmonic generation (SHG) where,
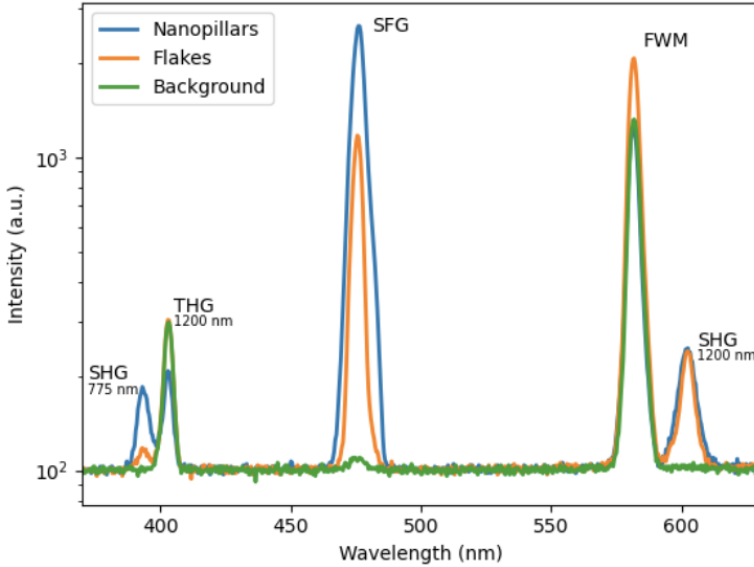
Figure 6.11: Nonlinear response of triangular NP arrays with 75 nm diameter and 350 nm length. Comparison with nearby MoS$_2$ flakes and Si substrate background can be seen.

$\omega_{SHG} = 2\omega_{1200}$ and $\omega_{SHG} = 2\omega_{775}$, third-harmonic generation (THG), where $\omega_{THG} = 3\omega_{1200}$, sum-frequency generation (SFG) where, $\omega_{SFG} = \omega_{775} + \omega_{1200}$ and four-wave mixing (FWM) where $\omega_{FWM} = 2\omega_{775} - \omega_{1200}$.

In addition to the nonlinear spectra acquired on the Mo-MoS$_2$ NPs, we also display the corresponding nonlinear spectra taken on the substrate material (Si/SiO$_2$) as well as on the nearby located MoS$_2$ flakes, which provide a reference for the same material under a different configuration. It can be observed that the third-order nonlinear signals (FWM, THG) are similar for the background and NPs. The THG nonlinear signal is even slightly reduced with respect to the background. However, the second order processes (SHG, SFG) are highly enhanced in the MoS$_2$. Indeed, the NP array, compared with the horizontally-oriented MoS$_2$ flakes of reference, benefits from the emission of even larger nonlinear signals for the SHG$_{775\ nm}$ and the SFG.

In order to explore the origin of nonlinear signals from the NP array, we perform a raster scan over the nanopillar array. Figure 6.12 shows a false color map of the intensities of the SFG (left), SHG (middle) and THG (right) nonlinear signals around the nanopillar array. Although different NPs can be distinguished from the second order nonlinear signals, the nonlinear intensities of the individual NPs differ. This could potentially be explained by slightly different orientations or angles of the NPs. There also appears to be nonlinear signal generated in between the NPs and this is most likely originated from horizontally oriented flakes in between the NPs that can be seen in the SEM images in Figure 6.2.
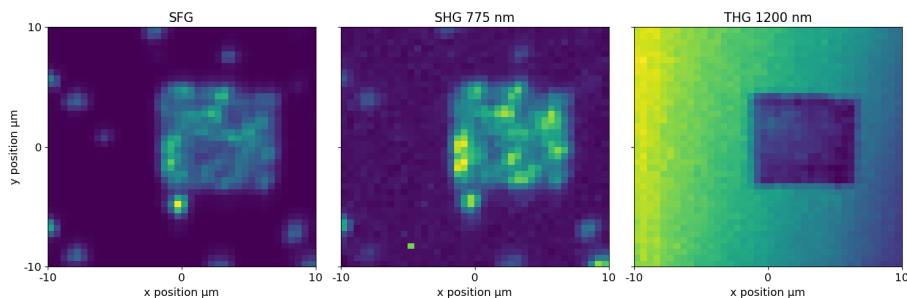
Figure 6.12: Raster scan of the triangular core-shell MoS_2 NP arrays corresponding to the spectrum in Figure 6.11. A clear signal from the SFG and SHG is found in the NP array area, while the THG_{1200nm} signal of the substrate is substantially higher than that of the NP arrays.

6.5. TOWARDS SULFURIZED W NANOPILLARS

In this chapter we have demonstrated the fabrication and synthesis of core-shell Mo-MoS_2 NPs with a combination of top-down and bottom-up approaches. One can imagine extending this methodology to create NP structures of different TMDs. In this respect, we report here on attempts to fabricate W NPs with the goal to further use these W NPs as a template for the synthesis of WS_2 based NPs. We use a fabrication and etching recipe for the W NP fabrication similar to the one for Mo NPs arrays. In Figure 6.13 the results of one such attempt can be seen. In Figure 6.13(a), and Figure 6.13(b) an array of W NPs before and after sulfurization can be seen, respectively. In the case of W NPs we observer significant tapering at the base of the NPs after patterning and cryogenic reactive ion etching. Tapering is found for all NP widths. One reason for the large degree of tapering for the W NPs can be the use of RF sputter-deposition for the W layer instead of using DC sputtering. Another possibility lies in the use of high power(70W) for the reactive ion etching; The W etch rate is slightly higher than for Mo using the same etch parameters. In the case of Mo etching, it was found that lowering the power to 30W leads to consistent fabrication of NPs with sub-100nm widths. We suspect that this is due to a lower degree of backscattering on the surface of the substrate of the ions during the dry etching. It remains to be seen if a lower etch power is needed to fabricate smooth sidewalls of W NPs, or whether other etch parameters should be varied.

We continue with the sulfurization of the fabricated W NPs. Similar sulfurization parameters are used for the W NPs compared to what was used for the Mo nanostructures. The sulfurization process of the as fabricated W NPs results in all the the sulfurized NPs having an ill-defined shape. W NPs with diameters in the 150 nm range tend to be ripped apart after sulfurization. Smaller widths for the original W NPs lead to a single sulfurized W NP, however with an ill-defined shape. One possible reason for the ill-defined shapes of the sulfurized W NPs can be the less than optimal fabrication results for the W NPs. Another possible reason is a high sulfurization rate for the W NPs, leading to very little control of the growth mechanism for the W nanostructures. For the fabrication and synthesis of WS_2 NPs further research is still needed to acquire precise control of fabricated and synthesized structures.
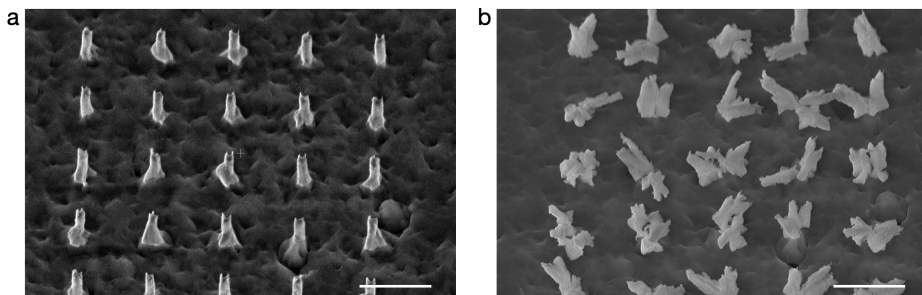
Figure 6.13: SEM images of W nanopillars before (a) and after (b) sulfurization. Both scale bars are 1 μm. The original widths for the W NPs are around 150 nm.

6.6. CONCLUSION & OUTLOOK

In this chapter we have shown how fabricated Mo NPs can be used as a template to synthesize core-shell Mo-MoS$_2$ nanopillars. The formation of the MoS$_2$ shell can be precisely controlled using a reaction temperature of 650° and by varying the reaction time. The shell of MoS$_2$ grows vertically with respect to the Mo core, leading to a mixture of vertically and horizontally oriented MoS$_2$ layers in the shell with respect to the substrate surface. This suggests that the amount of exposed edge structures of the MoS$_2$ layers can be reliably controlled by, first of all, varying the NP diameter and length in the fabrication step, and secondly, by adjusting the reaction time of the sulfurization.

The electronic structure between the Mo core and MoS$_2$ shell was studied using STEM-EELS. We found that the Mo core maintains its metallic character due to the appearance of the two bulk plasmon peaks associated with pure Mo. We also found features associated with the bulk plasmon peak and interlayer excitations associated with MoS$_2$ in the shell of the NPs. The EEL spectra indicate a sharp distinction between the Mo plasmonic activity and the MoS$_2$ plasmonic activity.

Additionally, we have found a nonlinear optical response of the core-shell Mo-MoS-2 NPs. By comparing the nonlinear response of the NPs with the nonlinear response of flakes near the NP arrays we see a clear difference in the intensity of the nonlinear response, where a larger nonlinear response is found for the core-shell NPs for second harmonic generation of 775 nm light, and sum-frequency generation. Further work is needed to determine the degree of tunability of the nonlinear optical response of the core-shell NPs with respect to shell size, widths, shapes, and pitch.

In previous studies of core-shell MoO$_x$-MoS$_2$ nanowires, several authors demonstrated favourable HER [9, 10, 22, 23] compared to monolayer flakes. They attributed the HER to the combination of the catalytically active MoS$_2$ shell and the conductive MoO$_x$. In their experiments, MoS$_2$ shells were synthesized with the basal planes parallel to the MoO$_x$ core. In this respect, the core-shell nanostructures developed in this work are promising candidates for HER experiments; advantageous catalytic activity can be supported due the large amount of exposed edges, such is found at the boundaries of the core-shell NPs in this work.

REFERENCES

[1] P. K. Sahoo, R. Janissen, M. P. Monteiro, A. Cavalli, D. M. Murillo, M. V. Merfa, C. L. Cesar, H. F. Carvalho, A. A. de Souza, E. P. A. M. Bakkers, and M. A. Cotta, *Nanowire Arrays as Cell Force Sensors To Investigate Adhesin-Enhanced Holdfast of Single Cell Bacteria and Biofilm Stability,* Nano Letters **16**, 4656 (2016), pMID: 27336224, https://doi.org/10.1021/acs.nanolett.6b01998 .

[2] V. Gautam, S. Naureen, N. Shahid, Q. Gao, Y. Wang, D. Nisbet, C. Jagadish, and V. R. Daria, *Engineering Highly Interconnected Neuronal Networks on Nanowire Scaffolds,* Nano Letters **17**, 3369 (2017), pMID: 28437614, https://doi.org/10.1021/acs.nanolett.6b05288 .

[3] D. J. Carrad, A. B. Mostert, A. R. Ullah, A. M. Burke, H. J. Joyce, H. H. Tan, C. Jagadish, P. Krogstrup, J. Nygård, P. Meredith, and A. P. Micolich, *Hybrid Nanowire Ion-to-Electron Transducers for Integrated Bioelectronic Circuitry,* Nano Letters **17**, 827 (2017), pMID: 28002672, https://doi.org/10.1021/acs.nanolett.6b04075 .

[4] J. Zhou, S. Deng, L. Gong, Y. Ding, J. Chen, J. Huang, J. Chen, N. Xu, and Z. L. Wang, *Growth of Large-Area Aligned Molybdenum Nanowires by High Temperature Chemical Vapor Deposition: Synthesis, Growth Mechanism, and Device Application,* The Journal of Physical Chemistry B **110**, 10296 (2006), pMID: 16722732, https://doi.org/10.1021/jp061213z .

[5] M. P. Zach, K. H. Ng, and R. M. Penner, *Molybdenum Nanowires by Electrodeposition,* Science **290**, 2120 (2000), https://science.sciencemag.org/content/290/5499/2120.full.pdf .

[6] Y. Bi and J. Ye, *In situ oxidation synthesis of Ag/AgCl core-shell nanowires and their photocatalytic properties,* Chem. Commun. , 6551 (2009).

[7] P. Chen, T. Zhou, M. Chen, Y. Tong, N. Zhang, X. Peng, W. Chu, X. Wu, C. Wu, and Y. Xie, *Enhanced Catalytic Activity in Nitrogen-Anion Modified Metallic Cobalt Disulfide Porous Nanowire Arrays for Hydrogen Evolution,* ACS Catalysis **7**, 7405 (2017), https://doi.org/10.1021/acscatal.7b02218 .

[8] N. Choudhary, C. Li, H.-S. Chung, J. Moore, J. Thomas, and Y. Jung, *High-Performance One-Body Core/Shell Nanowire Supercapacitor Enabled by Conformal Growth of Capacitive 2D WS_2 Layers,* ACS Nano **10**, 10726 (2016), pMID: 27732778, https://doi.org/10.1021/acsnano.6b06111 .

[9] Z. Chen, D. Cummins, B. N. Reinecke, E. Clark, M. K. Sunkara, and T. F. Jaramillo, *Core-shell MoO_3-MoS_2 Nanowires for Hydrogen Evolution: A Functional Design for Electrocatalytic Materials,* Nano Letters **11**, 4168 (2011), pMID: 21894935, https://doi.org/10.1021/nl2020476 .

[10] D. R. Cummins, U. Martinez, R. Kappera, D. Voiry, A. Martinez-Garcia, J. Jasinski, D. Kelly, M. Chhowalla, A. D. Mohite, M. K. Sunkara, and G. Gupta, *Catalytic Activity in Lithium-Treated Core-Shell MoO_x/MoS_2 Nanowires,* The Journal of Physical Chemistry C **119**, 22908 (2015), https://doi.org/10.1021/acs.jpcc.5b05640 .

6

[11] S. K. Dutta, S. K. Mehetor, and N. Pradhan, *Metal Semiconductor Heterostructures for Photocatalytic Conversion of Light Energy,* The Journal of Physical Chemistry Letters **6**, 936 (2015), pMID: 26262849, https://doi.org/10.1021/acs.jpclett.5b00113 .

[12] Y. Liu, H. Ma, X. X. Han, and B. Zhao, *Metal-semiconductor heterostructures for surface-enhanced raman scattering: synergistic contribution of plasmons and charge transfer,* Mater. Horiz. **8**, 370 (2021).

[13] J. Tan, S. Li, B. Liu, and H.-M. Cheng, *Structure, Preparation, and Applications of 2D Material-Based Metal-Semiconductor Heterostructures,* Small Structures **2**, 2000093 (2021), https://onlinelibrary.wiley.com/doi/pdf/10.1002/sstr.202000093 .

[14] D. Kong, H. Wang, J. J. Cha, M. Pasta, K. J. Koski, J. Yao, and Y. Cui, *Synthesis of MoS$_2$ and MoSe$_2$ Films with Vertically Aligned Layers,* Nano Letters **13**, 1341 (2013), pMID: 23387444, https://doi.org/10.1021/nl400258t .

[15] M. Bolhuis, J. Hernandez-Rueda, S. E. van Heijst, M. Tinoco Rivas, L. Kuipers, and S. Conesa-Boj, *Vertically-oriented MoS$_2$ nanosheets for nonlinear optical devices,* Nanoscale **12**, 10491 (2020).

[16] M. Tinoco, L. Maduro, and S. Conesa-Boj, *Metallic edge states in zig-zag vertically-oriented MoS$_2$ nanowalls,* Scientific Reports **9**, 15602 (2019).

[17] B. Yue, F. Hong, K.-D. Tsuei, N. Hiraoka, Y.-H. Wu, V. M. Silkin, B. Chen, and H.-k. Mao, *High-energy electronic excitations in a bulk* MoS$_2$ *single crystal,* Phys. Rev. B **96**, 125118 (2017).

[18] L. Martin, R. Mamy, A. Couget, and C. Raisin, *Optical Properties and Collective Excitations in MoS$_2$ and NbSe$_2$ in the 1.7 to 30 eV Range,* physica status solidi (b) **58**, 623 (1973), https://onlinelibrary.wiley.com/doi/pdf/10.1002/pssb.2220580223 .

[19] K. Zeppenfeld, *Electron energy losses and optical anisotropy of MoS$_2$ single crystals,* Optics Communications **1**, 377 (1970).

[20] W. Y. Liang and S. L. Cundy, *Electron energy loss studies of the transition metal dichalcogenides,* The Philosophical Magazine: A Journal of Theoretical Experimental and Applied Physics **19**, 1031 (1969), https://doi.org/10.1080/14786436908225867 .

[21] J. H. Weaver, D. W. Lynch, and C. G. Olson, *Optical properties of V, Ta, and Mo from 0.1 to 35 eV,* Phys. Rev. B **10**, 501 (1974).

[22] X. Xia, J. Tu, Y. Zhang, X. Wang, C. Gu, X.-b. Zhao, and H. J. Fan, *High-Quality Metal Oxide Core/Shell Nanowire Arrays on Conductive Substrates for Electrochemical Energy Storage,* ACS Nano **6**, 5531 (2012), pMID: 22545560, https://doi.org/10.1021/nn301454q .

6

[23] D. R. Cummins, U. Martinez, A. Sherehiy, R. Kappera, A. Martinez-Garcia, R. K. Schulze, J. Jasinski, J. Zhang, R. K. Gupta, J. Lou, M. Chhowalla, G. Sumanasekera, A. D. Mohite, M. K. Sunkara, and G. Gupta, *Efficient hydrogen evolution in transition metal dichalcogenides via a simple one-step hydrazine reaction,* Nature Communications **7**, 11857 (2016).

6

7

DISENTANGLING ELECTRONIC AND OPTICAL PROPERTIES OF WS$_2$ POLYTYPES WITH *ab-initio* CALCULATIONS

This work aims to elucidate the crystal-structure dependence of the electronic and optical properties of the 2H and 3R polytypes of WS$_2$, as well as of its 2H-3R polytype, by means of an extensive ab-initio study based on Density Functional Theory (DFT) methods. The one-particle Green's function (GW approximation) is computed in DFT and used to accurately predict the band gaps of the different polytypes of WS$_2$. Furthermore, we calculate the optical response of the WS$_2$ polytypes in terms of its energy loss function (ELF) and compare our predictions with experimental measurements of electron energy loss spectroscopy (EELS) on the same WS$_2$ polytypes. By studying the density of states, the joint density of states, and the band structure of these different polytypes, we are able to provide a theoretical assessment of the underlying origin of the different features observed in the low-loss region of EEL spectra taken on WS$_2$ nanostructures.

7.1. INTRODUCTION

M Aterials of the transition metal dichalcogenide (TMD) family have attracted ample interest due to the wide range of tunability of their electronic and optical properties [1–6]. This flexibility in tailoring the physical properties of TMD materials can be attributed to their marked sensitivity with respect to their dimensionality [7, 8], specific edge configurations [9–11], and stacking sequence [12–15].

The most common stacking sequences present in TMD materials are the 2H and 3R stacking sequences. In addition, mixed stacking sequences of the 2H and 3R crystal phases, termed polytypism, have been observed in MoS_2 [16] and $MoSe_2$ [17]. Recently, the observation of 2H-3R polytypism in WS_2 has been reported [18, 19]. There, the plasmonic and electronic implications of 2H-3R polytypism were studied by means of a combination of transmission electron microscopy (TEM) measurements and data processing with machine learning (ML), where deep neural networks make possible an efficient subtraction of the zero-loss peak background and the determination of the underlying bandgap value.

In this context, it is important to disentangle how the optical and electronic properties of the materials of the TMD family differ between either the 2H and 3R crystal phases and the mixed 2H-3R polytypism. With this motivation, this chapter will focus on pinning down the crystallographic dependence of the electronic and optical properties of bulk WS_2 for these three stacking sequences from a theoretical perspective. Specifically, we will be carrying out *ab initio* calculations based on different WS_2 crystal structure configurations by means of Density Functional Theory (DFT) [20, 21] using the `WIEN2k` software package [22, 23].

7

Furthermore, in order to obtain accurate estimates of the band gap associated to the different polytypes of WS_2, we will use the GW approximation as implemented in the GAP2 code by Jiang *et al.* [24, 25]. To this purpose, the outputs of the `WIEN2k` DFT calculations are used as input for the GW calculations in the GAP2 code. With this combination of the DFT and GW calculations we are able to evaluate the density of states (DOS), the band structure, the joint density of states (JDOS), and the energy loss function (ELF) for the three polytypes of WS_2. This information, in turn, makes possible disentangling the dependence of the electronic and optical behaviour of the WS_2 polytypes on the underlying crystal structure.

We start by defining the crystal structures of interest for this work. We continue with describing the calculational details concerning the geometry optimization, DOS, band structure, JDOS, and ELF for the different polytypes with the acquired wavefunctions and energies. In the final section, we discuss the main results of our theoretical calculations and compare them with experimental measurements acquired on WS_2 nanostructures exhibiting the same crystalline structure.
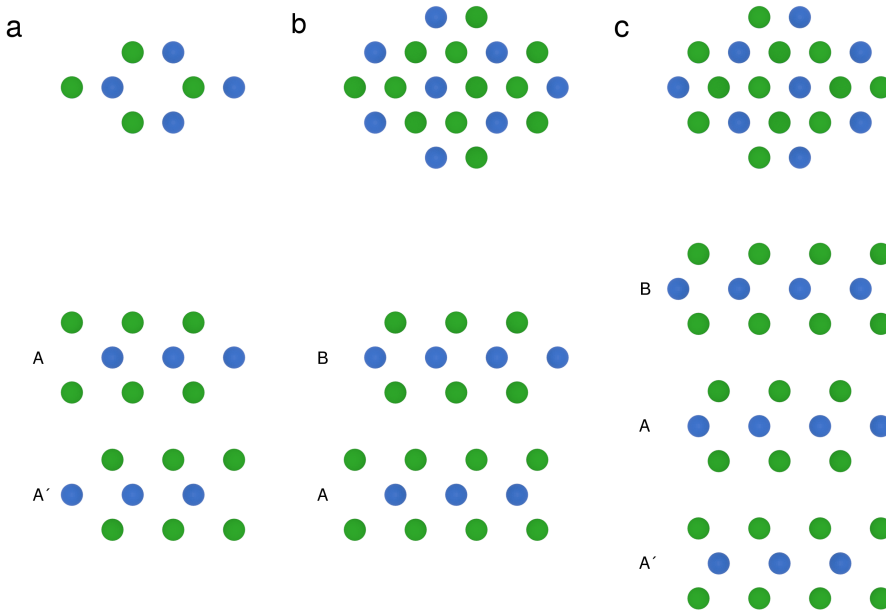
Figure 7.1: The different polytypes of WS2. In the top panels, it is shown how all three polytypes exhibit a hexagonal structures when viewed from the [0001] direction; (a) the 2H crystal phase exhibits a honeycomb lattice, while the (b) 3R and (c) 2H-3R polytypes both have an atom in the middle of their honeycomb structures. The stacking sequences of the 2H, 3R and their mixed 2H-3R polytypes can be better assessed when viewed from a lateral viewpoint with respect to the layers, as illustrated in the bottom panels.

7

7.2. ATOMIC MODELS

We start by first defining the atomic models of the different WS_2 polytypes that are being considered in this study. The DFT calculations presented in this work are based on the structural atomic models displayed in Figure 7.1. Figure 3.1(a) and (b) display the atomic model of the 2H and 3R polytypes, respectively. The 2H polytype exhibits the characteristic hexagonal stacking order (AA'), where the adjacent layers are rotated 180° and stacked directly upon one another. The 3R polytype is characterized by the rhombohedral stacking order (BA), in which the adjacent layers are slightly displaced from each other without any rotation. Figure 7.1(c) shows the atomic model of the mixed 2H-3R WS2 polytypes, which is characterized by a layer stacking order of the type BAA'. This stacking order arises from the mixture of the 2H (AA') and 3R (BA) polytypes [26].

7.3. COMPUTATIONAL DETAILS

7.3.1. GEOMETRY OPTIMIZATION

In this work we present two sets of calculations, one set of results will be on the DFT level, while the other set will be on the GW level. For each level of calculation and for each crystal lattice a specific amount of k-point sampling is used until convergence has been achieved with respect to the k-points. The k-points sampling of the first Brillouin

zone for the lattice parameter calculations and all subsequent calculations are carried out using the tetrahedon method of Blöchl et al. [27]. Geometry optimization is carried out using the literature values for lattice parameters of the 2H and 3R polytypes of WS_2 as a starting point. For the 2H-3R polytypism, we use the literature values of the lattice parameters of the 3R structure as a starting point for the geometry optimization.

The calculations on the DFT level are carried out using the linearized augmented plane wave (LAPW) and local orbitals (LO) methods implemented in the WIEN2k package. For all the crystal structures the following calculation parameters were kept the same. The nonlocal van der Waals [28, 29](vdW) interactions used for the DOS calculations uses optB88 [30] for the exchange term, the local density approximation [31] (LDA) for the correlation term, and the DRSLL kernel for the non-local term [32]. For the non-local vdW integration the cut-off density r_c was set to 0.3 bohr^{-3}, while the plane wave expansion cut-off G_{max} was set to 20 bohr^{-1}. No spin polarization was considered.

The lattice parameters were found by volume and force optimization of the different unit cells, such that the force on each atom was less than 1.0 mRy/bohr. The total energy convergence criteria was set to be 0.1 mRy between self-consistent field (SCF) cycles, while the charge convergence criteria was set to $0.001e$, with e the elementary unit charge. The core and valence electron states were separated by an energy gap of 6.0 Ry. Furthermore, the calculations used an Rk_{max} of 7.0, where R is the radius of the smallest Muffin Tin sphere, and k_{max} is the largest k-vector.

7.3.2. ENERGY LOSS FUNCTION & JOINT DENSITY OF STATES

The joint density of states and energy loss function $\Gamma_{ELF}(E)$ are calculated with the optic package as implemented in WIEN2k and is used to compare experimental EELS measurements [33–35]. The optic package calculates the optical properties in the Random Phase Approximation (RPA), neglecting local field effects. The joint density of states and the imaginary part of the dielectric function $\epsilon(E)$ are calculated by the program joint. Afterwards, the real part of the dielectric function is calculated using the Kramers-Kronig relations. The energy loss function is subsequently calculated using the relation

$$\Gamma_{ELF}(E) = \text{Im}\left(\frac{-1}{\epsilon(\omega)}\right) \tag{7.1}$$

7.3.3. SPIN-ORBIT COUPLING

Spin-orbit coupling is included after the geometry optimization in a one-shot calculation for the DOS, band structure, and ELF calculations. The spin-orbit coupling is included by using scalar-relativistic wavefunctions in a second-variational procedure [36, 37]. We ensure that enough eigenstates are included in the calculations including spin-orbit coupling by increasing EMAX in case.in1 to 7.5 Ry. Well-converged k-meshes are used for each lattice structure when calculating the DOS, band structure, and ELF and can be found in Table 7.2. For each lattice structure we used the same k-mesh for the DOS, band structure, and ELF for each level of calculation(DFT or GW level).

7.3.4. GW APPROXIMATION

After geometry optimization, the equilibrium lattice parameters obtained are used for the GW approximation calculations as implemented in the GAP2 code[24, 25]. There, the Green's function G and the screened Coulomb interaction W are calculated in the RPA framework. For the 2H and mixed 2H-3R crystal phases, we use a $6 \times 6 \times 1$ k-mesh sampling of the Brillouin zone, while a $4 \times 4 \times 4$ k-mesh sampling is used instead for the 3R crystal phase case. Fourier interpolation is used to interpolate a fine k-mesh from the sparse-mesh originally used in the GW calculations to obtain quasiparticle energies[38]. Spin-orbit coupling effects are taken into account in a perturbative one-shot manner. Table 7.2 displays the values of the k-mesh used for the GW calculation and for the calculation of the DOS, band structure, and ELF. These k-meshes are kept the same for the calculations with and without spin-orbit coupling.

7.4. RESULTS

We are now ready to present the main results of this theoretical study of the electronic and optical properties of the WS$_2$ polytypes. First, we present our determination of the density of states and band structure on these materials. Then we evaluate the energy loss function and the corresponding density of states. Finally, we provide a comparison with experimental results based on measurements taken on WS$_2$ nanostructures exhibiting the same polytypes.

7.4.1. GEOMETRY OPTIMIZATION

Geometry optimization is carried out to find the equilibrium lattice parameters of the different polytypes for the subsequent calculations. Convergence with respect to the amount of k-points is obtained for all the polytypes, and the corresponding numerical values obtained are reported Table 7.1. There, we also compare the calculated lattice parameters of the 2H and 3R polytypes with the literature values, finding good agreement. In the case of the 2H-3R polytypism, the in-plane and out-of-plane lattice parameters are found to be similar to the 3R polytype. Using the symmetry package in WIEN2k, we can identify that the 2H-3R polytypism belongs to the P3m1 space group.

Crystal Phase	Geometry Optimization	Calculated Lattice Parameters	Experimental Measurements
2H-3R	24 x 24 x 3	a = b = 3.205 Å, c = 19.057 Å	–
2H	16 x 16 x 3	a = b = 3.194 Å, c = 12.458 Å	a = b = 3.153 Å, c = 12.323 Å
3R	14 x 14 x 14	a = b = 3.199 Å, c = 18.733 Å	a = b = 3.158 Å, c = 18.490 Å

Table 7.1: k-mesh used for the calculations and crystal structures. We also display, for each WS$_2$ polytype, the calculated lattice parameters with the corresponding experimental values from [39].
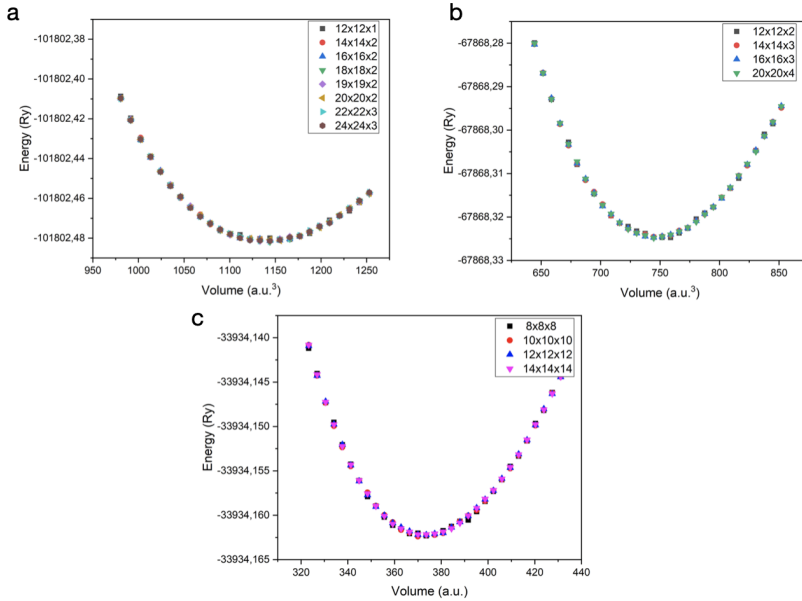
Figure 7.2: Geometry optimization of the (a) 2H-3R, (b) 2H, and (c) 3R structures. The convergence of the calculations for the 2H and 3R structures is verified by varying the amount of number of k-point sampling. For the 2H-3R crystal structure, a larger set of k-point sampling turns out to be required.

7.4.2. DENSITY OF STATES & BAND STRUCTURE

We continue our discussion with the density of states and electronic band structure of the three WS$_2$ polytypes. In Figure 7.4 the total density of states, the projected density of states, and the band structure, of the 2H, 3R, and 2H-3R polytypism are displayed. For all three crystalline structures, it is the W d-orbitals that primarily allows occupied and unoccupied states near the Fermi energy, a result which is consistent with related DFT studies on MoS$_2$ by Espejo *et al.* [2] and Coutinho *et al.* [40]. The effects of spin-orbit coupling (SOC) are also taken into account, the result of which leads to a small change in the density of states near the Fermi energy for all cases.

The band gap of the 2H-3R polytype is 1.48 eV without SOC and 1.40 eV with SOC, while

Crystal Phase	GW calculation	DOS, band structure, ELF
2H-3R	6 x 6 x 1	23 x 23 x 3
2H	6 x 6 x 1	20 x 20 x 4
3R	4 x 4 x 4	16 x 16 x 16

Table 7.2: k-mesh used for the calculations, of the density of states, band structure, and energy loss function. The k-meshes are kept the same for the calculations with and without spin-orbit coupling.

the band gap of the 2H structure is 1.39 eV without SOC and 1.34 eV with SOC. Including spin-orbit coupling has a most prominent effect for the 3R polytype, as we observe a dramatic shift in the calculated band gap value of the 3R polytype, decreasing from 1.62 eV(without SOC) to 1.47 eV(with SOC), compared to the rather more modest shift for the 2H (from 1.39 eV to 1.34 eV) and 2H-3R (from 1.48 eV to 1.40 eV) polytypes. We note that that band gap value of the 2H-3R polytypism lies in between those of the 2H and 3R polytypes in the cases with and without spin-orbit coupling. This effect could be explained by the one-shot post inclusion of spin-orbit coupling in the GW calculations.

For the band structure plots, we choose k-paths in the primitive Brillouin zones such that a complete irreducible set of symmetry lines is obtained. For the 2H and 2H-3R poly-types, identical k-paths in the Brillouin zone are chosen since their primitive Brillouin zone have identical symmetry points. For the 3R polytype we follow the prescriptions of [41–46] for the selection of the k-path in the primitive Brillouin zone. The Brillouin zone for the 2H and 2H-3R structures can be seen in Figure 7.3, while the Brillouin zone for the 3R structure can be seen in Figure 7.3. Due to the similarity of the primitive Bril-louin zones of the 2H and 2H-3R polytypes, we are able to make a direct comparison of the conduction and valence bands behaviours. Such a direct comparison is not possible for all three polytypes, since the primitive Brillouin zone of the 3R structure is dissimilar to those of the 2H and 2H-3R Brillouin zones.

In the case of the 2H and 2H-3R polytypes, the conduction band minima is found to be at the same point in the Brillouin zone, located between the K and Γ points in the Brillouin zone. While the valence band maximum for the 2H is at the Γ point, for the 2H-3R polytypism the valence band maximum lies at the A point. In the case of the 2H-3R polytypism there are three bands near the Fermi, as oppose to two bands near the Fermi energy for the 2H case. The extra band near the Fermi energy in the 2H-3R polytypism is the cause of the shift of the valence band maximum from the Γ point to the A point. As a consequence of the extra band near the Fermi energy, an additional band can be found near the K point. The extra band near the K point leads to additional bands appearing when taking spin-orbit coupling into account.

As mentioned above, the band gap of the 3R structure is 1.62 eV without SOC and 1.47 eV with SOC. In the case of the 3R structure, the valence band maximum lies at the Z point, while the conduction band minimum lies between the Γ and X points in the Brillouin zone. For this 3R crystal structure, we see that the band near the Fermi energy is split into two bands at the B, X and Q points in the Brillouin zone when including spin-orbit coupling. The conduction band minimum lies between the Γ and X points and is pushed down in energy when including spin-orbit coupling, while the maximum of the valence band is not changed significantly by the inclusion of spin-orbit coupling.
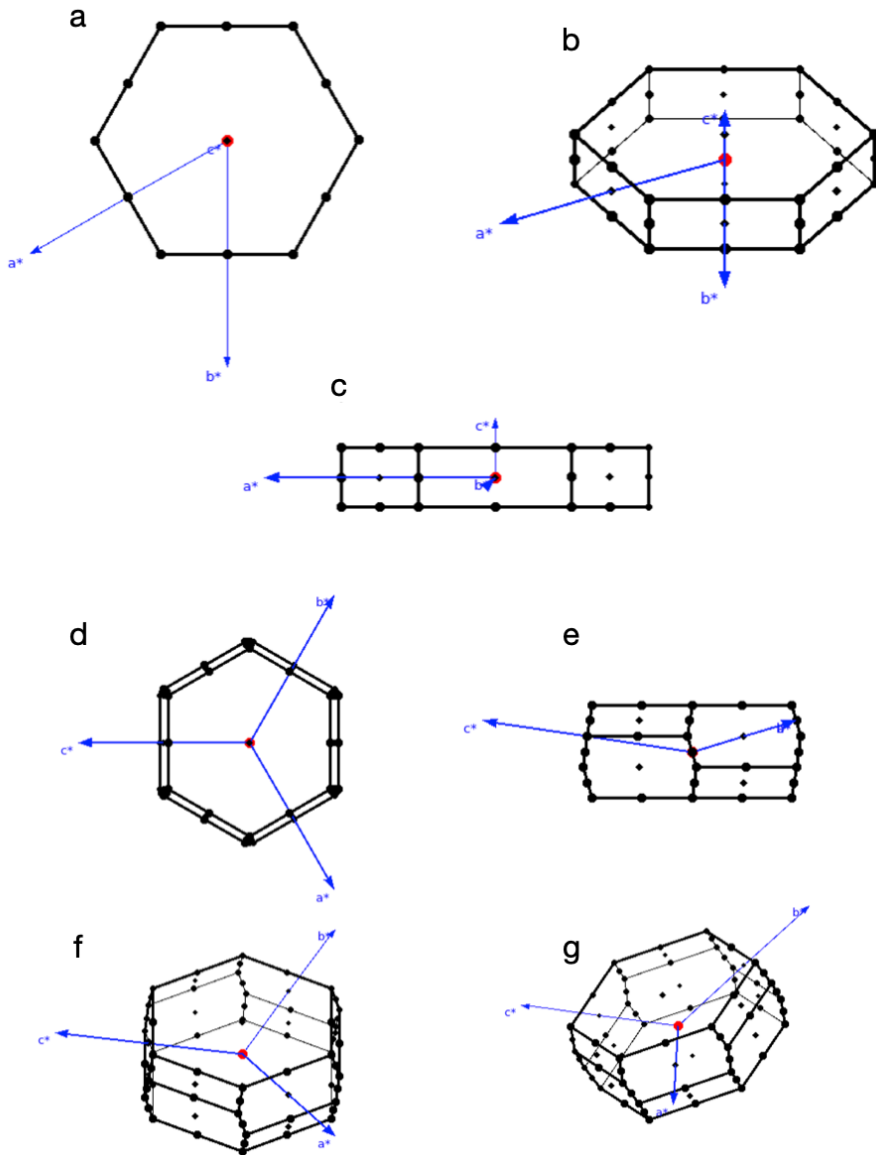
Figure 7.3: Primitive Brillouin zone of the 2H and 2H-3R structures. (a) Top and (c) side view of the primitive Brillouin zone together with the reciprocal lattice vectors a*, b*, and c*. Skew view (b) of the 2H and 2H-3R primitive Brillouin zones illustrating the rest of the primitive Brillouin zone. Following [41–46] we choose a k-path along the Γ-M-K-Γ-A-L-H-A high symmetry points for the band structure plots for the 2H and 2H-3R systems. Primitive Brillouin zone of the 3R structure.(d) Top and (e) side view of the primitive Brillouin zone together with the reciprocal lattice vectors a*, b*, and c*. Different skew view (f) and (g) further illustrate the primitive Brillouin zone of the 3R structure. Following [41–46] we choose a k-path along the Γ-L-B1-B-Z-Γ-X-Q-F-P1-Z-L-P-Z high symmetry points for the band structure plots for the 3R system.
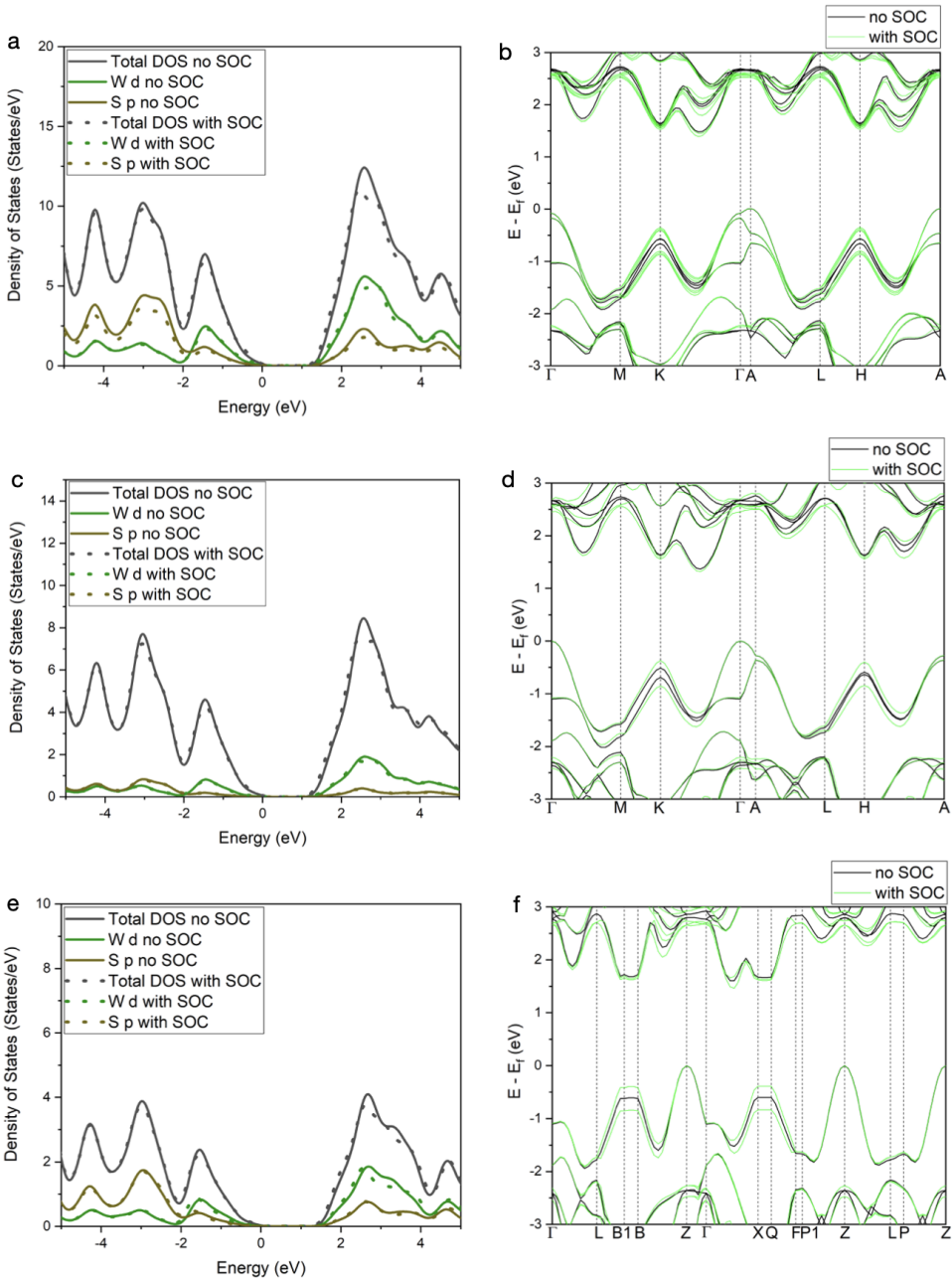
Figure 7.4: Density of states of the (a) 2H-3R, (c) 2H, and (e) 3R structures, with and without spin-orbit coupling (SOC) taken into account. Band structure plot of the (b) 2H-3R, (d) 2H, and (f) 3R structures with and without spin-orbit coupling.

7.4.3. Energy Loss Function & Joint Density of States

We continue our discussion of the theoretical predictions of the electronic and optical properties of the WS$_2$ polytypes by describing the energy loss function and the joint density of states, first for the 2H-3R polytype and then with the 2H and 3R crystal phases. Due to the symmetry properties of these polytypes, we have two distinct sets of energy losses for each polytype, namely the in-plane and out-of-plane energy-losses. For this reason, we represent graphically the energy loss associated with in-plane and out-of-plane losses separately. Additionally, we compare the energy loss function calculated at the DFT level and at the GW level, with and without taking the spin-orbit coupling effects into account.

The energy loss function for the different WS$_2$ polytypes is displayed in Figures 7.5, 7.6, and 7.7 respectively. For all the different crystal structures considered, the in-plane and out-of-plane bulk plasmon peaks lie between 20.91 eV and 22.02 eV. The in-plane and out-of-plane bulk plasmons differ by no more than 0.24 eV for both the DFT and GW calculations. The effects of spin-orbit coupling can be clearly seen both at the DFT and at the GW level: the bulk plasmon peaks for both in-plane and out-of-plane losses shifts towards lower energy losses. The positions of the bulk plasmon peaks for the different crystal structures and theoretical calculations are reported in Table 7.3.

Furthermore, in the energy loss region below losses of 10 eV we observe a number of distinct peaks. These features present in the low-loss region could be attributed to inter-band transitions between the valence and conduction bands near the Fermi energy, as we will discuss below. We present results for the joint density of states calculated at the GW level. We compare results with and without taking spin-orbit coupling into account. For all three polytypes, we calculate the joint density of states taking all the bands into account.

We also evaluate the contribution of separate bands to the joint density of states to elucidate which one are important in specific energy losses regions. We start with the calculation of the joint density of states by including one valence band, the top valence band, and one conduction band, specifically the bottom conduction band. We then include an increasing amount of valence and conduction bands with respect to the top valence band and the bottom conduction band, and represent graphically the results while comparing with the total joint density of states. We note that in the cases including spin-orbit coupling, we double the amount of bands needed with respect to the case without spin-orbit coupling to properly describe the energy loss spectra.

In order to properly describe the bulk plasmon peaks appearing in the energy loss regions in the range between 10 eV to 30 eV range, a larger amount of bands needs to be incorporated into the joint density of states calculation; this is consistent with the concept of plasmons arising as collective excitations of the electrons in the material. We continue first without considering spin-orbit coupling. In the energy loss region below 10 eV, we observe from the joint density of states that the top twenty valence bands and bottom twenty conduction bands can completely describe the energy regions below 10 eV for the 2H polytype, while for the 3R polytype ten valence bands and ten conduction bands is sufficient to completely describe the energy loss region below 10 eV. For the

2H-3R polytypism a larger amount of bands is needed to completely describe the region below 10 eV. As we proceed towards smaller energy losses we can see that a decreasing amount of valence and conduction bands are needed to explain the peaks in the corresponding energy region for all the polytypes.

7.4.4. DISCUSSION & COMPARISON WITH EXPERIMENT

Our calculations for the value of the band gap and the location of the bulk plasmon peak for the 2H crystal structure of WS_2 are found to be in good agreement with previous theoretical and experimental work [3, 5, 47–50]. Therefore, we are confident that we can reliably apply the same theoretical machinery to predict the electrical and optical properties of the corresponding 2H-3R polytype.

In this work we have also calculated that the 2H-3R polytype should exhibit an indirect band gap with a value in the range between 1.40 eV 1.48 eV. This prediction is in excellent agreement with the experimental result reported in [18, 19], where a band gap value of $1.6^{+0.3}_{-0.2}$ eV was extracted after subtracting the EELS zero-loss peak using machine learning techniques.

Finally, for the 3R polytype we have calculated an indirect band gap with a value in the range between 1.47 and 1.62 eV. The large discrepancy for the band gap calculations in the cases with and without taking into account the spin-orbit coupling could be related to an insufficiently dense k-mesh used in the GW calculation for the 3R polytype. For this crystal structure, we also calculate a bulk plasmon peak whose position is close to that of the 2H and 2H-3R polytypes. As of writing, no experimental measurements of the position of the bulk plasmon peak, the band gap type, or the band gap value have been reported for the 3R polytype and hence we cannot compare our predictions to experimental data.

In the case of 2H-3R polytypism, the location of the bulk plasmon peak observed in WS_2 nanostructures by means of electron-energy loss spectroscopy [18, 19] is rather similar to that of the bulk plasmon peak in the 2H polytype, in agreement with the theoretical predictions in this work.

Crystal Phase	DFT no SOC	DFT with SOC	GW no SOC	GW with SOC
2H-3R$_\parallel$	21.67 eV	20.72 eV	21.57 eV	20.91 eV
2H-3R$_\perp$	21.43 eV	20.94 eV	21.65 eV	21.10 eV
2H$_\parallel$	22.03 eV	20.69 eV	21.57 eV	21.46 eV
2H$_\perp$	21.84 eV	20.94 eV	21.76 eV	21.57 eV
3R$_\parallel$	21.95 eV	20.94 eV	21.43 eV	21.08 eV
3R$_\perp$	22.00 eV	21.02 eV	21.97 eV	21.59 eV

Table 7.3: In-plane ($\parallel$) and out-of-plane ($\perp$) locations of the bulk plasmon (BP) peaks for the three different WS_2 polytypes considered here. We show results for both the DFT and GW calculations, with and without spin-orbit coupling effects.
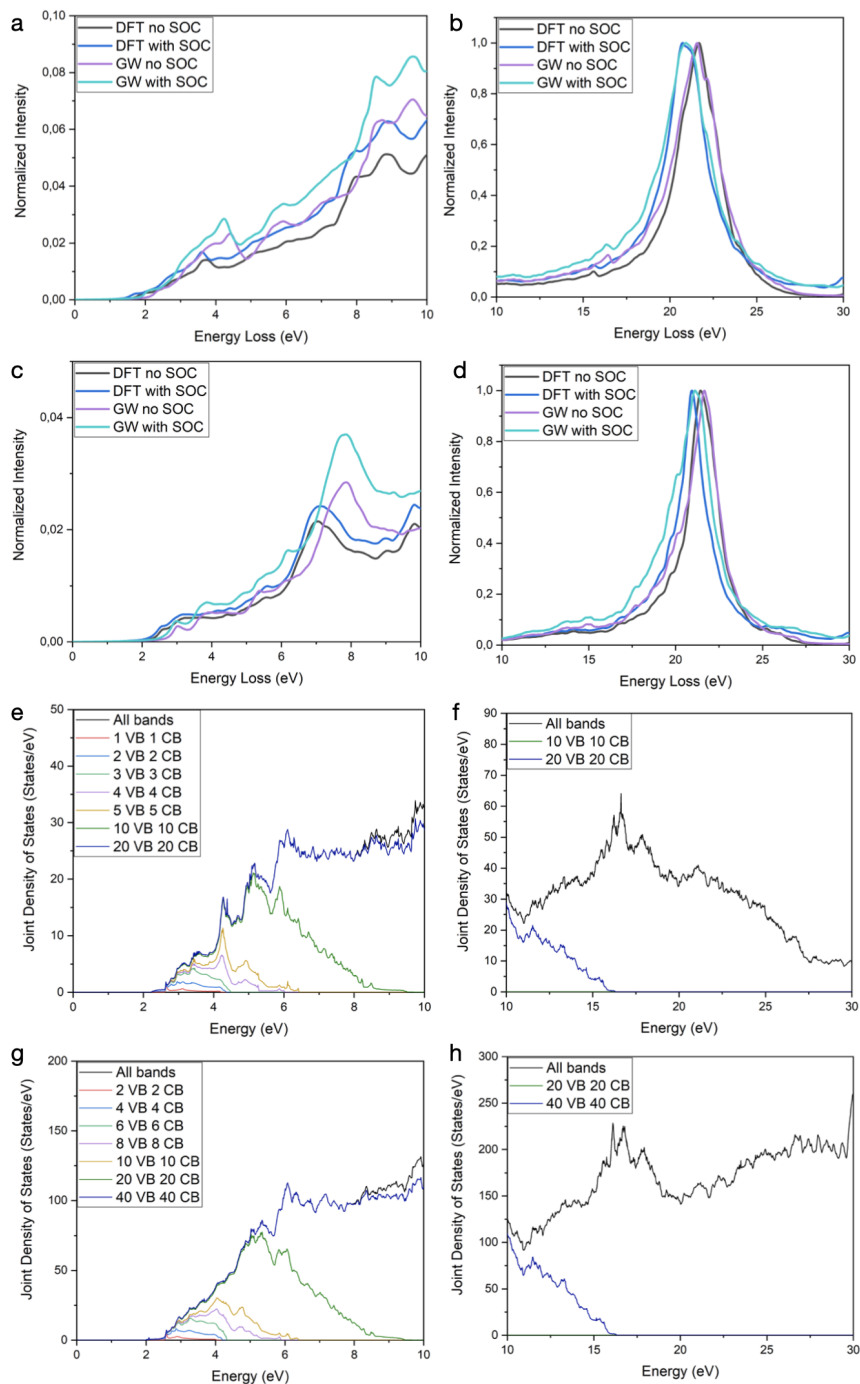
Figure 7.5: Energy loss function for the 2H-3R polytype of WS$_2$. (a) and (b) in-plane energy loss function with and without spin-orbit coupling (SOC). (c) and (d) out-of-plane energy loss function with and without SOC. Joint density of states of 2H-3R structure calculated on the GW level (e) and (f) without spin-orbit coupling. (g) and (h) with spin-orbit coupling. Here VB and CB stand for Valence Band and Conduction Band respectively.
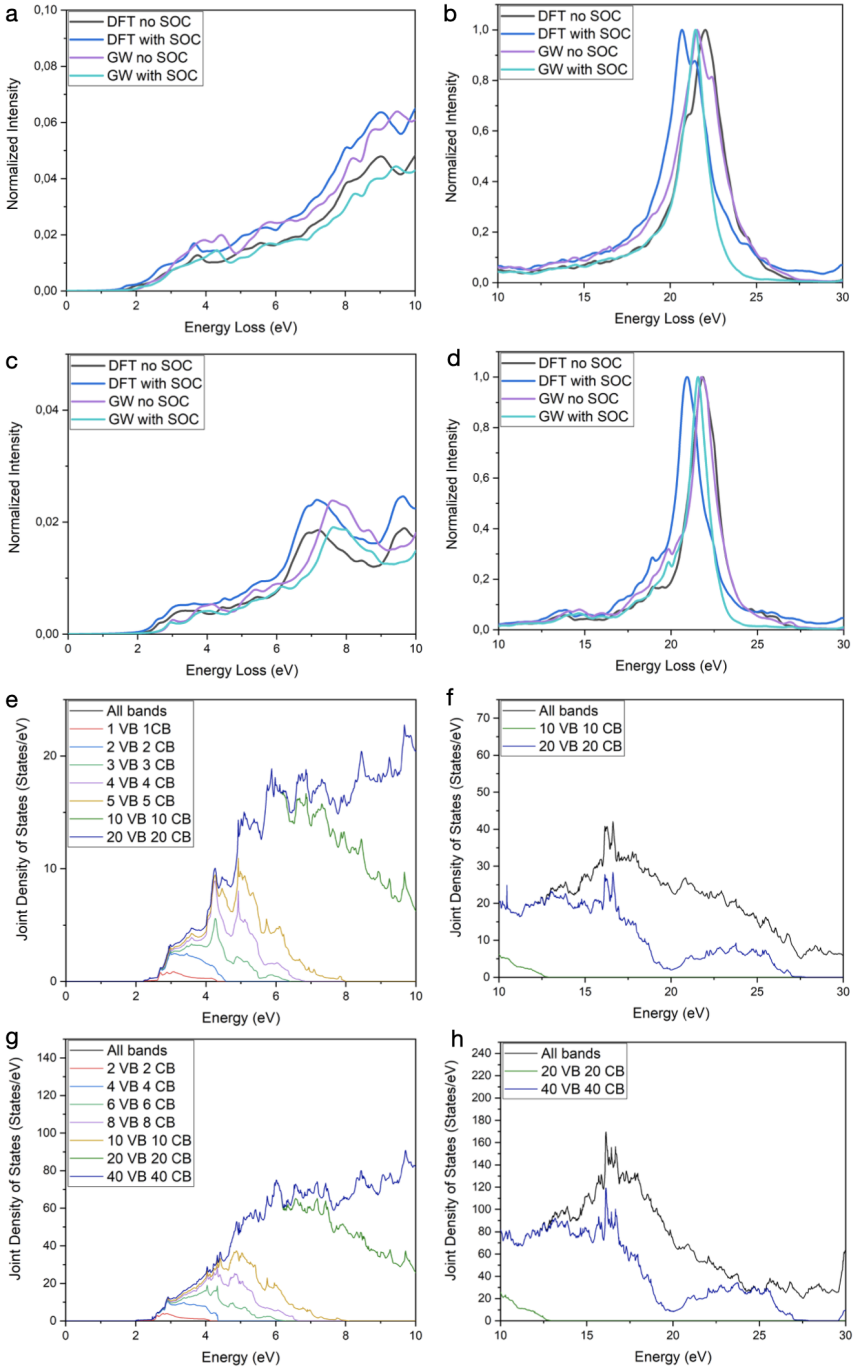
Figure 7.6: Same as Fig. 7.5 for the 2H crystal structure.
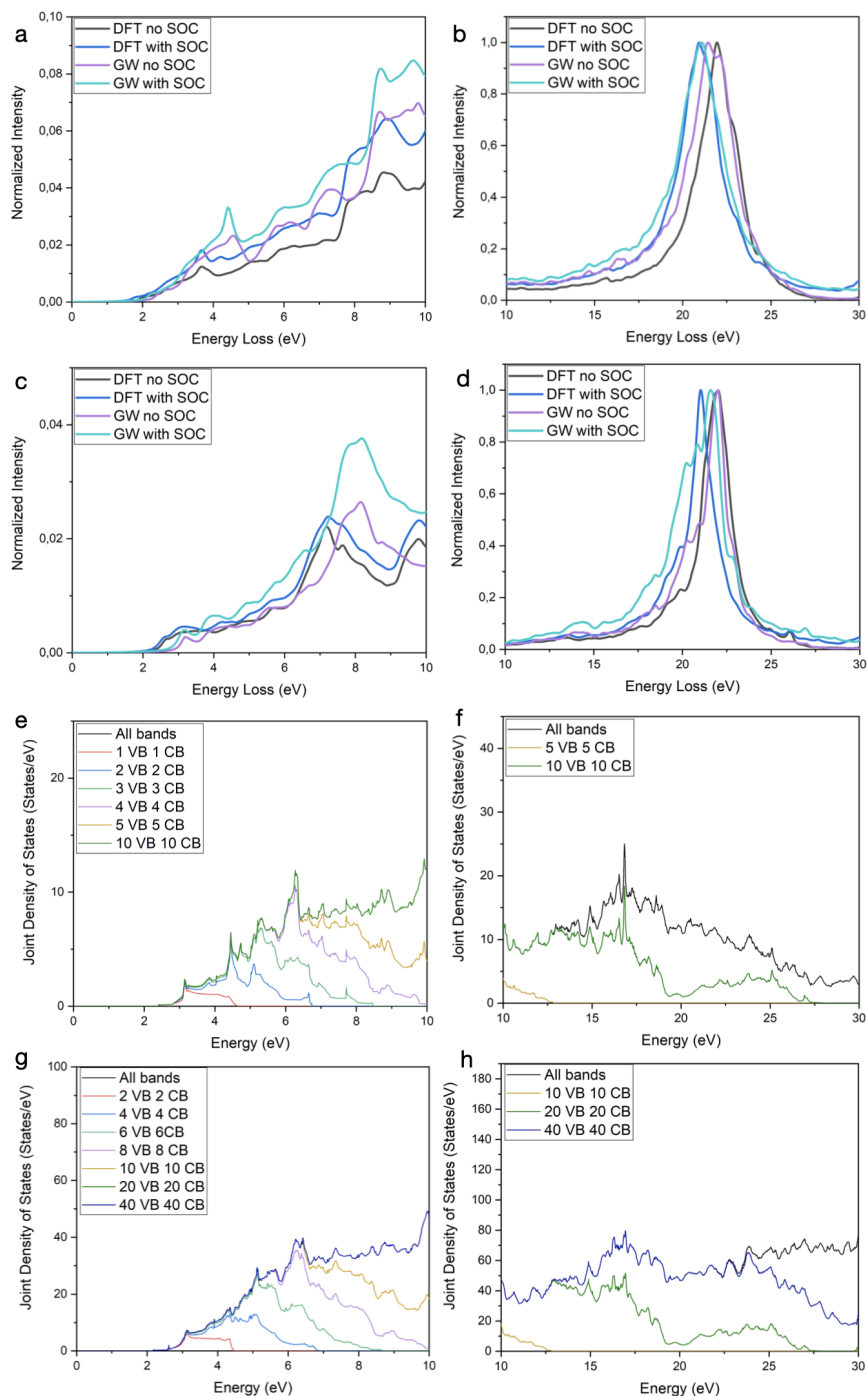
Figure 7.7: Same as Fig. 7.5 for the 3R crystal structure.
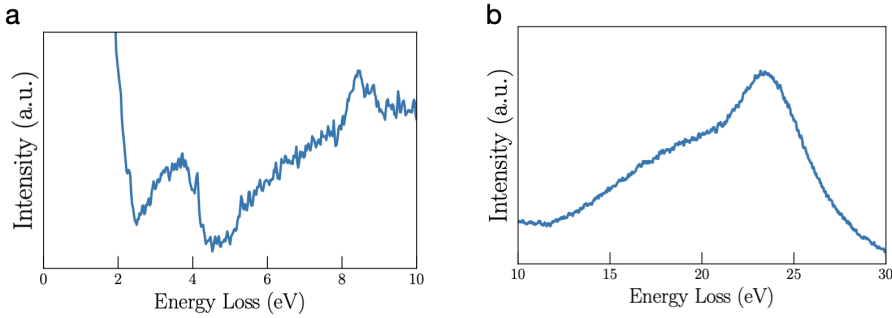
Figure 7.8: (a,b) Experimental EELS measurements acquired on a WS$_2$ nanostructure characterized by the same 2H/3R polytypism. Note that the zero-loss peak (ZLP) has not been subtracted from the EELS data.

Figure 7.8(c,d) displays then experimental EELS measurements acquired on a WS$_2$ nanostructure also characterized by the same 2H/3R polytypism [18, 19] in the same energy-loss range that the corresponding theoretical calculations. Note that the zero-loss peak (ZLP) has not been subtracted from the EELS data. In these experimental measurements, one observes in the low-loss region two peaks located at 3.5 eV and 8 eV. The peak at 8 eV, which can be associated to the interlayer coupling, is consistent with the features of the GW calculation both including and excluding SOC effects. On the other hand, the feature at 3.5 eV is not visible in the calculated ELF, but calculated DOS, see Figure 3.2(a), indicates that this peak is associated to a electronic transition from occupied d states to unoccupied d states of W. The absence of the feature at 3.5 eV energy loss can be explained due to limitations of the GW approach; GW accurately describes a single-particle process, however for optical excitations the effect of interactions between holes and electrons needs to be taken into account. Properly describing electron-hole interactions could be achieved by solving the Bethe-Salpeter Equations (BSE) [51–53]. Further details about the origin of these two observed peaks in the low-loss region can be found in the JDOS discussion below.

Concerning the bulk plasmon, it is located at around 23 eV in the experimental EELS measurements while in the DFT and GW calculations it appears at slightly smaller values. The slight discrepancy between the calculated and experimentally measured bulk plasmons of the mixed 2H-3R polytype can be attributed to the exclusion of local field effects and non-zero momentum transfer effects while calculating the dielectric response of the material as implemented in the optic package[33, 34, 54].

7.5. CONCLUSIONS & OUTLOOK

In this work, we have carried out *ab initio* calculations based on the 2H, 3R, and 2H-3R polytypes of WS$_2$. We showed how the band gap value of the 2H-3R polytypism lies between the band gap values of the 2H and 3R polytypes, where it is observed to be closer to the 2H band gap value compared to the 3R band gap value, and is in good agreement with experimental measurements.

Comparable band structures were found of the 2H and 2H-3R polytypes, where the top of the valence band of the 2H-3R polytypism lies at the A high symmetry point. We have shown that the bulk plasmon peaks of all the polytypes occurs at very similar energy loss values. For the energy loss function, we have determined the contribution of the different valence and conduction bands to the energy loss intensity for different energy loss regions.

One point of future research would be the determination of the character of the different contributing bands in the low loss region. Additionally, a denser k-mesh for the 3R GW calculation should be implemented in order to determine whether the band gap discrepancy for calculations with and without spin-orbit coupling can be explained. Further studies of the energy loss function near the band gap can be carried out by solving the Bethe-Salpeter equations to determine how the excitonic behaviour between the polytypes may differ among them [4, 6, 55, 56].

REFERENCES

[1] S. Manzeli, D. Ovchinnikov, D. Pasquier, O. V. Yazyev, and A. Kis, *2D transition metal dichalcogenides,* Nature Reviews Materials **2**, 17033 (2017).

[2] C. Espejo, T. Rangel, A. H. Romero, X. Gonze, and G.-M. Rignanese, *Band structure tunability in MoS$_2$ under interlayer compression: A DFT and GW study,* Phys. Rev. B **87**, 245114 (2013).

[3] P. Johari and V. B. Shenoy, *Tunable Dielectric Properties of Transition Metal Dichalcogenides,* ACS Nano **5**, 5903 (2011), pMID: 21707067, https://doi.org/10.1021/nn201698t .

[4] A. Ramasubramaniam, D. Naveh, and E. Towe, *Tunable band gaps in bilayer transition-metal dichalcogenides,* Phys. Rev. B **84**, 205325 (2011).

[5] J. Gusakova, X. Wang, L. L. Shiau, A. Krivosheeva, V. Shaposhnikov, V. Borisenko, V. Gusakov, and B. K. Tay, *Electronic Properties of Bulk and Monolayer TMDs: Theoretical Study Within DFT Framework (GVJ-2e Method),* physica status solidi (a) **214**, 1700218 (2017), https://onlinelibrary.wiley.com/doi/pdf/10.1002/pssa.201700218 .

[6] J. Ryou, Y.-S. Kim, S. Kc, and K. Cho, *Monolayer MoS$_2$ Bandgap Modulation by Dielectric Environments and Tunable Bandgap Transistors,* Scientific Reports **6** (2016).

[7] T. Eknapakul, P. D. C. King, M. Asakawa, P. Buaphet, R.-H. He, S.-K. Mo, H. Takagi, K. M. Shen, F. Baumberger, T. Sasagawa, S. Jungthawan, and W. Meevasana, *Electronic Structure of a Quasi-Freestanding MoS$_2$ Monolayer,* Nano Letters **14**, 1312 (2014), pMID: 24552197, https://doi.org/10.1021/nl4042824 .

[8] K. F. Mak, C. Lee, J. Hone, J. Shan, and T. F. Heinz, *Atomically Thin MoS$_2$: A New Direct-Gap Semiconductor,* Phys. Rev. Lett. **105**, 136805 (2010).

[9] H. Xu, S. Liu, Z. Ding, S. J. R. Tan, K. M. Yam, Y. Bao, C. T. Nai, M.-F. Ng, J. Lu, C. Zhang, and K. P. Loh, *Oscillating edge states in one-dimensional MoS$_2$ nanowires,* Nature Communications **7**, 12904 (2016).

[10] M. Tinoco, L. Maduro, M. Masaki, E. Okunishi, and S. Conesa-Boj, *Strain-Dependent Edge Structures in MoS$_2$ Layers,* Nano Letters **17**, 7021 (2017), pMID: 29064254, https://doi.org/10.1021/acs.nanolett.7b03627 .

[11] M. Tinoco, L. Maduro, and S. Conesa-Boj, *Metallic edge states in zig-zag vertically-oriented MoS$_2$ nanowalls,* Scientific Reports **9**, 15602 (2019).

[12] J. He, K. Hummer, and C. Franchini, *Stacking effects on the electronic and optical properties of bilayer transition metal dichalcogenides MoS$_2$, MoSe$_2$, WS$_2$, and WSe$_2$,* Phys. Rev. B **89**, 075409 (2014).

[13] R. Suzuki, M. Sakano, Y. J. Zhang, R. Akashi, D. Morikawa, A. Harasawa, K. Yaji, K. Kuroda, K. Miyamoto, T. Okuda, K. Ishizaka, R. Arita, and Y. Iwasa, *Valley-dependent spin polarization in bulk MoS$_2$ with broken inversion symmetry,* Nature Nanotechnology **9**, 611 (2014).

[14] L. Chen, H. Feng, R. Zhang, S. Wang, X. Zhang, Z. Wei, Y. Zhu, M. Gu, and C. Zhao, *Phase-Controlled Synthesis of 2H/3R-MoSe$_2$ Nanosheets on P-Doped Carbon for Synergistic Hydrogen Evolution,* ACS Applied Nano Materials **3**, 6516 (2020), https://doi.org/10.1021/acsanm.0c00988 .

[15] J. Wilson and A. Yoffe, *The transition metal dichalcogenides discussion and interpretation of the observed optical, electrical and structural properties,* Advances in Physics **18**, 193 (1969), https://doi.org/10.1080/00018736900101307 .

[16] J.-U. Lee, K. Kim, S. Han, G. H. Ryu, Z. Lee, and H. Cheong, *Raman Signatures of Polytypism in Molybdenum Disulfide,* ACS Nano **10**, 1948 (2016), pMID: 26756836, https://doi.org/10.1021/acsnano.5b05831 .

[17] A. A. Puretzky, L. Liang, X. Li, K. Xiao, K. Wang, M. Mahjouri-Samani, L. Basile, J. C. Idrobo, B. G. Sumpter, V. Meunier, and D. B. Geohegan, *Low-Frequency Raman Fingerprints of Two-Dimensional Metal Dichalcogenide Layer Stacking Configurations,* ACS Nano **9**, 6333 (2015), pMID: 25965878, https://doi.org/10.1021/acsnano.5b01884 .

[18] S. E. van Heijst, M. Mukai, E. Okunishi, H. Hashiguchi, L. I. Roest, L. Maduro, J. Rojo, and S. Conesa-Boj, *Illuminating the Electronic Properties of WS$_2$ Polytypism with Electron Microscopy,* Annalen der Physik **n/a**, 2000499, https://onlinelibrary.wiley.com/doi/pdf/10.1002/andp.202000499 .

[19] L. I. Roest, S. E. van Heijst, L. Maduro, J. Rojo, and S. Conesa-Boj, *Charting the low-loss region in electron energy loss spectroscopy with machine learning,* Ultramicroscopy **222**, 113202 (2021).

[20] P. Hohenberg and W. Kohn, *Inhomogeneous electron gas,* Phys. Rev. **136**, B864 (1964).

[21] W. Kohn and L. J. Sham, *Self-consistent equations including exchange and correlation effects,* Phys. Rev. **140**, A1133 (1965).

7

[22] P. Blaha, K. Schwarz, G. K. Madsen, D. Kvasnicka, J. Luitz, *et al.*, *wien2k,* An augmented plane wave+ local orbitals program for calculating crystal properties (2001).

[23] P. Blaha, K. Schwarz, F. Tran, R. Laskowski, G. K. H. Madsen, and L. D. Marks, *WIEN2k: An APW+lo program for calculating the properties of solids,* The Journal of Chemical Physics **152**, 074101 (2020), https://doi.org/10.1063/1.5143061 .

[24] H. Jiang, R. I. Gómez-Abal, X.-Z. Li, C. Meisenbichler, C. Ambrosch-Draxl, and M. Scheffler, *Fhi-gap: A gw code based on the all-electron augmented plane wave method,* Computer Physics Communications **184**, 348 (2013).

[25] H. Jiang and P. Blaha, *GW with linearized augmented plane waves extended by high-energy local orbitals,* Phys. Rev. B **93**, 115203 (2016).

[26] A. Yan, W. Chen, C. Ophus, J. Ciston, Y. Lin, K. Persson, and A. Zettl, *Identifying different stacking sequences in few-layer cvd-grown* Mos_2 *by low-energy atomic-resolution scanning transmission electron microscopy,* Phys. Rev. B **93**, 041420 (2016).

[27] P. E. Blöchl, O. Jepsen, and O. K. Andersen, *Improved tetrahedron method for Brillouin-zone integrations,* Phys. Rev. B **49**, 16223 (1994).

[28] J. Klimeš, D. R. Bowler, and A. Michaelides, *Chemical accuracy for the van der Waals density functional,* Journal of Physics: Condensed Matter **22**, 022201 (2009).

[29] J. c. v. Klimeš, D. R. Bowler, and A. Michaelides, *Van der Waals density functionals applied to solids,* Phys. Rev. B **83**, 195131 (2011).

[30] A. D. Becke, *Density-functional exchange-energy approximation with correct asymptotic behavior,* Phys. Rev. A **38**, 3098 (1988).

[31] J. P. Perdew and Y. Wang, *Accurate and simple analytic representation of the electron-gas correlation energy,* Phys. Rev. B **45**, 13244 (1992).

[32] M. Dion, H. Rydberg, E. Schröder, D. C. Langreth, and B. I. Lundqvist, *Van der Waals Density Functional for General Geometries,* Phys. Rev. Lett. **92**, 246401 (2004).

[33] C. Ambrosch-Draxl and J. O. Sofo, *Linear optical properties of solids within the full-potential linearized augmented planewave method,* Computer Physics Communications **175**, 1 (2006).

[34] V. Keast, *An introduction to the calculation of valence EELS: Quantum mechanical methods for bulk solids,* Micron **44**, 93 (2013).

[35] C. Hébert, *Practical aspects of running the WIEN2k code for electron spectroscopy,* Micron **38**, 12 (2007).

[36] D. D. Koelling and B. N. Harmon, *A technique for relativistic spin-polarised calculations,* Journal of Physics C: Solid State Physics **10**, 3107 (1977).

7

[37] A. H. MacDonald, W. E. Picket, and D. D. Koelling, *A linearised relativistic augmented-plane-wave method utilising approximate pure spin basis functions,* Journal of Physics C: Solid State Physics **13**, 2675 (1980).

[38] W. E. Pickett, H. Krakauer, and P. B. Allen, *Smooth Fourier interpolation of periodic functions,* Phys. Rev. B **38**, 2721 (1988).

[39] W. Schutte, J. De Boer, and F. Jellinek, *Crystal structures of tungsten disulfide and diselenide,* Journal of Solid State Chemistry **70**, 207 (1987).

[40] S. Coutinho, M. Tavares, C. Barboza, N. Frazão, E. Moreira, and D. L. Azevedo, *3R and 2H polytypes of MoS2: DFT and DFPT calculations of structural, optoelectronic, vibrational and thermodynamic properties,* Journal of Physics and Chemistry of Solids **111**, 25 (2017).

[41] W. Setyawan and S. Curtarolo, *High-throughput electronic band structure calculations: Challenges and tools,* Computational Materials Science **49**, 299 (2010).

[42] J. Perez-Mato, D. Orobengoa, E. Tasci, G. De la Flor Martin, and A. Kirov, *Crystallography online: Bilbao crystallographic server,* Bulgarian Chemical Communications **43**, 183 (2011).

[43] M. I. Aroyo, J. M. Perez-Mato, C. Capillas, E. Kroumova, S. Ivantchev, G. Madariaga, A. Kirov, and H. Wondratschek, *Bilbao crystallographic server: I. databases and crystallographic computing programs,* Zeitschrift für Kristallographie - Crystalline Materials **221**, 15 (2006).

[44] M. I. Aroyo, A. Kirov, C. Capillas, J. M. Perez-Mato, and H. Wondratschek, *Bilbao Crystallographic Server. II. Representations of crystallographic point groups and space groups,* Acta Crystallographica Section A **62**, 115 (2006).

[45] M. I. Aroyo, D. Orobengoa, G. de la Flor, E. S. Tasci, J. M. Perez-Mato, and H. Wondratschek, *Brillouin-zone database on the Bilbao Crystallographic Server,* Acta Crystallographica Section A **70**, 126 (2014).

[46] Tasci, E.S., de la Flor, G., Orobengoa, D., Capillas, C., Perez-Mato, J.M., and Aroyo, M.I., *An introduction to the tools hosted in the bilbao crystallographic server,* EPJ Web of Conferences **22**, 00009 (2012).

[47] K. K. Kam and B. A. Parkinson, *Detailed photocurrent spectroscopy of the semiconducting group VIB transition metal dichalcogenides,* The Journal of Physical Chemistry **86**, 463 (1982), https://doi.org/10.1021/j100393a010 .

[48] H. Jiang, *Electronic band structures of molybdenum and tungsten dichalcogenides by the gw approach,* The Journal of Physical Chemistry C **116**, 7664 (2012), https://doi.org/10.1021/jp300079d .

[49] M. Bell and W. Liang, *Electron energy loss studies in solids; the transition metal dichalcogenides,* Advances in Physics **25**, 53 (1976), https://doi.org/10.1080/00018737600101362 .

7

[50] W. Y. Liang and S. L. Cundy, *Electron energy loss studies of the transition metal dichalcogenides,* The Philosophical Magazine: A Journal of Theoretical Experimental and Applied Physics **19**, 1031 (1969), https://doi.org/10.1080/14786436908225867 .

[51] J. Deslippe, G. Samsonidze, D. A. Strubbe, M. Jain, M. L. Cohen, and S. G. Louie, *"berkeleygw: A massively parallel computer package for the calculation of the quasiparticle and optical properties of materials and nanostructures",* Computer Physics Communications **183**, 1269 (2012).

[52] A. Gulans, S. Kontur, C. Meisenbichler, D. Nabok, P. Pavone, S. Rigamonti, S. Sagmeister, U. Werner, and C. Draxl, *Exciting: a full-potential all-electron package implementing density-functional theory and many-body perturbation theory,* Journal of Physics: Condensed Matter **26**, 363202 (2014).

[53] C. Vorwerk, B. Aurich, C. Cocchi, and C. Draxl, *"bethe-salpeter equation for absorption and scattering spectroscopy: implementation in the exciting code",* Electronic Structure **1**, 037001 (2019).

[54] H. Raether, *Excitation of plasmons and interband transitions by electrons,* Vol. 88 (Springer, 1980) pp. 19–22.

[55] X. Leng, F. Jin, M. Wei, and Y. Ma, *GW method and Bethe-Salpeter equation for calculating electronic excitations,* WIREs Computational Molecular Science **6**, 532 (2016), https://www.onlinelibrary.wiley.com/doi/pdf/10.1002/wcms.1265 .

[56] X. Blase, I. Duchemin, D. Jacquemin, and P.-F. Loos, *The Bethe-Salpeter Equation Formalism: From Physics to Chemistry,* The Journal of Physical Chemistry Letters **11**, 7371 (2020), pMID: 32787315, https://doi.org/10.1021/acs.jpclett.0c01875 .

7

8

OUTLOOK

A PATH FORWARD

I̱N this thesis, we have discussed a broad range of theoretical calculations, fabrication and sample preparation strategies, and characterization techniques. A variety of structures based on transition metal dichalcogenides were studied, both in experimental measurements, and theoretical modelling of transition metal dichalcogenides for the interpretation of electron energy loss spectra in the transmission electron microscope. In this final chapter of the thesis we will provide an outlook on some of the questions left unanswered and on possible routes for further research.

In Chapter 3 we have seen how monochromated electron energy loss spectroscopy measurements along with structural characterization in the transmission electron microscope can be used to probe the properties of monolayers and edge structures of MoS_2. Likewise, in Chapter 4 we have seen how focused ion beam milling along with exploiting the crystallographic symmetries of MoS_2 can be used to expose edge-dependent electronic properties of MoS_2 nanowalls. The sample preparation strategies, along with characterization techniques, can be used to study other transition metal dichalcogenide structures with similar preparation parameters as those discussed in chapters 3 and 4.

However, some open questions remain concerning *ab initio* methods to interpret the energy loss spectra of MoS_2 monolayers ands nanowalls. We address the issues of *ab initio* methods at the end of this outlook chapter. In Chapters 5 and 6 we have demonstrated a scalable strategy to fabricate and synthesize core-shell nanopillars based on transition metal dichalcogenides. In the next section we address some open questions which would be important to address in the context of these core-shell nanopillars.

TRANSITION METAL DICHALCOGENIDES-BASED NANOPILLARS

FABRICATION STRATEGY

In Chapters 4 and 7 we have demonstrated how the combination of nanofabrication and chemical vapour deposition makes it possible to produce core-shell Mo-MoS_2 nanopillars. The size, shape, and density of these nanopillars can be easily controlled in the fabrication step, while the shell can be controlled in the chemical vapour deposition step.

The described procedure could be expanded to other TMDs by using a different chalcogen powder for the chemical vapour deposition, such as Se or Te, or mixtures thereof to create ternary or quaternary core-shell TMD nanopillars based on Mo [1, 2]. Another approach is to change the transition metal in the fabrication step, where an example with W has already been demonstrated in chapter 6. The fabrication of W nanopillars up to now has not been of the same quality as the Mo nanopillars, e.g. the shape control and sharp reproducible sidewalls have not been achieved in W nanopillar fabrication.

One way to improve the W nanopillar fabrication is to experiment with different etching parameters such as higher etching temperatures, different ICP power, platen power, or SF_6/O_2 gas mixtures. Another pathway for improving the W nanopillar fabrication is to experiment with different sputter-deposition parameters of the W film, such as deposition of W in multiple steps.

8

One can also imagine sputtering a mixture of Mo and W layers to create transition metal heterostructures for fabrication and subsequent sulfurization in the chemical vapour deposition process. It remains to be seen whether the fabrication strategy can be extended to other transition metals that also form flourides and oxyflourides, such as Nb or Ta [3–5].

NANOPILLARS CHARACTERIZATION

In Chapter 6, structural and local electronic analyses of core-shell nanopillars were carried out in the transmission electron microscope. From the structural analysis we have found the growth of the MoS_2 layers which are oriented perpendicular to the surface of the Mo core. In order to carry out this structural analysis, lamella preparation in a focused ion beam milling system was performed.

One drawback of the lamella preparation technique is the deposition of a Pt layer on top of the core-shell nanopillars. The use of a protective Pt layer has made the unambiguous structural characterisation of the boundaries of the nanopillars not possible. However, we suspect that the boundaries of the core-shell nanopillars have a large amount of exposed edges of MoS_2 layers due to the similarities of the shell growth to the growth of vertical MoS_2 nanosheets. One alternative route for structural characterization of the shell boundaries is to use ultrasonication to transfer the nanopillars onto a grid.

In Chapter 6, a nonlinear optical behaviour was observed in the core-shell Mo-MoS_2 nanopillars, which was enhanced from the response of nearby MoS_2 flakes. It is not yet clear how the specific geometry of the core-shell nanopillars improves the observed nonlinear response. Comparison of the response of the core-shell nanopillars with vertically grown MoS_2 nanosheets can elucidate the controllable tunability of the nonlinear optical response of MoS_2 nanostructures. In order to disentangle the nonlinear optical response of the core and the shell structures, nonlinear characterization should be carried out on Mo nanopillars.

Finally, we mention the potential application in hydrogen evolution reaction. The potential for hydrogen evolution reaction in other works on core-shell nanostructures based on transition metal dichalcogenides [6–8] has already been realized. The advantage of the core-shell geometry for hydrogen evolution reaction is attributed to the conductive core in combination with the catalytically active TMD shell. In this respect, the fabricated core-shell nanopillars in this work can be a promising candidate for hydrogen evolution reaction due to the combination of a metallic core *and* TMD shell with a large amount of exposed catalytically active edge structures. Similar to the nonlinear optical characterization, comparison of different nanopillar geometries with vertically grown nanosheets can elucidate the potential of core-shell nanopillars for hydrogen evolution reaction.

AB INITIO METHODS

The combination of atomic resolution transmission electron microscopy and monochromated electron energy loss spectroscopy makes it possible to correlate structural and electronic properties of nanomaterials. In recent years the use of monochromated elec-

tron energy loss spectroscopy[9] is increasing in popularity. As a consequence, further theoretical development is needed to correctly interpret the spectra acquired. One approach, which is used in this work, is to use ab initio methods to simulate energy loss spectra.

In Chapter 4 and Chapter 7 we used density functional theory as implemented in the WIEN2k package together with the *GW* approximation as implemented in the GAP2 code to interpret the energy loss spectra of the respective structures. We have seen good agreement of the ab initio calculations with the experimental results found in this work, however, as usual with numerical simulations, there always exists the possibility to improve on the precision and accuracy of the results.

We address here a few selected issues concerning the ab initio methods used in this work for future interpretation of monochromated electron energy loss spectra combined with atomic spatial resolution. One drawback of the WIEN2k package for calculating the dielectric response is that it neglects the local field effects, which can be quite important for nanostructures. Additionally, the long wavelength limit of the external perturbation is used, which is no longer a reasonable assumption for perturbations caused by a swift moving electron. Both of these limitations have to be addressed for accurate ab initio calculations for interpretation of energy loss in the electron microscope.

Another issue to be addressed is the addition of spatially resolved energy loss functions in *ab initio* methods. One final issue, which might be one that plagues all ab initio codes is known as the *tyranny of the scale*. The tyranny of scale here applies to the prohibitively large computational resources required to calculate realistic physical systems, such as systems with defects, monolayers of TMDs, or MoS_2 nanowalls. The issue of scale is one that hinders the calculations of realistic physical systems with many-body perturbation theory based on density functional theory, such as the GW approximation and solving the Bethe-Salpeter equations. As a consequence, *ab initio* methods to determine accurate band gaps and excitonic behaviour of these type of realistic physical systems might still be out of reach for the foreseeable future.

8

REFERENCES

[1] S. Susarla, A. Kutana, J. A. Hachtel, V. Kochat, A. Apte, R. Vajtai, J. C. Idrobo, B. I. Yakobson, C. S. Tiwary, and P. M. Ajayan, *Quaternary 2D Transition Metal Dichalcogenides (TMDs) with Tunable Bandgap,* Advanced Materials **29**, 1702457 (2017), https://www.onlinelibrary.wiley.com/doi/pdf/10.1002/adma.201702457 .

[2] Y.-C. Zou, Z.-G. Chen, S. Liu, K. Aso, C. Zhang, F. Kong, M. Hong, S. Matsumura, K. Cho, and J. Zou, *Atomic Insights into Phase Evolution in Ternary Transition-Metal Dichalcogenides Nanostructures,* Small **14**, 1800780 (2018), https://onlinelibrary.wiley.com/doi/pdf/10.1002/smll.201800780 .

[3] S. Franssila, *Introduction to Microfabrication, Second Edition* (Bantam, 2010).

[4] L. Xu, H. Gong, L. Deng, F. Long, Y. Gu, and J. Guan, *Complex-Mediated Synthesis of Tantalum Oxyfluoride Hierarchical Nanostructures for Highly Efficient Photocat-*

alytic Hydrogen Evolution, ACS Applied Materials & Interfaces **8**, 9395 (2016), pMID: 27010186, https://doi.org/10.1021/acsami.6b02622 .

[5] T. T. Tran, M. Gooch, B. Lorenz, A. P. Litvinchuk, M. G. Sorolla, J. Brgoch, P. C. W. Chu, and A. M. Guloy, *Nb$_2$O$_2$F$_3$: A Reduced Niobium (III/IV) Oxyfluoride with a Complex Structural, Magnetic, and Electronic Phase Transition,* Journal of the American Chemical Society **137**, 636 (2015), pMID: 25581015, https://doi.org/10.1021/ja511745q .

[6] Z. Chen, D. Cummins, B. N. Reinecke, E. Clark, M. K. Sunkara, and T. F. Jaramillo, *Core-shell MoO$_3$-MoS$_2$ Nanowires for Hydrogen Evolution: A Functional Design for Electrocatalytic Materials,* Nano Letters **11**, 4168 (2011), pMID: 21894935, https://doi.org/10.1021/nl2020476 .

[7] D. R. Cummins, U. Martinez, R. Kappera, D. Voiry, A. Martinez-Garcia, J. Jasinski, D. Kelly, M. Chhowalla, A. D. Mohite, M. K. Sunkara, and G. Gupta, *Catalytic Activity in Lithium-Treated Core-Shell MoO$_x$/MoS$_2$ Nanowires,* The Journal of Physical Chemistry C **119**, 22908 (2015), https://doi.org/10.1021/acs.jpcc.5b05640 .

[8] D. R. Cummins, U. Martinez, A. Sherehiy, R. Kappera, A. Martinez-Garcia, R. K. Schulze, J. Jasinski, J. Zhang, R. K. Gupta, J. Lou, M. Chhowalla, G. Sumanasekera, A. D. Mohite, M. K. Sunkara, and G. Gupta, *Efficient hydrogen evolution in transition metal dichalcogenides via a simple one-step hydrazine reaction,* Nature Communications **7**, 11857 (2016).

[9] J. A. Hachtel, A. R. Lupini, and J. C. Idrobo, *Exploring the capabilities of monochromated electron energy loss spectroscopy in the infrared regime,* Scientific Reports **8**, 5637 (2018).

A

GENERAL TIPS IN CLEANROOM NANOFABRICATION

In this appendix a few handy tips and practices for cleanroom work will be described. The tips and practices described here are a mixture of results found through trial and error and through conversations with other cleanroom users. Any specific fabrication project will have its subtleties and will require some degree of optimization, however it does not hurt to ask someone who might be doing something a bit similar and take that advice into account.

A.1. AMBIENT CONDITIONS

Maintaining a constant temperature and humidity in the cleanroom is crucial for the reproducibility and quality of fabricated nanostructures; the lifetime and usefulness of most resists depend heavily on these two parameters. A humidity level between 40% and 60 % should be maintained in order to use resists, with an ideal level in the 45%-50% range. A relatively high humidity (> 60%) usually leads to poor adhesion or cracking of the resists, which can be attributed to the hydrophobic nature of resists. Various aspects of nanofabrication depend on temperature, e.g. lift-off, resist storage, acid processing, to name a few. As such, it is important to be sure that the temperature of the fabrication process is consistent. Generally speaking, the wetbench area should have a working temperature around 20-25°C.

A.2. ELECTRON BEAM LITHOGRAPHY

A.2.1. BRIEF INTRODUCTION TO ELECTRON BEAM LITHOGRAPHY

In the past decades electron beam lithography (EBL) has emerged as a powerful tool to create structures to study properties at the nanoscale. One of the attractive features of EBL is its flexibility to create high quality structures from the micron range all the way down to sub-10nm structures. Electron beam lithography consists of exposing a electron sensitive polymer, termed "resist", to an electron beam. The exposed resist areas are chemically modified. The chemically modified sample can then be used for further processing. The shape of the pattern made with electron beam lithography can thus be easily changed by changing the path the electron beam traverses on the sample surface. The design can be made with several software packages, e.g. KLayout, or AutoCad. If one needs a bit more rigorous control of the specific shapes, it is also possible to create a design using Python.

A.2.2. CHOICE OF RESIST

Before choosing a resist, we still need to know what types of resists are available. There are two classes of electron beam resists that can be used. We speak of a negative-tone resist when the bonds of the polymer are strengthened at the exposed areas. The unexposed areas can be washed away by placing the sample in a solution, called the developer. The unexposed area can then be etched away in either a wet chemical etch or dry etch process.

Conversely, if the bonds are weakened at the exposed areas we speak of a positive-tone resist. In the case of a positive-tone resist, it is the exposed area that is washed away when the sample is placed in a developer solution. In this case, it is the exposed areas that can be etched away in a wet chemical etch or dry etch process. Alternatively, one

can deposit a material on top of the developed sample and use lift-off of the resist which then results in the deposited material remaining in the exposed area.

Ultimately, the choice of resists depends on the specific wishes of the user, e.g. structure width, thickness, complexity, or multiple lithography steps needed. As a rule of thumb, the size of the patterned structures depends on the thickness of the resist used; the thinner the resist, the smaller the structures that can be patterned. Quite often, resists come in various viscosities, resulting in different thicknesses of the resist after spincoating. Additionally, one needs to take into account the adhesion of a specific resist to the underlying material.

A.2.3. PROXIMITY EFFECT CORRECTION AND MULTIPASS LITHOGRAPHY

In order to improve the quality of the patterned structures one can employ proximity effect correction (PEC) and/or multipass electron beam lithography. We first start with the implementation of PEC.

In the case of PEC the goal is to correct for possible edge effects of a design, e.g. round or sharp corners; when exposing the sample the pattern generator exposes the selected area with the given exposure in the pattern generator software(cjob in this case). Unless otherwise instructed to, the pattern generator does not correct for forward or backscattering of electrons in your resist or substrate. Using PEC as implemented in the TRACER program from GenISys GmbH using a Monte Carlo approach. In the TRACER program, one can find a selection of resists and materials that are usually found in nanofabrication processes. In Fig A.1 the steps on how to create a specific stack of materials for the Monte Carlo simulation can be seen. We first start with choosing the materials to use, and their corresponding thicknesses. Afterwards, one can choose how many electrons should be considered in the simulation. After the simulation is finished, the user has the choice of either exporting the numerical result or a fitted Gaussian model for use in BEAMER. Implementation of the PEC is done by selecting the PEC module in BEAMER and creating the .gpf file of the desired design.

The goal of multipass electron beam lithography is to average out inherent instabilities in the pattern generation system during patterning, e.g. stage drift or beam fluctuations. The idea of multipass lithography is to expose the selected areas multiple times with a smaller exposure instead of a single exposure. A multipass process can be carried out in two ways in the Kavli Nanolab cleanroom. One can choose to expose the design multiple times in cjob, i.e. writing the desired design x times and choosing the exposure to be $\mu C/cm^2/x$. Alternatively, BEAMER has the option to implement multipass lithography in the .gpf file itself. In Fig A.2 the steps for implementing a multistep process in BEAMER can be seen. The use has the choice of carrying out 2 or 4 passes for exposure. Alternatively, the user can set a fixed exposure step value which a new pass will be carried out. In this case, the final exposure is set in cjob and cjob will calculate how many passes will be carried out when a specific exposure step is chosen, i.e. final exposure/exposure step.

A.3. INDUCTIVELY COUPLED PLASMA FOR REACTIVE ION ETCHING

A.3.1. CHOICE OF MATERIALS

Advantages of the use of an inductively coupled plasma for reactive ion etching (ICP-RIE) are such that one can create high aspect ratio structures in the material of choice. Quite often the materials silicon and silicon nitride are the ones etched in an ICP-RIE process. As this thesis has showed high aspect ratio structures are also possible in films of molybdenum, and to some degree, films of tungsten.

It is possible to etch high aspect ratio structures with an ICP-RIE due to the optimal concentration of ion species in the plasma and the directional bombardment designed into an ICP-RIE system. As a result, the etch rate of a material in an ICP-RIE system can be orders of magnitude higher than the etch rate in a RIE system. Additionally, the etch rates of different materials etched in the same ICP-RIE system can also differ by orders of magnitude, as this the case when comparing the etch rates of silicon($\sim \mu$m/minute) and molybdenum or tungsten ($\sim$100s nm/minute). One must think carefully of the different materials used If one wants to etch heterostructures in an ICP-RIE process.

A.3.2. ETCH RATE PARAMETERS

The etch rate parameters for materials like silicon or silicon nitride can be quite easily found in the literature. However, one should also be aware that different ICP-RIE systems might have different geometries for the process chamber. In general different chamber geometries lead to different etch rates for the same material when using the same etch parameters. However, one can think of using the etch rate of a different ICP-RIE system as a starting point for determination of the etch rate parameters for the ICP-RIE system being used.

One final note on the etch rate. It has been observed in the Kavli Nanolab cleanroom that the etch rates of materials in ICP-RIE systems tend to change suddenly, even after months or years of having a consistent etch rate. The sudden change in etch rate has been observed in different ICP-RIE systems, whether they are made from the same company or from different companies, and for different materials. The change in etch rate can be easily seen for ICP-RIE systems with a laser interferometry system. However, for systems without such a laser interferometry system, such as the Oxford Instruments PlasmaPro 100 Estrelas and the Adixen AMS 100 I-speeder, the change in etch rate is not so easily identifiable. In the case of a much higher etch rate one trick is to use a "sacrificial" sample and over-etch this sample. The over-etched sample can then be used as a reference to identify when the etch rate has become much higher.

B

On the use of Hydrogen Silsesquioxane for electron beam lithography

B.1. Brief Introduction to Hydrogen Silsesquioxane

Hydrogen Silsesquioxane (HSQ) is a negative tone resist that has been used as a type of "spin-on-glass" material due to its dielectric properties and excellent gap filling property. It is composed of H-Si-H and O-Si-O bonds which are ordered in a cage-like structure. Exposing the HSQ to electrons leads to the breaking of the weak H-Si bonds, eventually leading to the formation of Si-O bonds in the exposed area. The unexposed areas can be washed away with solutions containing TMAH, essentially forming nanostructures of SiO_2. With careful fabrication, sub-10 nm structures of HSQ can be fabricated onto the desired substrate. In addition to high spatial resolution, HSQ is also known for its high etch-resistance and stability in plasmas used in reactive ion etching systems making it ideal as a mask for high aspect ratio structures. However, HSQ remains a notoriously difficult resist to work with and the focus of this appendix is on the difficulties one can encounter when working with HSQ. The advice in this section consists partly from personal experience with HSQ and partly a summary of the literature which is available on HSQ, which can be found at the end of this section.

B.2. Using HSQ

HSQ, like other resists, is dissolved in a solution where the ratio of resist to solvent determines the thickness of the resist after spin-coating. It is possible to choose in which solvent the HSQ is dissolved. The first generation FOx-1x HSQ resists are dissolved in MIBK, while the second generation FOx-2x HSQ resists are dissolved in volatile methyl siloxane (VMS). This distinction in solvents is important if one wishes to use a multilayer resist system containing HSQ; other resists use MIBK as a developer, e.g. PMMA, so resist mixing can occur which can lead to undesired results. The layer thickness of HSQ after spin-coating can be anywhere from 120 nm to 900 nm, depending on the concentration of HSQ in the solvent. Be aware that the thicker the HSQ layer, the more difficult it becomes to develop the resist. TMAH containing developers, e.g. MF322, can be used for low concentrations of HSQ resist, however the thicker HSQ resists might need to be developed in 25% TMAH solution. The ideal developer ultimately depends on your process and surface of the substrate.

In the case of the FOx-1x series a thinner layer of HSQ can be spin-coated by diluting the FOx-1x resist in MIBK. Note that the HSQ should be diluted in teflon beakers as the HSQ will leave residues in glass beakers which cannot be removed. The teflon beakers can be cleaned by a short HF dip. The HSQ is stored in 5 mL bottles in liquid nitrogen, and to use a bottle on should ask Eugene Straver for a bottle. The bottles are placed inside a fridge after they are taken out of the liquid nitrogen. It is advised to let the HSQ warm up to room temperature after taking it out of the fridge, usually leaving the HSQ bottle for at least 30 minutes in a beaker in the HSQ spin-coating wetbench is sufficient.

After the HSQ is warmed up, it can be poured into a syringe and it is advised to let a few droplets flow outisde of the syringe to make sure there are no bubbles in the resist, this is especially useful when using the thicker HSQ resists.

After spin-coating the further process steps, (exposure, development, etching), should be done as soon as possible. The exposure should happen immediately after spin-coating. Likewise, the development should happen immediately after exposure. Ideally, the sam-

ple should be etched in a reactive ion etching plasma procedure on the same day as the previous lithography steps. However, it is still possible to carry out the etching 3 days after exposure and development, but not 5 days after exposure!

Removing the remaining HSQ can be done in a similar fashion to the removal of SiO_2. Reactive ion etching in carbon containing etch chemistries, e.g. CF_4 or CHF_3, will remove the remaining HSQ. Another way to remove the remaining HSQ is by a dip in HF or buffered HF. In both cases one should be aware that the patterned structure can also be damaged by the reactive ion etching or HF dip. In the case of Mo and W nanostructures, a 40% HF dip is too agressive, and a diluted 5% HF concentration gave the best results.

B.3. RESIST LIFETIME

Arguably the main cause of difficulties with HSQ is its relatively short lifetime. The short lifetime can be traced back to the reabsorption of H into the treated HSQ, leading to the loss of sharp features, lower etch resistance, lower adhesion, and less stability while using reactive ion etching. In the Kavli Nanolab the HSQ is stored in liquid nitrogen, and when needed, a 5 mL bottle is taken out of the liquid nitrogen for use. The storage in liquid nitrogen can dramatically increase the shelf lifetime of the resist up to 1.5 years, compared to a couple of months when not stored in liquid nitrogen. It can occur that the HSQ might give good results one week, while the results of the HSQ after week that can all be immediately and significantly worse.

To be clear, the shelf lifetime mentioned above refers to the moment that the resist arrived to the lab for use until the moment that the resist consistently gives bad results after use in electron beam lithography. This distinction is made to compare with the "out-of-the-liquid-nitrogen" lifetime of the HSQ. It was found that the best structures are produced when using HSQ that was immediately taken out of the liquid nitrogen. However, after 3 weeks of taking the resist out of the liquid nitrogen the quality of the structures sharply decreases.

B.4. ADHESION

Adhesion of resists to surfaces is a general concern in electron beam lithography. In the case of HSQ the adhesion is the best when applying the HSQ to Si substrates. The native oxide formed on the Si helps with the adhesion of the HSQ onto the Si, and this adhesion is further improved due to the electron exposure. However, adhesion to other substrates can be problematic, especially in the case of metal substrates. One way to bypass the adhesion problem is to evaporate HMDS onto the substrate before spin-coating the HSQ. Alternatively, one can also use the fact that HSQ has good adhesion to SiO_2; if the fabrication process allows it, one can deposit a thin layer of SiO_2 either with PECVD or sputter-deposition onto the substrate before spin-coating the HSQ.

Finally, it should be noted that adhesion of the HSQ to the substrate becomes worse as the resist reaches its shelf lifetime, especially in the case of Mo and W and presumably other metals.

B

B.5. Etch Resistance

As was mentioned above, the etch resistance of HSQ in reactive ion etching procedures is one of the reason for its continued use in electron beam lithography. In the case of Si, aspect ratios as high as 1:24 can be achieved in CHF_3/O_2 etch chemistries. HSQ is particularly etch resistant in pure O_2 plasmas, making it ideal as a mask for organic resists if one wants to make a bilayer HSQ/organic resist system. In the case of more aggresive etch chemistries like the ones used in this thesis, the selectivity of the HSQ with respect to the metal is not particularly large. However, as of writing, a resist that can withstand the etch chemistry needed for the metal etching has not been found.

As was mentioned above, the etch procedure with HSQ should be done as close as possible to the exposure and development step of HSQ. It was found that etching a sample 5 days after exposure and development led to poor results. As of writing, having a 3 day period between development and etching of the sample still gave good results.

C

WORKING WITH A HIGH PERFORMANCE COMPUTING CLUSTER

C.1. BRIEF INTRODUCTION TO HIGH PERFORMANCE COMPUTING

It is safe to assume that the reader has in their pocket what a person in the 1960's would call a supercomputer. Current smartphones have the memory and computing power that would fill entire rooms a few decades ago. Recent advances in computing power and algorithms have made it possible to tackle computational problems which were untenable a few decades ago. However, with great computing power comes great confusion on how to use said computing power, at least when it comes to the author of this thesis. The goal of this section is to give a few tips on how to work with high performance computing clusters (HPC), and how to tackle possible pitfalls when carrying out large-scale calculations.

For what follows we assume the use of a Linux based system. HPC consists of multiple computers connected to each other to form a network, where each computer can be considered a **node**. The idea is to tackle large computational problems with a large amount of computers, what is termed **parallel computing**. Communication between the nodes depends on the type of connections between the nodes. Cables connecting nodes usually consist of **ethernet** cables or **infiniband** cables. We will not go into much detail about these different types of cables. The important thing to remember is that infiniband cables support larger data volume and fast communication between different nodes compared to ethernet cables. This distinction can be useful if one is carrying out a calculation that cannot be easily split among nodes. We speak of a **homogeneous** computing cluster when all the nodes consists of the same type of hardware and connections, and a **heterogeneous** computing cluster when different types of compute nodes and/or connections are used.

The hierarchy of a computing cluster can be split into a **master** node and **worker** node. A user usually logs onto the computing cluster into the master node. It is in the master node that a user can submit jobs for the worker nodes to carry out. The resources of a computing cluster is usually managed by a resource manager software package. In the case of the HPC05 computing cluster, PBS/torque resource manager is used. The Cartesius supercomputer facility at Surfsara uses the SLURM resource manager. The use of different resource managers usually has the effect that a different job submission script is needed to start a calculation.

C.2. THE IMPORTANCE OF PROPER PACKAGE USE

Installing software packages onto a computer cluster is not a trivial matter, since most users do not have administrator privileges. A lack of administrator privileges has a consequence that the "sudo apt-get" command cannot be used for easy installation of a software package onto the cluster. In such a case, the user needs to manually install all the auxiliary packages needed for a specific software package. Quite often one can find different versions of the same package, so care is needed to install the correct package versions. It is also important that the packages also be compiled with the same compilers. It can happen that compiling different auxiliary packages with different compilers can lead to no errors when compiling and installing the software package needed for the required calculation. However, when performing the actual calculations the software

package can stay stuck at a specific point of the calculation, this can be due to slightly different definitions of function between different versions of compilers. In some cases, it also necessary to know the specific hardware being used in order to set the proper flags when compiling and installing packages.

C

D

PRACTICAL CONSIDERATIONS FOR DENSITY FUNCTIONAL THEORY CALCULATIONS

D.1. Introduction

In chapter 2 we briefly discussed the formalism of density functional theory(DFT) and the *GW* approximation. In this appendix we will go more into detail on how the DFT calculations are carried out in the WIEN2k package[21]. Topics that will be discussed are the determination of the atomic models used in this work, k-point convergence, calculations of the density of states, determining the band structure, and calculation of the energy loss function. At the end of this appendix highlight possible roadblocks one might encounter while carrying out the DFT calculations.

D.2. The Self-Consistent Field Cycle in WIEN2k

D.2.1. Structure determination

The first step into understanding the system of study is to actually define the system. We need to define the system geometrically, i.e. the amount of atoms, the atomic coordinates, and the type of crystal. The geometrical configuration of the system of interest in WIEN2k is saved in type.struct files, where 'type' is the name of a system e.g. CO_2.struct. The WIEN2k software has a package, named StructGen, wherein it is possible to define the system by specifying the amount of atoms in the unit cell, distances, angles, and symmetry group. The StructGen package is rather limited to unit cells of bulk systems. More sophisticated structures, *supercells*, with e.g. defects, impurities, or surfaces effects, can be generated with the structeditor WIEN2k package. The structeditor package is interfaced with Octave, an open source version of Matlab. The atomic structures can be visualized with the XCRYSDEN[34]. Other programs such as Rhodius from the University of Cadíz and VESTA[1] can also be used to create and visualize unit cells and supercells. One problem encountered with supercells created with Rhodius is that WIEN2k gives rounding errors for large supercells. Large supercells created with Rhodius tend to be problematic with WIEN2k due to rounding errors of the positions of the atoms. The rounding errors problem can be solved by adjusting the tolerance level in WIEN2k. WIEN2k(and other DFT codes) carry out their calculations in reciprocal space. The calculations in reciprocal space come as a natural consequence of the periodicity of the crystals studied with DFT codes.

D.2.2. Convergence criteria

After determining the structure we need to specify the amount of k-points needed, the atomic radii, and the separation energy of core and valence electrons. The use of k-points is due to the reciprocal lattice calculation mentioned above. The amount of k-points needed depends on the type of material being used (metal, semiconductor, insulator), and on the size of the unit cell. When carrying out calculations with metals a large amount of k-points are needed(1000-10000's k-points), while less k-points are needed for semiconductors(100-1000's), and even less for insulators(1-10 k-points). The atomic radii should be chosen such that the atomic spheres are touching, but not overlapping. The atomic radius is chosen by setting a value of "RKmax" in WIEN2k. RKmax is the product of the smallest atomic sphere radius times the largest k-vector of the plane wave expansion of the wave function. The size of the basis set is determined by RKmax, while the calculation time depends on both RKmax and the amount of k-points used. Accurate

results can be acquired by increasing the amount of k-points and RKmax and afterwards calculate some physical properties (band structure, density of states, EELS) until these physical properties do not change significantly from one calculation to the other.

The orbitals generated by WIEN2k need to have the correct electron density in order to describe a physically realistic system. Core state electrons are bound states and as a consequence the orbitals associated to core states should not have charge leakage outside of the atomic sphere. As a rule of thumb, the charge associated with core states should be between 97% to 100% inside the atomic sphere. The situation is different for valence electrons, which have a much larger degree of delocalization as compared to core electrons. The distinction between core and valence states can be done by specifying a cutoff energy at which electrons can be considered to be of the core or valence type. By default the energy seperation is set to 13.61 eV. The WIEN2k code willl give a warning if charge is leaking from the core states. However, the warning does not automatically lead to the code crashing and unphysical results can be a consequence of a calculation. The amount of charge leakage from the core states need to be carefully checked before concluding if a calculation gives real physical results.

D.3. LATTICE PARAMETERS DETERMINATION

D.3.1. VOLUME OPTIMIZATION

One can begin with using the experimentally measured values for the lattice parameters to define the locations of the atoms in the unit cell. Lattice parameters close to literature values are quite consistenly found with DFT calculations[21][2]. Volume optimization and internal structure optimization can be carried out in order to acquire the correct theoretical equilibrium lattice parameters in order to qualitatively and quantitatively compare with experiments. One way of finding the optimized volume is by minimizing the equation of state as in [36][35], where the energy E of a crystal at a volume V is given by:

$$E(V) = E_0 + \frac{K_0 V}{K_0'} \left(\frac{(V_0/V)^{K_0'}}{K_0' - 1} + 1 \right) - \frac{K_0 V_0}{K_0' - 1} \tag{D.1}$$

where K_0 is the modulus of incompressibility, and K_0' is its first derivative with respect to pressure. V_0 is the equilibrium volume, and E_0 is the equilibrium energy of a crystal. The approach taken is this work is to vary the unit cell volume until a minimum in the total energy of the system is found with respect to the unit cell volume. The unit cell with minimum energy is taken as the equilibrium unit cell, which is subsequently used for further calculations in the equilibrium(non-strained) state. One way this can be done is by increasing the total volume of the unit cell, while keeping the a:b:c ratio constant. The optimized volume can then be used to optimize the c/a ratio. Alternatively, one can also vary the c/a ratio while keeping the volume constant.

D.3.2. FORCE OPTIMIZATION

Volume optimization of a crystal concerns the calculation of the lattice parameters which minimizes the equation of state Eq. D.1. Additionally, in WIEN2k one can use internal

force optimization of the atoms in the unit cell to acquire the correct internal coordinates. Force optimization is another step of optimization that is carrried out in a similar matter as the volume optimization calculations that were discussed in the previous section. The electronic structure of MoS_2 is highly sensitive to the internal atom coordinates and interlayer distance. Applying strain or an electric field can lead to large changes in the interlayer distance and internal atomic coordinates [37] [38] [39] [40].

D.3.3. NONLOCAL VAN DER WAALS INTERACTION IN WIEN2K
The transition metal dichalcogedides are layered materials, whose van der Waals interaction is of significance for determining their physical properties, as we have seen in this thesis. In this work we have chosen to use the implementation of a non-local van der Waals functional, as implemented in WIEN2k. We choose the van der Waals functional optB88-vdW as this gives reliable results for layered solids [32]. In the WIEN2k implementation care needs to be taken such that a smooth density ρ_s is defined as

$$\rho_s(\mathbf{r}) = \begin{cases} \rho(\mathbf{r}), & \rho(\mathbf{r}) \le \rho_c \\ \frac{\rho(\mathbf{r}) + A\rho_c(\rho(\mathbf{r}) - \rho_c)}{1 + A(\rho(\mathbf{r}) - \rho_c)}, & \rho(\mathbf{r}) > \rho_c \end{cases} \tag{D.2}$$

where $A = 1$ bohr^3. For a specific ρ_c, a plane-wave expansion cutoff G_{max} also needs to be chosen. Different ρ_c and G_{max} values were studied in [31] and [32], and reasonable values found are $\rho_c = 0.3$ bohr^{-3} at a plane-wave expansion cutoff $G_{max} = 20$ bohr^{-1} gives reliable results. We chose these values for calculations including van der Waals interactions in this work.

D.3.4. DENSITY OF STATES CALCULATION
The density of states (DOS) is calculated in WIEN2k after a well-converged SCF calculation has been carried out. A finer k-mesh is needed for the DOS, so usually one increases the amount of k-points and runs lapw1 with the finer k-mesh to acquire the wavefunctions and energies of the system of interest. Afterwards, the script lapw2 with the "qtl" option can be run to acquire densities and partial density of states to study properties like specific orbital (s,p,d) dependence of specific atoms in the system of interest.

D.3.5. BAND STRUCTURE
To calculate the band structure of materials a specific path in the Brillouin zone needs to be chosen. In the literature there are standard high symmetry points that are usually used for such band structure plots. However, one has a lot of freedom to choose which path one is interested in. After choosing the path, the amount of k-points along a path needs to be chosen. Note that the amount of k-points along a path is not neccesarily the same as the amount of k-points used in a different calculation, e.g. a DOS calculation. It can occur that the amount of k-points chosen for a path is much larger than in a DOS calculation, leading to slightly different band gap values in the case of semiconductors and insulators. A path can be chosen by loading the case.struct file of interest into the XCRYSDEN visualization package. With XCRYSDEN the amount of k-points can be chosen along the path of choice. After choosing a path, run lapw1. The script lapw2 needs to

be run with the "qtl" and "band" switches. Afterwards,one can use the "spaghetti" script to calculate the band structure, while also using

D.3.6. OPTICAL PROPERTIES

Optical properties are calculated in WIEN2k with the optic package. The optic package calculates linear optical properties of solids in the Random Phase Approxiation (RPA). After choosing a finer k-mesh, one can rerun lapw1 and afterwards lapw2 with the "-fermi" switch to generate the weight file for the different bands in the calculation.

After running lapw2, the script "optic" generates the momentum matrix elements for the different bands for each k-point combination. After using optic, the results fed into the "joint" script to calculate the imaginary part of the dielectric function by carrying out the Brillouin zone integration. The function "kram" can be used to calculate the real part of the dielectric function, along with the energy loss function, absorption spectrum, and refractive indices. Additionally, Gaussian broadening and a scissor operator can be used with the kram script.

D.4. GW APPROXIMATION CONSIDERATIONS

D.4.1. GW APPROXIMATION IN WIEN2K

We use the output of WIEN2k SCF calculations as the input for the *GW* approximation calculations. It is important that well-converged DFT calculations are used for the input of the *GW* calculations. To carried out different k-point convergence tests for the DFT calculations before continuing with the *GW* calculations. This is done on an equally spaced k-mesh where quasi-particle energies are calculated. However, for physical properties like the density of states and energy loss function, a denser k-mesh is needed with k-points that were not considered in the original *GW* calculation. The C-shell scripts *gap2_analy* and *gap2_gwnvf* are used to acquire quasi-particle energies using Fourier interpolation method for the k-points not considered in the original *GW* calculation. The output of these scripts are case.vector and case.energy files that can then be used for further calculations. In the case of the density of states and band structure, the *gap2_analy* script has the option to directly carry out these calculations. For the band structure, a standard path in the Brillouin zone is chosen with the quasi-particle corrected energies. One can choose a different path in the Brillouin zone by using xcrysden to create a different case.klist_band file. Using the command

"gap2_analy -f casefile -gwdir /PATH/gw_case_directory -t dos/band -gwtag (the type of approximation, *GW*, G_0W_0, etc) -gw (gap2c.x or gap2c-mpi.x) -nkp (#number of k-points)"

The use of the script gap2_gwnvf can also be used with the above command without the "-t dos/band" tag.

D.4.2. ENERGY LOSS FUNCTION IN THE GW APPROXIMATION WITH WIEN2K

For the energy loss function the dielectric function needs to be calculated. This is done in principle within the *GW* approximation to acquire the dynamical Coulomb potential

W. A few more steps are needed to use the results of the *GW* calculations for the optical properties calculations in the optic package. Namely, after using either *gap2_analy* or *gap2_gwnvf* the files with the quasi-particle energies are stored in case.vector_GW and case.energy_GW. These files are needed for the optic calculations and need to be renamed as case.vector and case.energy. Furthermore, there are an additional number of files that need to be renamed in order to carry out the calculations with optic. All of the files that need to be renamed in order to carry out calculations with optic are:

- case.clmsum_gw -> case.clmsum

- case.klist -> case.klist

- case.kgen-dos -> case.kgen

- case.energy_GW-dos -> case.energy

- case.energyso_GW-dos -> case.energyso when including spin-orbit coupling

- case.in1_gw -> case.in1 (or case.in1c_gw -> case.in1c in the case without inversion symmetry)

- case.vector_GW-dos -> case.vector

- case.vectorso_GW-dos -> case.vectorso when including spin-orbit coupling

- case.scf1-dos -> case.scf1

- case.scf2_GW-dos -> case.scf2

- case.r2v_gw -> case.r2v

- case.vns_gw -> case.vns

- case.vsp_gw -> case.vsp

Afer renaming these files, the calculations with the optic package can resume as in the case without the *GW* calculations.

D.5. Troubleshooting

When encountering problems while carrying out a calculation with WIEN2k, the first step is to check if all the parameters or files are correct. If the problem persists, WIEN2k has an extensive mailing list and clever use of keywords can be used to find an issue raised by another use which is similar to the issue at hand. Here we mention some issues encountered in this work and possible solutions. In the case of the crystal structures of WS_2 a problem was encountered for the 3R structure. Namely, the SCF cycle would immediately crash for calculations with the 3R structure. The issue is due to the 3R structure itself with different versions of WIEN2k and the intel fortran compilers. The calculations would crash when the 2017 intel fortran compilers were used with any version of WIEN2k. Switching to the 2016 intel fortran compilers resulted in working SCF calculations for the 2017 and 2018 versions of WIEN2k, but not the 2019 WIEN2k version. The reason why the 3R calculations crashed for the 2017 fortran compilers and 2019 WIEN2k versions is not yet known. The takeaway message is that it is useful to

have older versions available to check if certain calculations crash due to changes made between compiler and package versions.

REFERENCES

[1] K. Momma and F. Izumi *VESTA 3 for three-dimensional visualization of crystal, volumetric, and morphology data*, J. Apply. Cryst. (2011), 44, 1272-1276, https://doi.org/10.1107/S0021889811038970

[2] C. Espejo T. Rangel, A.H. Romero, X. Gonze, G.-M Rignanese *Band structure tunability in MoS$_2$ under interlayer compression: A DFT and GW study*, Physical Review B **87**, 245114 (2013)

[3] B. Schonfeld, J.J. Huang, S.C. Moss *Anisotropic mean-square displacement (MSD) in single crystals of 2H- and 3R-MoS$_2$*, Acta Crystallographica B39 (1983), 404-407

[4] J. Gusakova, Z. Wang, L. Lynn Shiau, A. Krivosheeva, V. Shaposhnikov, V. Borisenko, V. Gusakov, B. Kang Tay *Detailed Photocurrent Spectroscopy of the Semiconducting Group VI Transition Metal Dichalcogenides*, J. Phys. Chem. 1982, 86, 463-467

[5] K.F. Mak, C. Lee, J. Hone, J. Shan, T.F. Heinz *Atomically Thin MoS$_2$: A New Direct-Gap Semiconductor*, Physical Review Letters **105**, 136805 (2010)

[6] M.M. Glazov, T. Amand, X. Marie, D. Lagarde, L. Bouet, and B. Urbazek *Exciton fine structure and spin decoherence in monolayers of transition metal dichalcogenides*, Physical Review B **89**, 201302(R) (2014)

[7] M.T. Rivas, L. Maduro, M. Masaki, E. Okunish, and S. Conesa-Boj *Strain-dependent Edge Structures in MoS$_2$ Layers*, Nano Letters, 17, 7021 (2017)

[8] M.V. Bollinger, J.V. Lauritsen, K.W. Jacobsen, J.K. Nørskov, S. Helveg, and F. Besenbacher *One-Dimensional Metallic Edge States in MoS$_2$*, Physical Review Letters **87**, 196803 (2001)

[9] X. Qian, J. Liu, L. Fu, and J. Li *Quantum spin Hall effect in two-dimensional transition metal dichalcogenides*, Science 20 Nov 2014

[10] H. Xu, S. Liu, Z. Ding, S.J.R. Tan, K.M. Yam, Y. Bao, C.T. Nai, M. Ng, J. Lu, C. Zhang, and K.P. Loh *Oscillating edge states in one-dimensional MoS$_2$*, Nature Communications DOI: 10.1038/ncomms12904

[11] X. Fan, D.J. Singh, and W. Zheng *Valence Band Splitting on Multilayer MoS$_2$: Mixing of Spin-Orbit Coupling and Interlayer Coupling*, The Journal of Physical Chemistry 2016, 7, 2175-2181

[12] F. Hüser, T. Olsen, and K.S. Thygesen *How dielectric screening in two-dimensional crystals affects the convergence of excited-state calculations: Monolayer MoS$_2$*, Physical Review B **88**, 245309 (2013)

[13] J. Xiao, M. Zhao, Y. Wang, and X. Zhang *Excitons in atomically thin 2D semiconductors and their applications*, Nanophotonics DOI 10.1515/nanoph-2016-0160

D

[14] S.R. Park and C. Kim *Microscopic mechanism for the Rashba spin-band splitting: Perspective from formation of local orbital angular momentum*, Journal of Electron Spectroscopy and Related Phenomena 201 (2015) 6-17

[15] S.M. Kochm M. Kira, G. Khitrova, and H.M. Gibbs *Semiconductor excitons in new light*, Nature materials VOL 5, july 2006

[16] G.D. Scholes and G. Rumbles *Excitons in nanoscale systems*, Nature materials VOL 5, september 2006

[17] K.S. Thygesen *Calculating excitons, plasmons, and quasiparticles in 2D materials and van der Waals heterostructures*, 2D materials **4** (2017) 022004

[18] T. Olsen, S. Latini, F. Rasmussen, and K.S. Thygesen *Simple Screened Hydrogen Model of Excitons in Two-Dimensional Materials*, Physical Review Letters **116** 056401 (2016)

[19] P. Puschnig and C. Ambrosch-Draxl *Optical absorption spectra of semiconductors and insulators including electron-hole correlations: An ab-initio study within the LAPW method*

[20] R. Laskowski and N.E. Christensen *Ab initio calculations of excitons in AlN and Elliott's model*, Physical Review B **74**, 075203 (2006)

[21] K. Schwarz P. Blaha *Solid state calculations using WIEN2k*, Computational Materials Science 28 (2003) 259-273

[22] C Ambrosch-Draxl J. O. Sofo *Linear optical properties of solids within the full-potential linearized augmented planewave method* Computer Physics Communications 175 (2006) 1-14

[23] C. Hébert *Practical aspects of running the WIEN2k code for electron spectroscopy*, Micron 38 (2007) 12-28

[24] R.J. Nicholls and A.J. Scott *Practical approaches to the accurate modelling of EELS edges using Density Functional Theory*, Journal of Physics: Conference Series **126** (2008) 012038

[25] J.A. Camargo-Martìnez and R. Baquero *Performance of the modified Becke-Johnson potential for semiconductors*, Physical Review B **86**, 195106(2012)

[26] J.A. Camargo-Martìnez and R. Baquero *The band gap problem: the accuracy of the Wien2k code confronted*, arXiv:1208.2057v2 [cond-mat.str-e] 17 Jun 2013

[27] D. Koller, F. Tran, and P. Blaha *Improving the modified Becke-Johnson exchange potential*, Physical Review B **85**, 155109 (2012)

[28] K.E. Riley, M. Pitoňák, P. Jurečka, and P. Hobza *Stabilization and Structure Calculations for Noncovalent Interactions in Extended Molecular Systems Based on Wave Function and Density Functional Theories*, Chem. Rev. 2010, 110, 5023-5063

[29] K. Berland, V.R. Cooper, K. Lee, E. Schröder, T. Thonhauser, P. Hyldgaard, and B.I. Lundqvist *van der Waals forces in density functional theory: a review of the vdW-DF method*, Reports on Progress in Physics **78** (2015), 066501

[30] M. Dion, H. Rydberg, E. Schröder, D.C. Langreth, and B.I. Lundqvist *van der Waals Density Functional for General Geometries*, Physical Review Letters, Volume 92, Number 24, 2004

[31] D.C. Langreth, B.I. Lundqvist, S.D. Chakarova-Käck, V.R. Cooper, M. Dion, P. Hyldgaard, A. Kelkkanen, J. Kleis, L. Kong, S. Li, P.G. Moses, E. Murray, A. Puzder, H. Rydberg. E. Schröder, and T. Thonhauser *A density functional for sparse matter*, Journal of Physics: Condensed Matter **21** (2009) 084203

[32] F. Tran, L. Kalantari, B. Traoré, X. Rocquefelte, and P. Blaha *Nonlocal van der Waals for solids: Choosing an appropriate one*, Physical Review Materials **3**, 063602 (2019)

[33] F. Tran, J. Stelzl, D. Koller, T. Ruh, and P. Blaha *Simple way to apply nonlocal van der Waals functionals within all-electron methods*, Physical Review B **96**, 054103 (2017)

[34] A. Kokalj *Computer graphics and graphical user interfaces as tools in simulations of matter at the atomic scale* Comp. Mater. Sci., 2003, Vol. 28, p. 155

[35] Alberto Ajurrat Ascunce *Quantitative methods for electron energy loss spectroscopy*, PhD thesis, Universitat de Barcelona

[36] D.M. Teter, G.V. Gibbs, M.B. Boisen, D.C. Allan, M.P. Teter *First-principles study of several hypothetical silica framework structures*, Physical Review B **52**, 8064-8073 (1995)

[37] H. Peelaers, C.G. Van de Walle *Effects of strain on band structure and effective masses in MoS_2*, Physical Review B **86**, 241401 (2012)

[38] E. Scalise, M. Houssa, G. Pourtois, V. Afanas'ev, A. Stesmans *Strain-Induced Semiconductor to Metal Transition in the Two-Dimensional Honeycomb Structure of MoS_2*, Nano Res. 2012, 5(1): 43-48

[39] W.S. Yun, S.W. Han, S.C. Hong, I.G. Kim, J.D. Lee *Thickness and strain effects on electronic structures of transition metal dichalcogenides: 2H-MX_2 semiconductors (M= Mo, W; X= S, Se, Te)* , Physical Review B **85**, 033305 (2012)

[40] A. Ramasubramaniam, D. Naveh, E. Towe *Tunable band gaps in bilayer transition-metal dichalcogenides* , Physical Review B **84**, 205325 (2011)

[41] K. Jorissen *The ab initio calculation of relativistic electron energy loss spectra*, PhD Thesis, Universiteit Antwerpen 2007

[42] S. Woo, H.C. Par, and Y.W. Son *Poisson's ratio in layered two-dimensional crystals*, Physical Review B **93**, 075420 (2016)

D

[43] Z. Y. Zhu, Y.C. Cheng, U. Schwingenschlögl *Observation of monolayer valence band spin-orbit effect and induced quantum well statesin MoX$_2$*, Nature Communications DOI: 10.1038/ncomms5673

[44] X. Fan, W.T. Zheng, D.J. Singh *Nature of Valence Band Splitting on Multilayer MoS$_2$*, Physical Review B **84**,153402 (2011)

[45] Z. Y. Zhu, Y.C. Cheng, U. Schwingenschlögl *Giant spin-orbit-induced spin splitting in two-dimensional transition-metal dichalcogenide semiconductors*, arXiv:1509.06118

[46] A. Molina Sánchez *Effect of spin-orbit interaction on the optical spectra of single-layer, double-layer, and bulk MoS$_2$*

[47] M.G. Bell, W.Y. Liang *Electron energy loss studies in solids; The transition metal dichalcogenides*, Advances in Physics, 1976, Vol. 25, No. 1, 53-86

[48] W.Y. Liang, Sl.L. Cundy *Electron energy loss studies of the transition metal dichalcogenides*, Philosophical Magazine, 19:161, 1031-1043

[49] K. Zeppenfeld *Electron Energy Losses and Optical Anisotropy of MoS$_2$ single crystals*, Optics Communications Volume 1, number 8, 1970

[50] A. Kumar, P.k. Ahluwalia *Tuneable dielectric response of transition metal dichalcogenides MX$_2$ (M = Mo, W; X = S, Se, Te): Effect of quantum confinement*, Physica B **407** (2012) 4627-4634

[51] P. Johari, V. B. Shenoy *Tuneable Dielectric Properties of Transition Metal Dichalcogenides*, ACS Nano Vol. 5, No. 7, 5903-5908, 2011

[52] D. B. Williams, C. B. Carter *Transition Electron Microscopy, Second Edition*

[53] H. Raether , Springer Tracts in Modern Physics 88

[54] W. Wang, C. Yang, L. bai, M. Li, W. Li *First-Principles Study on the Structural and Electronic Properties of Monolayers MoS$_2$ with S-vacancy under Uniaxial Tensile Strain*, Nanomaterials 2018, **8**, 74

[55] I.A. Rahmanm, A. Purqon *First Principles Study of Molybdenum Disulfide Electronic Structure* J, Phys.L Conf. Ser. **877** 012026

[56] M. Kan, J.Y Wang, X.W. Li, S.H. Zhang, Y.W. Li, Y. Kawazoe, Q. Sun, P. Jena *Structures and Phase Transition of a MoS$_2$ Monolayer* The Journal of Physical Chemistry 2018, 118, 1515-1522

[57] S. Ahmad, S. Muhkerjee *A Comparative Study of Electronic Properties of Bulk MoS$_2$ and Its Monolayer Using DFT Technique: Application of Mechanical Strain On MoS$_2$ Monolayer* Graphene, 2014, 3, 52-59

[58] M. Sharma, P. Jamdagni, A. Kumar, P.K. Ahluwalia *Electronic and dielectric properties of MoS$_2$-MoX$_2$ heterostructures* AIP Conference Proceedings 1661, 080028 (2015)

[59] E. Scalise, M. Houssa, G. Pourtois, V. Afanas'ev, A. Stesmans *Strain-Induced Semiconductor to Metal Transition in the Two-Dimensional Honeycomb Structure of MoS$_2$* Nano Res. 2012, 5(1):43-48

D

CURRICULUM VITÆ

Louis Arcolino MADURO

04-10-1990   Born in Aruba

EDUCATION

2003–2009   Voortgezet Wetenschappelijk Onderwijs
Colegio Arubano, Aruba

2009–2013   Bachelor of Science in Physics
Universiteit Leiden, Leiden, The Netherlands

Thesis: Multifrequency EPR on Titanium Oxides Mixtures and on the $Fe(O,S)_3$ complex
Supervisor: Prof. dr. E. Groenen

2013–2016   Master of Science in Experimental Physics
Universiteit Leiden, Leiden, The Netherlands

Thesis: Cotunneling with energy-dependent contact transmission
Supervisor: Prof. dr. ir. S.J. van der Molen

Thesis: Towards current-induced magnetization switching with a 100% spin-polarized current
Supervisor: Prof. dr. J. Aarts

2017–2021   Ph.D. Physics
Delft Univeristiy of Technology, Delft, The Netherlands

Thesis: An Edgy Journey with Transition Metal Dichalcogenides: From Flakes to Nanopillars
Promotors: Prof. dr. L. Kuipers and Dr. S. Conesa-Boj

LIST OF PUBLICATIONS

9. A. Brokkelkamp, J. ter Hoeve, I. Postmes, S. van Heijst, **L. Maduro**, A. Davydov, S. Krylyuk, J. Rojo, S. Conesa-Boj *EELS-based spatially-resolved determination of the bandgap and dielectric function in nanomaterials* (In preparation) (2021)

8. **L. Maduro**, S. van Heijst, H. Jiang, S. Conesa-Boj *First-principles calculation of the opto-electronic properties of polytypic WS$_2$* (In preparation) (2021)

7. **L. Maduro**, M. Noordam, M. Bolhuis, L. Kuipers and S. Conesa-Boj *Position-Controlled Fabrication of Vertically-Aligned Mo-MoS$_2$ Core-Shell Nanopillar Arrays* (Under review) (2021)

6. **L. Maduro**, C. de Boer, M. Zuiddam, E. Memisevic, S. Conesa-Boj *Molybdenum nanopillar arrays: Fabrication and Engineering* Physica E: Low-Dimensional Systems and Nanostructures, 114903 (2021)

5. S. van Heijst, M. Mukai, E. Okunishi, H. Hashiguchi L. Roest, **L. Maduro**, J. Rojo, S. Conesa-Boj *Illuminating the electronic properties of WS$_2$ polytypism with electron microscopy* Annalen der Physik **18**, 639 (2021)

4. L.I. Roest. S.E. van Heist, **L. Maduro**, J. Rojo, S. Conesa-Boj *Charting the low-loss region in electron energy loss spectroscopy with machine learning*, Ultramicroscopy **18**, 639 (2021)

3. M. Tinoco[†], **L. Maduro**[†], S. Conesa-Boj *Metallic edge states in zig-zag vertically-oriented MoS$_2$ nanowalls*, Scientific Reports **9**, 15602 (2019).

2. M. Tinoco, **L. Maduro**, M. Masaki, E. Okunishi, S. Conesa-Boj *Strain-Dependent Edge Structures in MoS$_2$ Layers*, Nano Letters **17**, 70217026 (2017)

1. S. Blok, R.R. Agundez Mojarro, **L. Maduro**, M. Blaauboer, S.J. Van Der Molen, *Inelastic cotunneling with energy-dependent contact transmission*, The Journal of Chemical Physics **146**, 092325 (2017)

[†]Equal contribution

Acknowledgements

Now that we have all those formalities out of the way, it's time for some fun.[1] I am of the opinion that, much like a child, it takes a village to raise a PhD student. So some words of appreciation are needed for the inhabitants of the village that helped make this journey possible, enjoyable, and always filled with interesting moments(in between all the impossible and unenjoyable moments). During my years here in QN it has been my privilege to get to know, work, share a drink, talk about life and the universe, joke around, complain about another failed experiment, complain about code that keeps on crashing, and experience an undoubtedly changed world since march 2020, with a bunch of wonderful people.

First I would like to thank **Sonia Conesa-Boj** for the opportunity to work in this group, the morning and afternoon coffees, as well as the never-ending support and advice given during the last four years. It has been a wonderful journey from the first interview up until the last shared cup of coffee right before writing this sentence. When I joined we were a group of three for a long time, and it has been exciting to see how the group has grown, and will undoubtedly continue (CVD) growing. Gràcies per tot, ha estat una experiencia genial!

I would also like to thank my promotor **Kobus Kuipers**. I highly appreciate your support for the PhD council and your constant work on creating a healthy working environment, where everyone can flourish.

I joined the Conesa-Boj group as the first PhD student, joining the first postdoc **Miguel Tinoco Rivas** in helping to set up the lab. Miguel, it was a pleasure working with you. Your unending patience is one of your biggest assets. I wish you further success on your academic and non-academic journey. The group started to grow when **Maarten**, and then shortly after, **Sabrya** joined for their PhD projects(it's always entertaining to see who can out-organize the other). I can say that for both of you that your attention to details have been a tremendous asset to the group and will surely help you with whatever paths you two choose to take. **Abel** I'm sure that your chill attitude will help with all the learning of the machines that you will continue to do, if not then you can always try and use an infinite amount of Gaussians. During my PhD I had the opportunity to supervise three bachelor students, **Olivier**, **Martijn**, and **James**. I hope that you learned from me as much as I learned from you. At the end of 2019 I got interested in machines and how they learn, thanks to the nice lectures given by **Juan Rojo** at Nikhef. Fortunately, Juan, together with the machine teachers, **Laurien**, **Isabel** and **Jaco** all took an interest in applying their teaching skills towards spectroscopy techniques used in the TEM. It was a great pleasure to work with you all, I'm quite glad and proud with what we were able to accomplish and am excited to see how the work can be further used for analysis in the TEM community. We can also use this work to convince our future machine overlords

---

[1]with grammar mistakes and typos and all!

to spare us when the singularity occurs. I am in the fortunate position to have known all the members that have been part of the Conesa-Boj group, namely the rest not yet mentioned being **Assunta**, **Magda**, **Stef**, **Rose**, **Dave**, **Jorien**, and **Jeroen**.

Carrying out research in this day and age is a massive undertaking, where a support staff is crucial to make sure that everything runs smoothly. I would like to thank **Etty**, **Heleen**, **Maria**, and **Erika**(I hope that one day I will learn to fill in my hours on time) for all the support they have given, **Tino** and **Tom** for the help in setting up the CVD lab. I would also especially like to thank all who made it possible to give us researchers the opportunity to keep on researching during all the lockdowns. For me at least, being able to see my colleages every once in a while during the first weeks of the first lockdown(and all subsequent lockdowns) helped with coping to this strange new world.

The research carried out in this work wouldn't have been possible without the facilities provided by the Kavli nanolab. A big chunk of the work was possible due to a lot of fruitful discussions with the amazing Kavli nanolab staff. I'm sure every cleanroom user is super greatful that it's been possible to keep the cleanroom open and continue with nanofabrication processes during the last eighteen months, and I would like to express my deep gratitude for all the hard work of the Kavli nanolab staff. When it came to etching nanopillars, I could always turn to **Marc Z** and **Charles** for helpful suggestions on how to proceed further with the Estrelas. Using the FIB system wouldn't have been possible without the support from **Hozanna**. Of course, the rest of the cleanroom processes would not have been possible without the advice and help of **Pauline**, **Eugene**, **Anja**, **Arnold**, **Roald**, **Bas**, and **Ewan**.

F190 has always been the office which I have inhabited since I started in QN. At one point the original F190 (**Miguel**, **Jeremié**, **Mari**, **Dima**, **Ranko**) was arguably the loudest office in the F-wing corridor, and I take quite a lot of pride in that. The current F190 (**Brecht**, **Jorrit**, **Ulderico**, **Jorris**, and **Maarten**) needs to defend that title, in my humble opinion. Dima, I know how much you value PhD theses, so this line is for you :). I cannot say enough words of thanks to Jeremié for your help with my DFT questions. Mari and Miguel, it was always entertaining to hear you talk(curse) in spanish about whatever and nothing. And Ranko, I'm pretty sure you always enjoyed my vocal excercises in the office. Also, you might have a dutch passport now, but you will always have a Montenegrin passport in my heart :). In a way, Jorrit has been a member of F190 even before starting his PhD. For a while it was fun to see who could arrive the earliest in the office(although nothing beats the tyranny of living in the same city as where one works). The gold standard of arriving early is still given by Miguel's punctuality.

The cleanly cleanroom days were(and still are) made more enjoyable by having amazing colleagues to work with, along with all the toys(I mean equipment) available in the cleanroom. In this respect, fruitful (and unfruitful, vegetable) discussions concerning nanopillars with Brecht always made the time fly by quite fast(there's a joke on fast etching there somewhere, probably). I also want to thank **Elvedin** for all the discussions on resist and recipes, without which would have made the fabrication process quite a bit more difficult. Additionally, the NP project was further enhanced(get it?) by **Marc N**'s nonlinear optical experiments. It was very encouraging to see someone from outside the group being so enthousiastic for the NP project and helpful in getting some nice experiments done on them.

Other than the sciencey scientific part, the friday afternoon drinks in the TeePee cafe, with the subsequent dinners have been the origin for a lot of great memories. Partners in crime include(but are not limited to) **Rasa**, **Iacopo**(fellow first PhD in a new group person), **Laëtitia**, **Lukas**, **Mattias**, **Thierry**, **Nikos**, **Holger**, and **Patrick**; Here's to future days with more Teepee and dinners.

Another group of QN inebriators that I managed to be part of include **Sonakshi**(arguably, the leader), **Nina**(space girl), **Nicco**, **Parsa**, **Liu**, **Mathijs**, and it's been a privilege to get to know all of you. I'm sure that one day our social-activities-organization-skills will improve. Sonakshi, this friendship started in Courchevel, I think our first conversation was about toes or something. It's been a great couple of years, and when you become all rich and powerful, please remember about the little people(i.e. give me your monniiesss).

As some of you might know, I do enjoy a pun or two. I think that one beautiful feature of language is that there is evidence that puns might be found in all languages.[2] Of course, this is one personal opinion on language, and other (wrong)opinions exist that state that puns do not count as humor(they do). What I want to convey here is that we all have a deep personal connection to the languages that we speak. Papiamento has always been an important part of my identity, and as such, it was very important to me that there be a Papiamento translation of the summary of this thesis. For this I would like to thank **Esther** and **Ramon Todd Dandaré** for their help in translating the summary into Papiamento. Masha danki pa e ayudo, mi ta spera cu Papiamento por sigui crece y por bira mas uza den e literatura cientifico.

Before getting the PhD position in QN there were two couches and one small room made available to me after I gave up my student room after my master studies. The two couches belonged to two wonderful people who would later become my housemates at Zuidwal. **Jess** and **Sindy**, moving in with you two was one of the best decisions I have ever made. All the fond memories created during the trips to Haagse markt, random walks in the Hague, and random dance parties during the first lockdown(I shudder when I imagine how that first period of isolation would have been without you two), has been some of the best times in my life. Perhaps one day I will have as much a love for board games as ya'll and **Ben**. I also need to give a big word of thanks to **Mark** and **Nicolle** for the small room provided to me during the last months of 2016 and first half of 2017(and this was not even the first time I lived in that room). Thank you for everything! During the search for a PhD position having two caring housemates really helped with that period of uncertainty. I think a box of stickers should be a nice present for you. Now with the PhD ending, I am once again asking for that room......................just kidding.

During all the years living in the Netherlands I've managed to have a not-blood-related family away from the Aruban home. Thank you all for all the outings, sleepovers, dinners, discussions, dancing, laughing. Eventhough we might not see each other as much as we used to, the love is still there. Here's to all the amazing years of the past, and to the years to come ; **Krista**, **Lloyd**, **Kyra**, **Tibi**, **Sarah**, **Thali**, **Memo**, **Sherwin**, **Pedro**, **Viviana**, **Deon**, **Carolus**, **Kaye**, **Damiano**, **Birgitt**, **Andrew**, **Stacey**, **Evertson**(AASSSPPEEENNN), **Taiza**, **Densay**, **Junior**, **Kevin**, **Alyssa**, **Iskra**, **Mandy Patch**, **Nova**. Tambe mi kier a bisa cu tur biaha mi bai bek Aruba, mi semper por a hang out cu the flower sisters, **Dani** y **Chantal**,

---

[2]See for example the article "Are pun mechanisms universal? A comparative analysis across language families" https://doi.org/10.1515/humor-2012-0017

That was quite a ride, amirite?